Models of polymer solutions in electrified jets and solution blowing

Marco Lauricella

*Istituto per le Applicazioni del Calcolo, Consiglio Nazionale delle Ricerche,
Via dei Taurini 19, I-00185 Rome, Italy*

Sauro Succi

*Center for Life Nanoscience at la Sapienza, Istituto Italiano di Tecnologia,
Viale Regina Elena 295, I-00161 Rome, Italy,
Istituto per le Applicazioni del Calcolo, Consiglio Nazionale delle Ricerche,
Via dei Taurini 19, I-00185 Rome, Italy,
and Harvard Institute for Applied Computational Science,
Cambridge, Massachusetts 02138, USA*

Eyal Zussman

*Faculty of Mechanical Engineering, Technion—Israel Institute of Technology,
Haifa 32000, Israel*

Dario Pisignano[*]

*Dipartimento di Fisica, Università di Pisa, Largo Bruno Pontecorvo 3, I-56127 Pisa, Italy
and NEST, Istituto Nanoscienze–Consiglio Nazionale delle Ricerche,
Piazza San Silvestro 12, I-56127 Pisa, Italy*

Alexander L. Yarin

*Department of Mechanical and Industrial Engineering, University of Illinois at Chicago,
842 West Taylor Street, Chicago, Illinois 60607-7022, USA*

(published 18 August 2020)

Fluid flows hosting electrical phenomena are the subject of a fascinating and highly interdisciplinary scientific field. In recent years, the extraordinary success of electrospinning and solution-blowing technologies for the generation of polymer nanofibers has motivated vibrant research aiming at rationalizing the behavior of viscoelastic jets under applied electric fields or other stretching fields including gas streams. Theoretical models unveiled many original aspects in the underpinning physics of polymer solutions in jets and provided useful information to improve experimental platforms. This review examines advances in the theoretical description and numerical simulation of polymer solution jets in electrospinning and solution blowing. Instability phenomena of electrical and hydrodynamic origin, which play a crucial role in the relevant flow physics, are highlighted. Specifications leading to accurate and computationally viable models are formulated. Electrohydrodynamic modeling, theories on jet bending instability, recent advances in Lagrangian approaches to describe the jet flow, including strategies for dynamic refinement of simulations, and effects of strong elongational flow on polymer networks are reviewed. Finally, the current challenges and future perspectives in the field are outlined and discussed, including the task of correlating the physics of the jet flows with the properties of relevant materials, as well as the development of multiscale techniques for modeling viscoelastic jets.

CONTENTS

[*]dario.pisignano@unipi.it

035004-1

I. INTRODUCTION

Coupling electrical phenomena and fluids leads to an interdisciplinary scientific field that has been fascinating physicists for centuries. Pioneers in this field were, among others, William Gilbert, Lord Rayleigh, and Sir Geoffrey Taylor (Taylor, 1964, 1966). For instance, Gilbert (1600) noted that a sessile droplet of water lying on a dry surface is deformed near the apex into a cone when it is approached by a rubbed amber. Indeed, when rubbed with fur or wool the amber acquires a net negative electric charge, through a kind of contact electrification that is known as the triboelectric effect. A few simple experimental consequences of the triboelectric effect, such as the capability of rubbed amber to attract small wires or feathers, have been known for many centuries (since ancient Greece). The deformation of sessile droplets observed by Gilbert was also due to electrostatic attraction, namely, to the interaction of the rubbed amber and droplets warped from their resting shape by an electric field. In Gilbert's experiment, a water droplet is placed onto a glass surface and the water-amber attraction is sustained by positive electric charges at the liquid surface, thus determining a conical shape as sketched in Fig. 1(a). A photograph of a conical surface made of canola oil, stretched by an electric field and captured with a high-speed camera (Collins *et al.*, 2008), is shown in Fig. 1(b). The fact that conical liquid-air interfaces can be generated in this way is, at first sight, surprising. This stands in contrast with our everyday experience that a droplet of water tends to be pulled into a spherical shape, namely, to reach a minimum surface area A that is due to the imbalance of cohesive forces (i.e., the attraction of the liquid molecules to each other) at the surface layer. The surface tension α of the liquid is the physical quantity that is defined by such an imbalance of cohesive forces and it is expressed by the Gibbs free energy W_G per unit area at constant temperature and pressure,
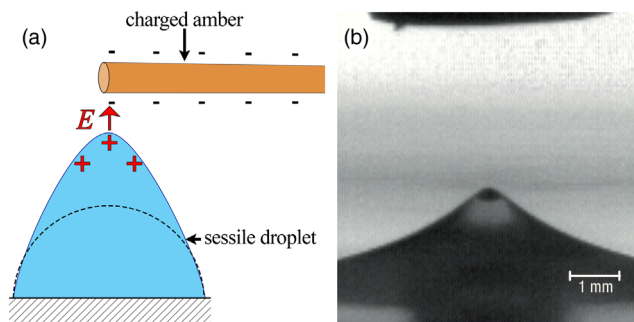

FIG. 1. (a) Sketch of Gilbert's observation of the electrostatic deformation of sessile water droplets. A piece of negatively charged amber is placed in proximity to a sessile droplet lying on a surface. The electric field E generated by the rubbed amber deforms the droplet, from the resting shape (dashed line) into a conical one (continuous line). (b) Conical liquid-air interface photographed in a region affected by an electric field. The liquid is canola oil. Adapted from Collins *et al.*, 2008.

$\alpha = \partial W_G / \partial A$, while the cohesive imbalance is expressed by the Laplace pressure, which is $\alpha(r_{T1}^{-1} + r_{T2}^{-1})$, where r_{T1} and r_{T2} are the principal radii of curvature of the liquid-air interface. As a consequence, another force needs to be applied to the fluid to have the latter strained out of its unperturbed shape in which the surface area is minimum and the curvature is constant. The accumulation of an excess charge on the surface of a droplet, due to an electric field generated in the region of space surrounding the liquid-air interface, can provide such extra force (the Maxwell stresses) in an extremely effective way (Reznik *et al.*, 2004, 2006; Collins *et al.*, 2008), thus leading to the formation of an apex as displayed in Fig. 1. As is clear in this review, producing conical shapes in liquid-air interfaces this way is important from a technological viewpoint since it is fundamental for the possibility of focusing and stretching polymer molecules dissolved in fluids into submicrometer features.

In the 20th century, patents describing methods for dispersing fluids with the aid of electric fields were issued to Cooley (1902) and Morton (1902). These early studies were followed by others from Zeleny (1914, 1917), and finally by some patents of Formhals (1934, 1939, 1940, 1943, 1944), who focused on the formation of fibers by means of electrified jets of solutions of cellulose acetate. Later fibers with diameter smaller than 1 μm were realized from electrified jets of acrylic solutions in dimethylformamide (DMF) by DuPont researchers (Baumgarten, 1971). However, it was with two works from Reneker's group (Doshi and Reneker, 1995; Reneker and Chun, 1996) that the interest for the process named electrostatic spinning, i.e., electrospinning, started at our times. Such technology was largely developed during the years around 2000, concomitantly with a significant growth in global interest in nanotechnology that opened new routes for the headway of a variety of applications.

Depending on the process parameters, which involve the electric field applied to a polymer solution, the solution

concentration, and various aspects of the experimental setup used (details are presented in Sec. III.B), the polymeric, carbon (carbonized), or ceramic (calcined) fibers produced by electrospinning exhibit cross-sectional diameters ranging from a few nanometers (Huang *et al.*, 2006) to a few microns. This property directly affects the surface area to material mass ratio. Indeed, polymer filaments with a cross-sectional radius about 100 nm and material density about 1.5 g/cm^3 have a surface area to mass ratio well above 10^5 cm^2/g, which offers intriguing prospects for several practical applications. In addition, the electrospinning process has been found to be chemically versatile, i.e., fibers could be formed from a wide variety of compounds, such as thermoplastic materials, conductive and light-emitting polymers, piezoelectric polymers, biomolecules, and blends. Many aspects of this technology could be engineered at an advanced level. This has been aimed at fabricating nanofibers with desired shape, morphology, and composition (Sun *et al.*, 2003; Li and Xia, 2004a; Loscertales *et al.*, 2004; Ji *et al.*, 2006; Zussman *et al.*, 2006; Yarin, Pourdeyhimi, and Ramakrishna, 2014), assembled in specific architectures and networks (Theron, Zussman, and Yarin, 2001; Li, Wang, and Xia, 2003; Zussman, Theron, and Yarin, 2003; Sun *et al.*, 2006; Xie *et al.*, 2010), or performing given functions. Finally, electrospinning technologies are operationally simple, they need a relatively low investment for equipment, and their throughput is generally much higher than those of other methods for producing nanostructures, such as high-resolution lithographies, nanoimprinting, molecular self-assembly, and colloidal synthesis (Xia *et al.*, 2003; Li and Xia, 2004a; Luo *et al.*, 2012). For these reasons, the applications of electrospun fibers today span the entire field of nanotechnology and microtechnology, including filtration, catalysis, energy harvesting and storage, photonics and optoelectronics, nanoelectronics, development of surface coatings with controlled wettability and thermal properties, new textile materials, chemical and biochemical sensors, systems for drug delivery, and tissue engineering and regenerative medicine, as well as cancer research, as summarized in Fig. 2.

Electrospinning and related methods, as well as the applications of nanofibers and microfibers produced by them, have been the subject of several books (Ramakrishna *et al.*, 2005; Reneker and Fong, 2006; Filatov, Budika, and Kirichenko, 2007; Wendorff, Agarwal, and Greiner, 2012; Pisignano, 2013; Yarin, Pourdeyhimi, and Ramakrishna, 2014; Yarin, Roisman, and Tropea, 2017) and reviews (Dzenis, 2004; Li and Xia, 2004b; Greiner *et al.*, 2006; Greiner and Wendorff, 2007; Reneker *et al.*, 2007; Yarin *et al.*, 2007; Reneker and Yarin, 2008; Yarin, 2011; Choi *et al.*, 2017). Not equally covered is the major effort done to develop theoretical models of these processes, which is the subject of this review.

Modeling approaches might offer a critical tool to investigate the underpinning physics of electrified polymer solutions and provide valuable information for rationalizing observed phenomena, and then for substantially improving experiments. Here we report on the main modeling strategies pursued in recent decades, introducing relevant physical characteristic lengths and highlighting instability phenomena of an electrical and hydrodynamic nature, which play a crucial role in the physics of flow. The review is organized as follows. The processes, their working principles, and relevant dimensionless parameters describing the physics underneath are presented in Sec. II. Section III provides an introductory yet comprehensive overview of the experimental methods and of the physical rationale behind them. Section IV presents the specifications that make modeling reliable in describing the dynamics of these fluids, namely, what one needs to elaborate on accurate and computationally viable models. These aspects include, for instance, required parameters from experiments and phenomenology, as well as specific computational platforms and resources. Section V.A discusses the modeling methods of the physical processes that affect electrified fluids and that are based on a so-called electrohydrodynamic (EHD) description. Then the physical reasons of the instabilities affecting electrospun fluids are reviewed. A general and detailed model of the electrospinning process was formulated in the past two decades by Reneker *et al.* (2000, 2007) and Yarin, Pourdeyhimi, and Ramakrishna (2014). The basic building blocks on which these and other, more recent models were formulated are reported in Secs. V.B and V.C. The main approaches developed for modeling the flow of electrified fluids under high strain rates, namely, under fast deformation, and its effects on polymer networks are described in Sec. V.D. Section VI reviews modeling methods for solution blowing, that is, an air-jet spinning method and among the most recent and promising technologies to generate nanofibers (Yarin, Pourdeyhimi, and Ramakrishna, 2014; Sinha-Ray *et al.*, 2015). In this process, polymer solutions are delivered into a coflowing subsonic or supersonic gas jet that stretches them directly (i.e., without the application of an electric field). Exploiting the aerodynamic drag force results in a 100-fold increase in the production rate of nanofibers, and in higher compatibility with industrial equipment already designed for other uses such as meltblowing (Kolbasov *et al.*, 2016). Finally, an outlook is provided in Sec. VII regarding currently open challenges, as well as possible future developments of theory and modeling methods for this class of technologies.

A few details on notation and units used in this paper deserve mention. Throughout the review, boldfaced characters denote vectors. For equations containing terms depending on the electric field, we use Gaussian (centimeter-gram-second, cgs) units unless otherwise stated since these are highly convenient where the highlighted physics encompasses both electrostatics and fluid mechanics. An advantage of the cgs system is in the compact-dimensional description of physical quantities, which involves only three base quantities (length, mass, and time). In particular, while in SI units the electric charge q needs to be defined as an independent quantity (in Coulomb units), in the cgs system setting the vacuum permittivity $\varepsilon_0 = 1$ and the Coulomb constant $k_C = 1$ (Sommerfeld, 1952), the Coulomb's law for the force $F = q^2/\ell^2$ between two charges at distance ℓ easily defines the charge as $q = \sqrt{\mathrm{dyn\,cm}^2} = \mathrm{cm}^{3/2}\,\mathrm{g}^{1/2}\,\mathrm{sec}^{-1} = \mathrm{statC}$. Hence, the electric field, i.e., the electrostatic force divided by the test charge, $E = F/q$, in cgs units is measured in dyn/statC $= \mathrm{cm}^{-1/2}\,\mathrm{g}^{1/2}\,\mathrm{sec}^{-1} = \mathrm{statV/cm}$, and the electric potential, $\Phi = E\ell$, is measured in statV $= \mathrm{cm}^{1/2}\,\mathrm{g}^{1/2}\,\mathrm{sec}^{-1}$. All physical quantities used in this review,
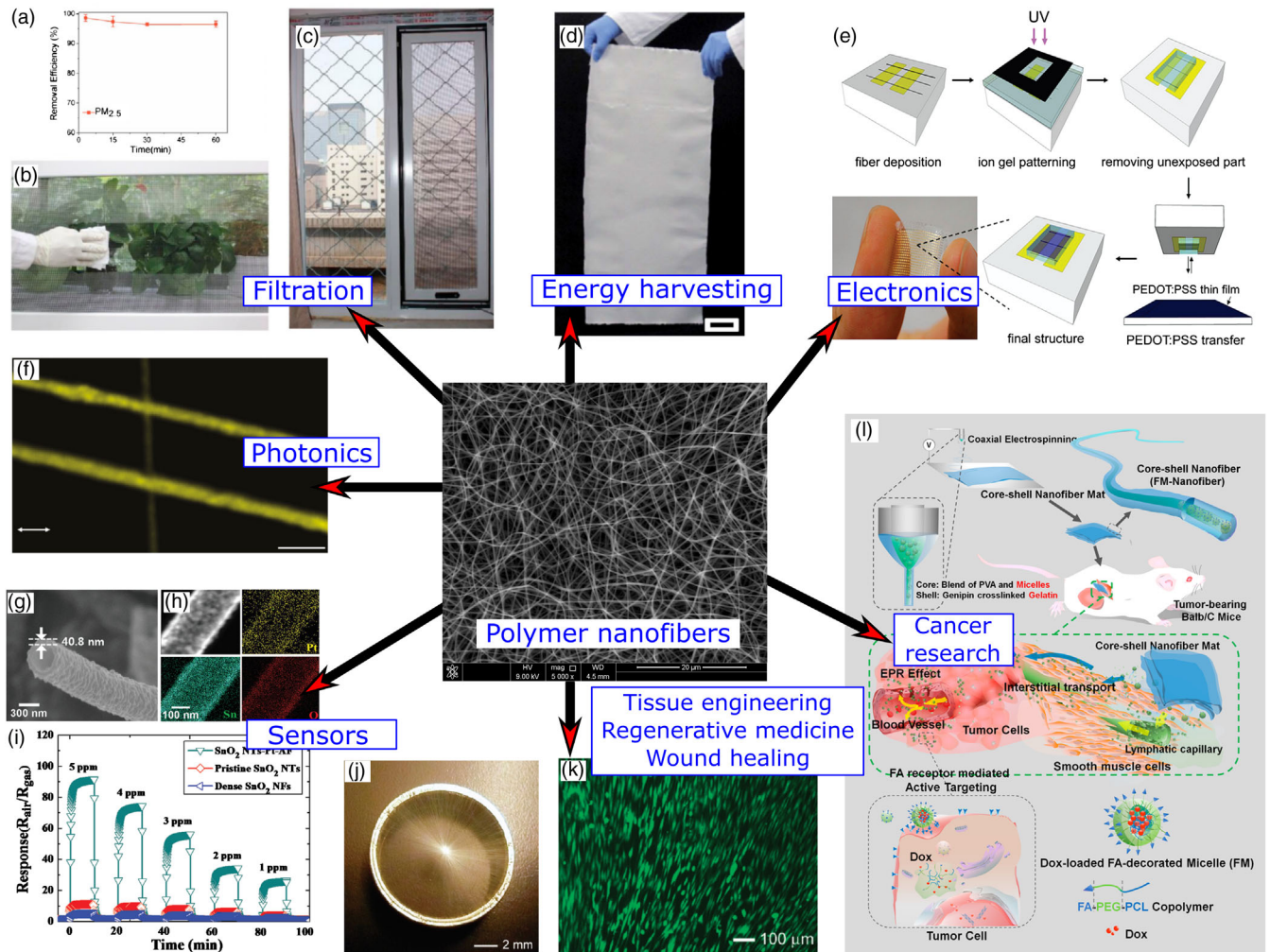
FIG. 2. Applications of nanofibers realized through electrified jets or solution blowing from polymer solutions. (a)–(c) Filtration performance of a window screen coated by polyacrylonitrile nanofibers used to remove PM$_{2.5}$ particles (particles with a diameter smaller than 2.5 μm). The wiping of nanofibers from the window screen, performed by tissue paper, is also shown in (b). Adapted from Khalid *et al.*, 2017. (d) Large-area mat of piezoelectric nanofibers. Scale bar, 5 cm. From Fang *et al.*, 2013. (e) Process for the realization of an array of top-gate field-effect transistors, involving the deposition of electrospun poly(3-hexylthiophene) nanofibers across gaps between source and drain electrodes. The process includes a transfer procedure of a poly(3,4-ethylenedioxythiophene) polystyrene sulfonate (PEDOT:PSS) layer. From Lee *et al.*, 2010. (f) Light-emitting polymer fibers for photonics, showing emission polarized along their longitudinal axis. The arrow displays the direction of the polarizer used to analyze the emitted light. Scale bar, 5 μm. From Pagliara *et al.*, 2011. (g)–(i) Chemoresistive sensors. Example of Pt-loaded SnO$_2$ nanotubes made through electrospinning, corresponding elemental distribution (Pt, Sn, and O), and response to acetone for SnO$_2$ nanotubes, SnO$_2$ nanofibers, and Pt-loaded SnO$_2$ nanotubes. Concentration range, 1–5 ppm at 350 °C. Adapted from Jang *et al.*, 2015. (j),(k) Application in biomedical devices for wound closure or tissue engineering. Radially aligned nanofibers deposited on a ring collector, and image of dura fibroblasts seeded on fibronectin-coated scaffolds made of the radially aligned nanofibers. From Xie *et al.*, 2010. (l) Scheme of the fabrication of an implantable active-targeting micelle-in-nanofiber device (FM-Nanofiber) and of the delivery process of doxorubicin-loaded micelles (FM) from nanofibers to tumor tissues and cells. From Yang *et al.*, 2015.

and their units, are given in the List of Symbols and Abbreviations.

II. PROBLEM FORMULATION AND DIMENSIONLESS PARAMETERS IN ELECTROSPINNING

The electrospinning process (scheme in Fig. 3) generates nanofibers starting from a polymer solution at a high enough concentration (for instance, 5%–30% in polymer weight with respect to solvent) and applying an electric voltage bias

($\Delta\Phi_0 \approx$ 3–300 statV, namely, 1–100 kV) between the solution and a metal surface onto which fibers are to deposited. The motivation for having a high concentration of molecules in the polymer solution is that such molecules have to be entangled to provide the fluid with remarkable viscoelastic properties, as better described later. In a typical process, the solution and the metal surface of the target (a counterelectrode) are initially at a typical distance h ranging from a few centimeters to a few tens of centimeters, thus leading to electric fields E from a few statV/cm to a few tens of
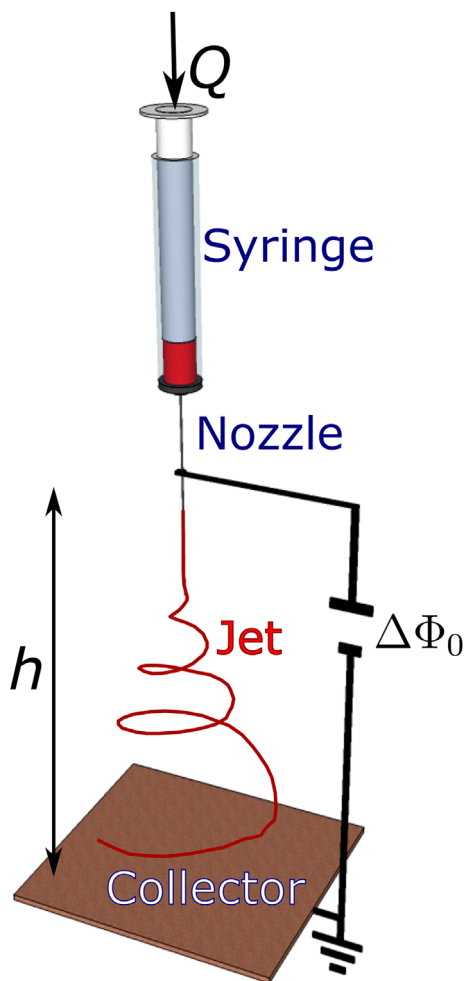
FIG. 3. Scheme of electrospinning. The various process parameters are indicated, nozzle-collector distance (h), nozzle-collector voltage bias ($\Delta\Phi_0$), polymer solution flow rate (Q), together with main experimental equipment (syringe, metal needle, collecting surface).

statV/cm (i.e., ~2–10 kV/cm). The accumulation of an excess charge on the solution surface (i.e., a droplet, or a free liquid surface) then leads to the formation of an apex with a well-defined shape and local radius r_T at the same surface. The determination of the exact shape of this apex has been the subject of intense research that is reported in Sec. V.A.1. Upon increasing the applied voltage, electric forces overcome the elastic forces characteristic to viscoelastic polymer solutions and surface tension (α) and destabilize the pristine fluid body. Limiting ourselves for simplicity to the contributions from electric forces and surface tension, this effect can be conveniently expressed by a dimensionless parameter, which is the electric Bond number, Bo $= r_T E^2/\alpha$, where E is the electric field at the solution apex. The Bond number directly compares the electrostatic pressure at the liquid surface ($\varepsilon_0 E^2/2$ for a liquid acting as a perfect electric conductor in the vacuum with $\varepsilon_0 = 1$ in cgs units) with the Laplace pressure ($2\alpha/r_T$), which is related to surface energy. Hence, when Bo approaches unity (Reznik *et al.*, 2004), a significant deformation of the solution surface can be achieved. Considering typical values of $\alpha = 50$ g/s^2 and $E = 10$ statV cm^{-1}, which corresponds to

3 kV cm^{-1}, one would have a Bo value up to 0.2 for an apex radius ≤ 0.1 cm. As a result, strain occurs in the fluid body, and an electrically charged solution jet is issued in electrospinning.

Viscoelasticity plays a crucial role in the jet onset. Since the used solution concentration is quite high, a significant amount of polymer entanglements are formed in the fluid. Overly low values of the polymer concentration in the solution might instead lead to electrospraying (or the so-called dripping regime), thus forming monodisperse or polydisperse, charged sprayed droplets instead of a jet and nanofibers (Collins, Harris, and Basaran, 2007; Gañán-Calvo and Montanero, 2009; Herrada *et al.*, 2012; Collins *et al.*, 2013; Gañán-Calvo *et al.*, 2018). The dimensionless quantity allowing one to distinguish between the two cases of jetting (electrospinning) and dripping (jet breaking) is the capillary number, Ca $= \mu_e \upsilon/\alpha$, where υ is the jet velocity and the characteristic dynamic viscosity involved is the elongational viscosity, $\mu_e = \sigma/\dot{\varepsilon}$ (σ, longitudinal stress and $\dot{\varepsilon}$, strain rate). The capillary number is the ratio between the (elongational) viscous forces and capillary forces (Anna and McKinley, 2001; Montessori *et al.*, 2019), and it also allows *high-viscosity* and *low-viscosity* fluids to be distinguished in electrospinning experiments, depending on the obtained Ca values. In the jetting regime, the electric field is strong enough to imprint a suited velocity, or the solution viscosity is high enough that the viscous forces overcome the surface tension (Ca > 1). For instance, in aqueous solutions of poly(ethylene oxide) (PEO) at different concentrations, with elongational viscosity spanning from 500 to 5000 g cm^{-1} s^{-1} (Xu, Yarin, and Reneker, 2003; Reneker *et al.*, 2007), and typical values $\upsilon = 10$ cm s^{-1} and $\alpha = 50$ g/s^2, the corresponding capillary number is in the range 10^2–10^3. On the other hand, if the capillary force is dominant (Ca < 1), the jet rapidly necks down pinching off into droplets due to the Rayleigh-Tomotika instability (Tomotika, 1935), and small droplets can be easily emitted from the solution surface (dripping regime). In other words, in this regime the polymer jets cannot be stabilized against the capillary instability (Entov and Yarin, 1984a; Yarin, 1993).

During the fast (≤ 0.1 s) path to the counterelectrode, the electrospun jet is dramatically stretched, initially as a short almost straight section and then, in the course of various other instabilities that *bend* the trajectory of the fluid, generating spiraling loops as shown in Fig. 4 (Reneker and Fong, 2006; Reneker and Yarin, 2008). The term *bending instability* in electrospinning (Reneker *et al.*, 2000) is motivated by a similar term applied to the kindred aerodynamically driven bending instability (Weber, 1931), and a basic similarity was also recognized between bending jets and the elastic bar bending in the classical Euler-Bernoulli theory (Landau and Lifshitz, 1970). Bending instabilities occur because small perturbations rapidly trigger their growth, which is driven by the fact that lateral electric forces, namely, electrostatic repulsion of charges along the fluid filament, appear at any curved section of the jet. These instabilities influence the electrospinning outcome in many ways, increasing the overall length of the jet trajectory to a practically fractal-like one and thus leaving longer time for fluid stretching and diameter reduction, and also leading to a
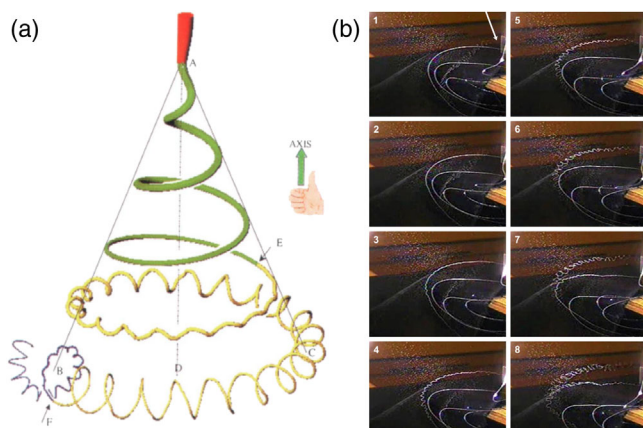
(a)

(b)

FIG. 4. (a) Schematics of an electrified polymer solution jet. The various regimes of jet flow are highlighted, with a straight region (A) followed by various bending instability stages featuring spiraling loops with different characteristic frequency. D indicates the projection of the straight region along the vertical direction. AB and AC indicate the jet envelope cone. E and F indicate points of onset of the second and third bending instabilities, respectively. From Reneker and Fong, 2006. (b) Photographs of a jet of polyisobutylene in a viscous mixture of acetone and paraffin oil, highlighting bending instability. The frames are captured by a video camera at a rate of 30 frames/s. The diameter of the largest coils is about 20 cm. From Reneker and Yarin, 2008.

highly disordered configuration of nanofibers (nonwoven mat, central panel of Fig. 2) deposited on flat counter-electrodes. Owing to instabilities, an electrospun jet is a highly complex system, namely, a continuous fluid object whose cross-sectional radius r and curvature k (defined as the inverse of the curvature radius and measured in cm^{-1}) both are strongly dependent on the position along the fluid filament. In addition, the solvent simultaneously evaporates while the jet is moving, which allows solid polymer nanofibers to be deposited.

Fortunately, some physical estimates allow the description of electrospun solutions to be simplified in the different regions of the jet. Indeed, much of the jet dynamics depends on the magnitude of the characteristic hydrodynamic time θ_H versus the relaxation time θ_C of ionic charges present in the fluid. θ_H can be estimated as $\mu r/\alpha$ (Reznik *et al.*, 2004). With μ of the order of $10\ \mathrm{g\,cm^{-1}\,s^{-1}}$ ($1\ \mathrm{g\,cm^{-1}\,s^{-1}} = 1\ \mathrm{P} = 0.1\ \mathrm{Pa\,s}$), which is reasonable for electrospun solutions, and $\alpha = 50\ \mathrm{g/s^2}$, one would obtain a θ_H value of the order of 10 ms for $r = 0.1$ cm and well below the milliseconds for $r \leq 10\ \mu\mathrm{m}$, respectively. The characteristic charge relaxation time θ_C can be estimated as ε/σ_e, where ε is the dielectric permittivity and σ_e is the electric conductivity (expressed in s^{-1} in cgs units). With plausible values of $\varepsilon = 40$ and σ_e in a range 10^3–10^4 s^{-1} (corresponding to 10^{-7}–10^{-6} S m^{-1} in SI units), θ_C is up to a few milliseconds ($\sim$4–45 ms) for polymer solutions used in electrospinning (Reneker *et al.*, 2007; Yarin, Pourdeyhimi, and Ramakrishna, 2014). These solutions are in fact leaky dielectrics, i.e., poor ionic conductors (Melcher and Taylor, 1969; Saville, 1997). However, whenever θ_H is significantly higher than θ_C, the electric behavior of an ionic

conductor reduces to that of a perfect conductor, even though it is actually a poor conductor compared to such truly good conductors as metals. On the contrary, when $\theta_H \ll \theta_C$, the fluid body can be considered a perfect dielectric, with "frozen" charges (Reneker *et al.*, 2000). This means that while the electrospun jet continuously reduces its diameter when moving from the initial fluid apex to the counter-electrode, its physical description might actually change from that typical of a conductor to that typical of a dielectric system. We see later in this review how this feature is exploited in models of the electrospinning dynamics.

The strong elongational flow in the jet also causes a substantial stretching of involved macromolecular coils and polymer networks. Indeed, strain rates exerted by fluid bodies during elongational processes that are comparable to or higher than the reciprocal relaxation time θ^{-1} of the involved polymer molecules favor the transition of random coils into stretched and relatively aligned molecular assemblies (de Gennes, 1974). This can be expressed in terms of the dimensionless Deborah number De $= \dot{\varepsilon}\theta$ that quickly reaches a value above unity along the jet path (Bellan, Craighead, and Hinestroza, 2007). Such an effect can be observed experimentally by various methods, including Raman, luminescence, birefringence, infrared spectroscopy, mechanical measurements, and x-ray inspection (Fong and Reneker, 1999; Arinstein *et al.*, 2007; Kakade *et al.*, 2007; Reneker *et al.*, 2007; Pagliara *et al.*, 2011; Pai, Boyce, and Rutledge, 2011; Camposeo *et al.*, 2013; Richard-Lacroix and Pellerin, 2013, Yarin, Pourdeyhimi, and Ramakrishna, 2014; Richard-Lacroix and Pellerin, 2015), and it was also discussed theoretically (Greenfeld and Zussman, 2013; Deng, Arinstein, and Zussman, 2017). For instance, below a certain crossover diameter of electrospun nanofibers that is dependent on the polymer molar mass the elastic moduli of the fibers begin to rise sharply (Arinstein *et al.*, 2007; Burman, Arinstein, and Zussman, 2008; Ji *et al.*, 2008; Burman, Arinstein, and Zussman, 2011; Liu *et al.*, 2011). Similarly, in optically active polymers, the effective conjugation length of chromophores might increase as a result of electrospinning, and the optical absorption and emission become polarized along the fiber axis (Camposeo *et al.*, 2013, 2014). These findings are highly important for applications of polymer nanofibers. They also further make clear that rationalizing the dynamics of electrospun jets by means of proper models is essential to understand how the jet properties affect, or are inherited by, the obtained nanofibers. The main phenomena to be caught by models are described in Sec. III.

III. PHENOMENOLOGY OF ELECTRIFIED JETS

A. Formation and characteristics of electrified jets

In electrospinning, polymer solutions are usually delivered in a continuous way through a syringe (Fig. 3), terminated by a metallic needle with a diameter of a few hundred micrometers. This leads to the formation of a pendant droplet at the tip of the needle. However, most of the mechanisms producing electrified jets are general, and they hold not only for pendant droplets but also for any other free surface (Yarin and Zussman, 2004; Lukas, Sarkar, and Pokorny, 2008). For

instance, upon inserting an electrode into a charged sessile or pendant droplet of polymer solution and applying an electric voltage bias with respect to a counterelectrode, the droplet can acquire a stable shape whenever the potential difference is not too high (Reznik *et al.*, 2004). As introduced in Sec. II, this can be achieved by connecting electrodes to a high-voltage generator, and the counterelectrode functions as a collecting surface onto which polymer nanofibers are to be deposited. The corresponding electric field imposes the electric Maxwell stresses pulling and stretching the droplet toward the counterelectrode. The surface tension of the fluid would tend to minimize the droplet surface and shape it as a spherical volume (thus minimizing the surface energy) through the Laplace pressure. The elastic effect in the viscoelastic polymer fluid, which might be much higher than the surface tension, also plays a restraining role. A steady-state droplet shape then arises as a result of the interplay between the Maxwell stresses and the restoring forces. The shape at the apex of the droplet was originally described by the so-called Taylor cone (Taylor, 1964, 1966). This shape at the transition region between the stressed droplet and the formed jet is important. Indeed, correlations were recently found between observable features of the droplet-jet shape and the diameter of the obtained electrospun nanofibers (Liu and Reneker, 2019).

The condition on the threshold electric field for jet activation corresponds to a condition in terms of the minimum surface charge density accumulated at the fluid-air interface near the apex (the so-called Rayleigh condition). In addition, because of the high solution concentration, in electrospinning significant elastic stresses should also be overcome by the electric Maxwell stresses.

Once formed, the jet proceeds quickly toward the counterelectrode. The jet velocity ranges from the order of 10 to a few hundred cm/s, which can be measured by various experimental techniques such as particle image velocimetry (Bellan, Craighead, and Hinestroza, 2007; Reneker *et al.*, 2007) and direct high-speed imaging (Yarin, Koombhongse, and Reneker, 2001a; Han, Yarin, and Reneker, 2008; Montinaro *et al.*, 2015). Corresponding accelerations reach the order of 10^4 cm/s^2. The high strain rate $\dot{\varepsilon}$ thus reached, exceeding the reciprocal relaxation time θ^{-1} of the solution (de Gennes, 1974; Thompson *et al.*, 2007), might stretch the polymer matrix into a nonequilibrium conformational state (Greenfeld *et al.*, 2011). This effect is at the origin of the significant orientational anisotropy inherited by the produced nanofibers. In this way, polymer chains might become prevalently oriented along the longitudinal axis of electrospun fibers, which in turn affects several optical, electronic, and mechanical properties, although some relaxation of the anisotropic structure can still occur after formation.

The jet continuously delivers an electric charge from the spinneret to the counterelectrode, which results in a current $I = Q\rho_q$, where Q is the jet flow rate and ρ_q is the volumetric charge density. The overall charge carried by the jet rapidly transforms into surface charges, leading to bulk and surface advection components that contribute to the current (Fridrikh *et al.*, 2003; Reznik *et al.*, 2006). During the jet flight and the development of the bending instability, the electric charges are basically at rest with respect to the jet because the characteristic charge relaxation time θ_C is larger than the characteristic hydrodynamic time θ_H; see Sec. II. In other words, in this regime transport processes associated with viscoelastic relaxation and hydrodynamics are faster than electric transport phenomena (Saville, 1997), leading to the conclusion that during its path toward the counterelectrode (collector) the jet may be assumed as a perfect dielectric (Yarin, Pourdeyhimi, and Ramakrishna, 2014). Some of these aspects are further detailed in Sec. V.A. Overall, a quantity denoted by ρ_q can still be used to indicate carried charge density, meaning an effective charge density that would account for both bulk and surface advection components contributing to the current. The current delivered by electrospun jets was investigated in dedicated experiments (Theron, Zussman, and Yarin, 2004; Bhattacharjee *et al.*, 2010). Depending on the used polymer solution and other process parameters, values ranging from the order of nanoamperes to hundreds of microamperes ($\sim$3 to 3×10^5 statC/s) have been measured (Reneker and Chun, 1996; Deitzel, Kleinmeyer, Harris, and Beck Tan *et al.*, 2001; Hohman *et al.*, 2001b; Theron, Zussman, and Yarin, 2004; Kalayci *et al.*, 2005; Bhattacharjee *et al.*, 2010).

The evaporation of the solvent from the jet is another phenomenon that is important to the process outcome, contributing to diameter reduction and determining whether still wet or fully dried nanofibers are deposited on the collector (Yarin, Koombhongse, and Reneker, 2001a). In addition, if the evaporation rate is sufficiently high, the solvent evaporation being faster from the external layers of the jet might lead to the formation of a polymer skin along the fluid body (Koombhongse, Liu, and Reneker, 2001; Guenthner *et al.*, 2006). Such skin can then collapse and cause the formation of electrospun fibers with different cross-sectional shapes, including belts, ribbons, hollow filaments, fibers with an elliptical cross section, etc.; see Fig. 5. Solvent evaporation effects were modeled by nonlinear mass diffusion transfer to estimate the transient solvent concentration profiles in the jets (Wu, Salkovskiy, and Dzenis, 2011). Furthermore, solvent evaporation strongly affects the morphology and porosity of the surface of electrospun nanofibers (Srikar *et al.*, 2008). It was shown that the characteristic times of (i) polymer-solvent mutual diffusion, (ii) solvent evaporation, and (iii) phase separation of immiscible components influence the ultimately achieved nanofibers, which can be smooth, exhibit corrugations as displayed in Fig. 5(b) (Pai, Boyce, and Rutledge, 2009) or pores as displayed in Figs. 5(c) and 5(d) (Bognitzki *et al.*, 2001).

Since early studies in the late 1990s, it was found that during its path from the spinneret to the collector the electrified jet does not follow a straight trajectory but is instead affected by a variety of bending instabilities (Reneker *et al.*, 2000). An analogous effect is rapid whipping, which is also nonaxisymmetric and involves a deformation of the centerline of the electrified jet (Hohman *et al.*, 2001a, 2001b; Shin *et al.*, 2001). Other mechanisms observed are jet branching, consisting of secondary filaments separating from the main jet and possibly leading to fibers with complex shape (Yarin, Kataphinan, and Reneker, 2005), and buckling at the collector, which produces many different coiled
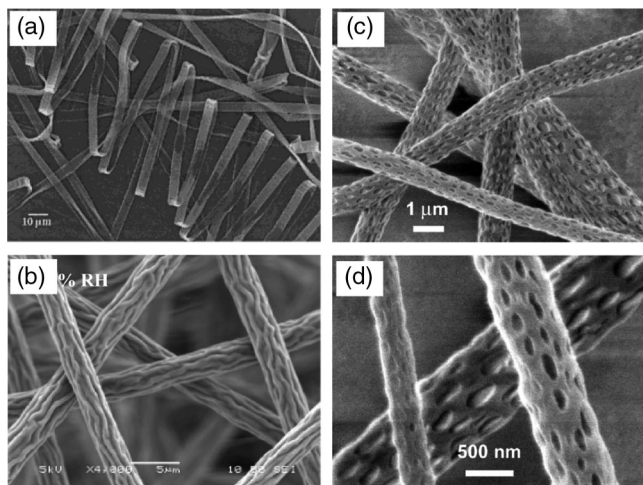
FIG. 5. (a) Electrospun ribbons made of poly(ether imide). Scale bar, 10 μm. From Koombhongse, Liu, and Reneker, 2001. (b) Corrugated fibers electrospun from a 30 wt % polystyrene-DMF solution under 22% relative humidity. Scale bar, 5 μm. Adapted from Pai, Boyce, and Rutledge, 2009. (c),(d) Porous fibers made of poly(L-lactide). Scale bar (c) 1 μm, (d) 500 nm. From Bognitzki *et al.*, 2001.
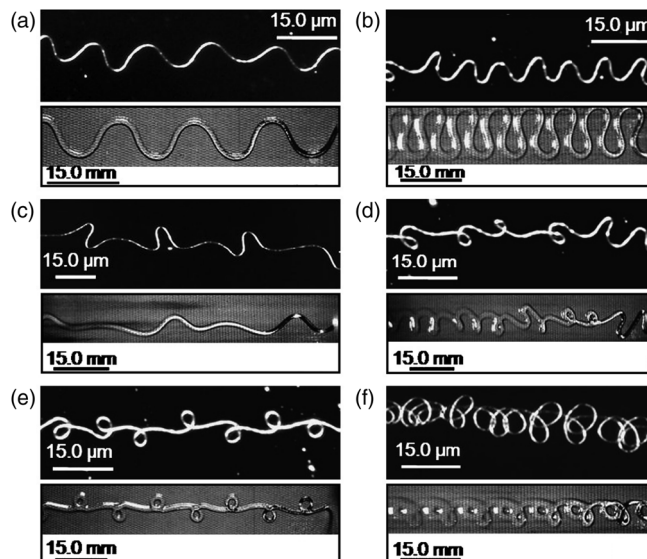

FIG. 6. Buckled patterns with various geometries formed by electrified jets of PEO in water (upper panel in each pair), collected on glass slides, and similar patterns produced by the buckling of uncharged, gravity-driven syrup jets (corresponding bottom panels). The fall of viscous threads leads to buckling patterns $\sim 10^3$ times larger than those from electrified jets. The obtained patterns include (a) sinusoidal features, (b) compressed meanders, (c) double meanders, (d) irregular features, (e) elongated figures of eight, and (f) coils. (Top panels) From Han, Reneker, and Yarin, 2007. (Bottom panels) Adapted from Chiu-Webster and Lister, 2006.

geometries, as displayed in Fig. 6 (Han, Reneker, and Yarin, 2007). Buckling effects are superimposed on those from bending instabilities and resemble those previously observed with larger nonelectrified jets (Chiu-Webster and Lister, 2006). The buckled coils found in electrospinning experiments show typical diameters in the range of a micrometer up to tens of micrometers, and patterns built at megahertz characteristic frequencies, depending on the jet velocity and viscoelastic properties. While the origin of bending instability is in the existence of lateral forces of electric origin, which appear at any curved section of a jet and lead to further bending, buckling arises from compressive forces acting along the jet from an obstacle. In this sense, buckling is a close counterpart of the classical elastic buckling of compressed columns discovered and explained by Euler (Landau and Lifshitz, 1970). Interested readers are referred to works dedicated to the theory of buckling of free liquid jets (Tchavdarov, Yarin, and Radev, 1993; Yarin, 1993).

B. Experimental parameters

The electrospinning is a process dependent on a number of governing parameters (Theron, Zussman, and Yarin, 2004). Ideally, by optimizing the set of these variables, an experimentalist can obtain nanofibers with desired composition and morphology. For this reason, theory and models of electrified jets also carefully consider these parameters and generally start from them to properly describe the process (Reneker *et al.*, 2000; Fridrikh *et al.*, 2003). The values of many of these parameters (so-called primary parameters) can be directly controlled by experimentalists (such as chemicals, solution concentration, and the setup parameters). However, other quantities are not chosen directly but depend in turn on the values of the primary parameters. These aspects make optimizing the overall process quite complex and also

highlight how important modeling can be to better rationalize observed phenomena, to identify most relevant variables that affect the formation of nanofibers, and to provide suitable ranges or starting values of relevant parameters to guide the experiments. In pioneering papers (Doshi and Reneker, 1995), the electrospinning parameters were grouped into three main classes:

(i) *Variables related to solution properties.*—These parameters depend on the used polymer species and their molecular weight, concentration, and elastic relaxation time, as well as on the solvent used; they include the solution density, viscosity, electrical conductivity, dielectric constant, and surface tension. In addition, the solvent properties include its volatility, determining the evaporation rate.

(ii) *Variables related to the used setup.*—These parameters include the applied electric potential difference $\Delta\Phi_0$, the solution flow rate Q, the distance between the spinneret and the collector h, and the internal diameter of the spinning needle.

(iii) *Variables related to the ambient.*—These parameters include relative humidity, temperature, and pressure.

The various classes of parameters are summarized in Table I.

The influence of the solution and setup parameters or of combinations of them on the dynamics of electrified jets and on the morphology of electrospun nanofibers was investigated

TABLE I.   Different classes of process parameters in electrospinning. Quantities used in models are reported with their symbol and Gaussian (cgs) units. Relevant references are also highlighted for each class of parameters.

	Primary parameters (directly chosen)	Secondary parameters (dependent on the primary ones)	
Solution properties	Polymer species Solvent species Solution concentration (C_p, mol cm^{-3}) Polymer molecular weight	Solution density (ρ, g cm^{-3}) Dynamic viscosity (μ, g cm^{-1} s^{-1}) Conductivity (σ_e, s^{-1}) Surface tension (α, g/s^2) Relaxation time (θ, s) Dielectric constant (ε)	Deitzel, Kleinmeyer, Harris, and Beck Tan (2001), Megelski *et al.* (2002), Theron, Zussman, and Yarin (2004), Jarusuwannapoom *et al.* (2005), Shenoy *et al.* (2005), Thompson *et al.* (2007), and Montinaro *et al.* (2015)
Setup settings	Applied voltage bias ($\Delta\Phi_0$, statV) Solution flow rate (Q, cm^3/s) Interelectrode distance (h, cm) Needle internal diameter	E, Electric field (statV cm^{-1})	Deitzel, Kleinmeyer, Harris, and Beck Tan (2001), Megelski *et al.* (2002), Theron, Zussman, and Yarin (2004), Thompson *et al.* (2007), and Montinaro *et al.* (2015)
Ambient properties	Atmosphere composition Atmosphere pressure Relative humidity Temperature (T, K)		Megelski *et al.* (2002), Casper *et al.* (2004), Thompson *et al.* (2007), Wang *et al.* (2007), Pai, Boyce, and Rutledge (2009), and Fasano *et al.* (2015)

in several studies (Deitzel, Kleinmeyer, Harris, and Beck Tan, 2001; Megelski *et al.*, 2002; Theron, Zussman, and Yarin, 2004; Jarusuwannapoom *et al.*, 2005; Shenoy *et al.*, 2005; Thompson *et al.*, 2007; Montinaro *et al.*, 2015). Other works focused on the effects of the ambient variables, particularly on humidity that is relevant for controlling the surface morphology and porosity of nanofibers (Casper *et al.*, 2004). Recent experiments showed that performing electrospinning in a controlled nitrogen atmosphere [Fig. 7(a)] might be useful for reducing the surface roughness of nanofibers, as well as for improving light emission properties of fibers made of conjugated polymers, because of the reduced incorporation of oxygen in the jets (Fasano *et al.*, 2015).

Finally, it should be mentioned that the polymer solution can be doped in various ways, particularly by adding nanoparticles with the aim of realizing nanocomposite fibers. Classes of quantum dots and of other nanoparticles used in electrified jets include those made of metals (Au, Ag), semiconductors (CdS, CdSe, ZnSe, ZnS), oxides (ZnO, Fe_3O_4, silica, titania), minerals such as hydroxyapatite and tricalcium phosphate, two-dimensional (2D) materials, carbon nanotubes, etc. (Dror *et al.*, 2003; Salalha *et al.*, 2004; Schlecht *et al.*, 2005; Sui, Shao, and Liu, 2005; Liu *et al.*, 2006; Lu, Wang, and Wei, 2009; Zhang *et al.*, 2016; Resta *et al.*, 2017). Because nanoparticles are dispersed in the solution, the polymer component works as a three-dimensional (3D) topological network, with the particles constituting distributed solid domains. These can significantly affect the jet rheology and dynamics, as highlighted by dedicated models (Lauricella, Pisignano, and Succi, 2017).

C. Electrified jet engineering

Using a planar collecting surface, electrified jets produce a random distribution of nanofibers on the plane connected to the counterelectrode, as shown in the central panel of Fig. 2, with a layer-by-layer stacked deposition along the direction

perpendicular to that surface. This is fine for some applications, such as for building filters or nonwoven mats for catalysis or textiles, but for other applications parallel nanofibers or nanofibers arranged in different architectures are much more convenient. To this aim, collector geometries were engineered in various ways to achieve contraction of the pattern of the electric field lines on sharp edges and, consequently, desired assemblies of nanofibers (Theron, Zussman, and Yarin, 2001; Zussman, Theron, and Yarin, 2003; Sundaray *et al.*, 2004; Teo and Ramakrishna, 2006). For instance, it was found that nanofibers can be obtained in almost uniaxially oriented arrays [Figs. 7(b)–7(e)] between electrodes with parallel conductive regions separated by a gap (Li, Wang, and Xia, 2003, 2004; Xie *et al.*, 2010). Upon approaching such regions, the electrified jet experiences two electrostatic forces. One is due to the electrospinning electric field, while the other is the attractive interaction between advection charges in the jet and the corresponding image charges in the collector electrodes. The combination of the two forces makes fibers stretch across the gap between the conductive regions. The effects of residual charges and of the gap size on fiber alignment were studied by numerical simulations, and the alignment of fibers was found to improve upon increasing the gap distance from 3 to 8 mm (Liu and Dzenis, 2008). Another successful method consists of collecting nanofibers on rotating cylinders (Sundaray *et al.*, 2004) or sharp disks (Theron, Zussman, and Yarin, 2001). This approach might also lead to extra pulling and stretching of the electrified jets and possibly to an enhanced order of polymer macromolecules in nanofibers. Magnetic-field-assisted electrospinning has also gained importance as a method to align nanofibers that incorporate magnetic particles (Rahmani, Rafizadeh, and Afshar Taromi, 2014; Mei, Song, and Liu, 2015; Huang *et al.*, 2016; Guarino *et al.*, 2019). Pioneering experiments showed that magnetic fields might be more efficient than electric fields in aligning fibers into parallel arrays (Yang *et al.*, 2007). A conceptually different
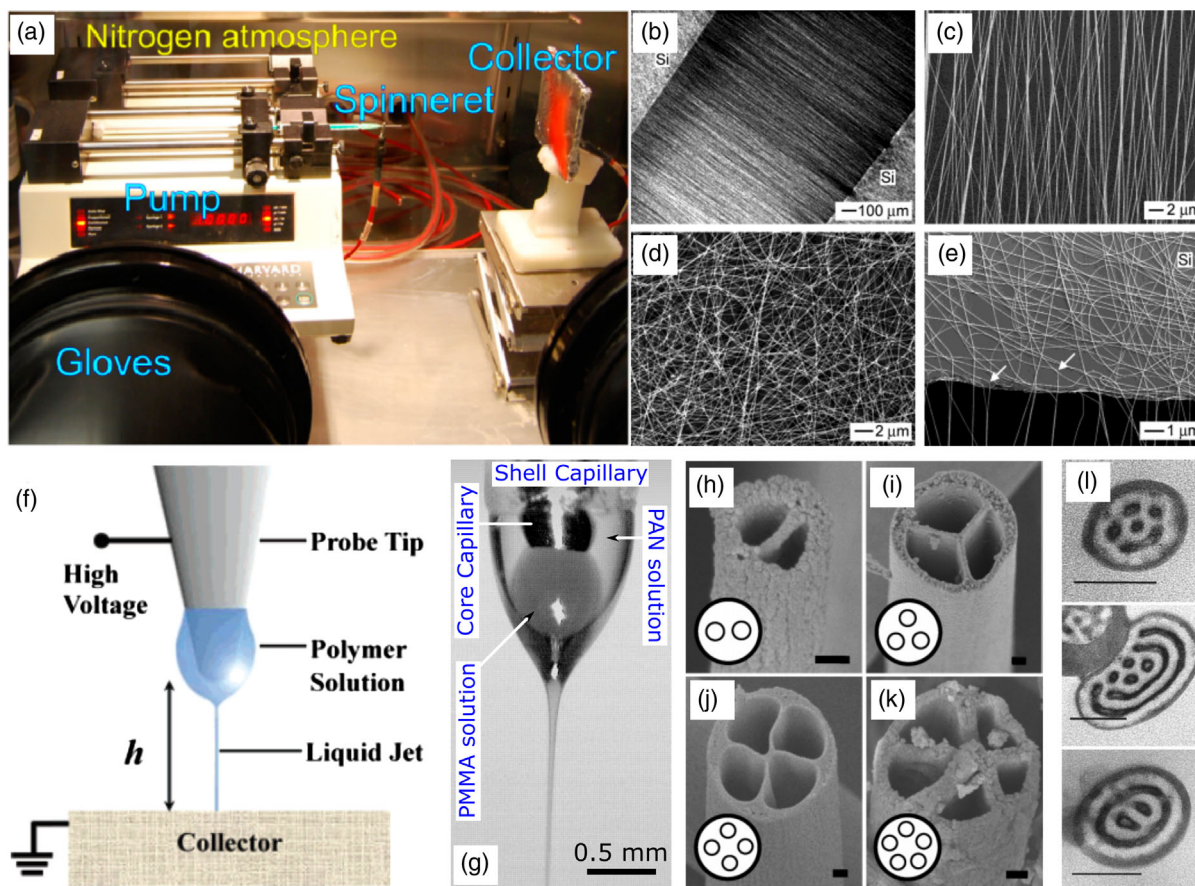
FIG. 7. Examples of process engineering. (a) Setup for producing electrified polymer solution jets in a nitrogen atmosphere. From Fasano *et al.*, 2015. (b)–(e) Images of uniaxially aligned arrays of electrospun polymer nanofibers produced with a gap collector: (b) dark-field optical micrograph, and (c),(d) scanning electron microscopy (SEM) images comparing (c) aligned and (d) random fibers deposited onto a flat surface. (e) A SEM micrograph of the gap edge is also shown, displaying a transition from aligned to random nanofibers. From Li, Wang, and Xia, 2003. (f) Scheme of the near-field electrospinning process. Here *h* is from a few hundred micrometers to a few millimeters. From Sun *et al.*, 2006. (g) Compound droplet and bicomponent Taylor cone encompassing two different polymer solutions in coaxial electrospinning. Polymers used are poly(methyl methacrylate) (PMMA) for the core and polyacrylonitrile (PAN) for the shell. Adapted from Zussman *et al.*, 2006. (h)–(k) SEM micrographs of multichannel tubes with variable diameter and channel number obtained by a multichannel spinneret. Scale bars, 100 nm. From Zhao, Cao, and Jiang, 2007. (l) Transmission electron micrographs of cross sections of annealed block-copolymer fibers. Scale bars, 100 nm. From Kalra *et al.*, 2009.

approach for controlling fiber positions [Fig. 7(f)] consists of reducing the distance between the spinneret and the collecting surface to the subcentimeter or even submillimeter scale, thus exploiting the initial, straight part of the jet (i.e., before the onset of bending instabilities), in so-called near-field electrospinning (Sun *et al.*, 2006; Chang, Limkrailassiri, and Lin, 2008).

Electrified jets were also engineered to deliver more than one polymer compound in coflows to obtain nanofibers with core-shell or even multicomponent architecture or hollow nanofibers (following the removal of an internal sacrificial material). Core-shell structures in fibers are important for a wide range of technologies, including waveguides with layers showing refractive index contrast, electrical nanowires with insulating sheath, polymer structures for drug delivery, nanofluidics, and biological scaffolds. Coaxial electrospinning was implemented by means of concentric needles delivering different polymer solutions (Loscertales *et al.*, 2002; Sun *et al.*, 2003; Li and Xia, 2004a; Loscertales *et al.*, 2004; Yu, Fridrikh, and Rutledge, 2004; Zhang *et al.*, 2004; Zussman *et al.*, 2006; Gañán-Calvo *et al.*, 2007). A bicomponent Taylor cone can be obtained in this way [Fig. 7(g)]. In coaxial jets with two immiscible solutions, instabilities might be reduced and the flow of the internal solution is supported by the external one, thus making it possible to use as core fluid a solution that does not on its own have a sufficiently viscoelastic behavior to form electrospun fibers. This is the case of many solutions of light-emitting or conductive polymers, low-molar-mass molecules, biomolecules, and drugs to be encapsulated for controlled and sustained delivery. The method can be scaled up to more fluids, and nanofibers with several either concentric or parallel layers or cavities [Figs. 7(h)–7(k)] formed by means of spinnerets featuring three or more fluidic channels (Zhao, Cao, and Jiang, 2007; Chen *et al.*, 2010). An application of multifluid jets was shown in confining block copolymers within the small volumes of individual nanofibers
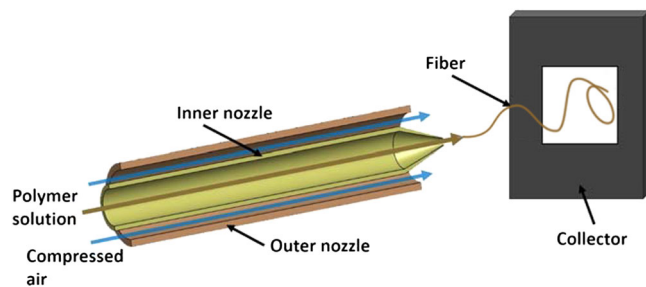
FIG. 8. Scheme of a solution-blowing setup and process. Adapted from Polat *et al.*, 2016.

to study the resulting microphase configuration (Kalra *et al.*, 2006, 2009; Ma *et al.*, 2006). For instance, nanofibers with a block-copolymer core and a shell made of silica or of a polymer with high glass transition temperature can be annealed to induce ordered domains in the internal region [Fig. 7(l)]. Core-shell nanofibers can also be electrospun from a single nozzle by using emulsions of two polymers in a single solvent as a working fluid (Bazilevsky, Yarin, and Megaridis, 2008; Yarin, Pourdeyhimi, and Ramakrishna, 2014). In the case of emulsion spinning, the dispersed phase forms the core, whereas the continuous phase forms the shell. Recently emulsion spinning of core-shell nanofibers found an application in generating self-healing vascular nanotextured composite materials (Yarin *et al.*, 2019).

D. From electrospinning to solution blowing

Methods to enhance the throughput in producing nanofibers could make use of forces other than electrostatic ones. For instance, a gas stream delivered by a nearby distributer would support polymer solution jets through additional shearing and stretching. Such gas-assisted electrospinning or electroblowing methods (Um *et al.*, 2004; Wang *et al.*, 2005; Hsiao *et al.*, 2012) might be implemented through gas distributers surrounding the spinneret and allow thinner nanofibers to be obtained. In fact, coflowing subsonic gas jets have been used

for a long time to assist the formation of microscopic fibers in meltblowing (Pinchuk *et al.*, 2002; Fedorova and Pourdeyhimi, 2007; Yarin, Pourdeyhimi, and Ramakrishna, 2014). These technologies start from polymer melts, and at variance with electrospinning, the bending instability in this case arises purely aerodynamically due to a distributed lateral force acting on curved sections of polymer jets, driving the instability process. To obtain nanofibers, air-jet spinning, i.e., solution blowing (Sinha-Ray, Yarin, and Pourdeyhimi, 2010a) rather then meltblowing is used. This process is schematized in Fig. 8. The needle is concentric with the nozzle issuing the air jet at a given delivery pressure. Solution blowing has attracted increasing interest due to its superior throughput and capability to generate thin (20–50 nm) nanofibers (Sinha-Ray *et al.*, 2013, 2015; Yarin, Pourdeyhimi, and Ramakrishna, 2014; Daristotle *et al.*, 2016; Polat *et al.*, 2016). The method has already been scaled up to industrial equipment (Kolbasov *et al.*, 2016). As shown in Fig. 9(a), in this technique polymer solutions are employed similarly to electrospinning; however, the jet is issued into a coflowing subsonic or supersonic gas jet without the application of an external electric field, similarly to meltblowing. Solution blowing shares many of its process parameters with electrospinning, including solution properties (polymer and solvent species, concentration, zero-shear viscosity, and elastic relaxation time). Also of importance are several variables related to the used setup (particularly solution flow rate, and needle gauge), and such ambient parameters as humidity and temperature. Here aerodynamically driven bending perturbations can be triggered by turbulence of the surrounding gas flow, whereas polymer viscoelasticity, similar to electrospinning, plays a restraining role. In some cases, two streams of polymer solution and pressurized gas can also be generated by means of a commercially available airbrush such as that displayed in Fig. 9(b) (Tutak *et al.*, 2013). Solution-blown nanofibers have been used to obtain carbon nanotubes (Sinha-Ray, Yarin, and Pourdeyhimi, 2010b), for filter media (Zhuang *et al.*, 2013; Liu *et al.*, 2019), for biomedical engineering (Khansari *et al.*, 2013; Tutak *et al.*, 2013; Behrens *et al.*, 2014; Behrens *et al.*,
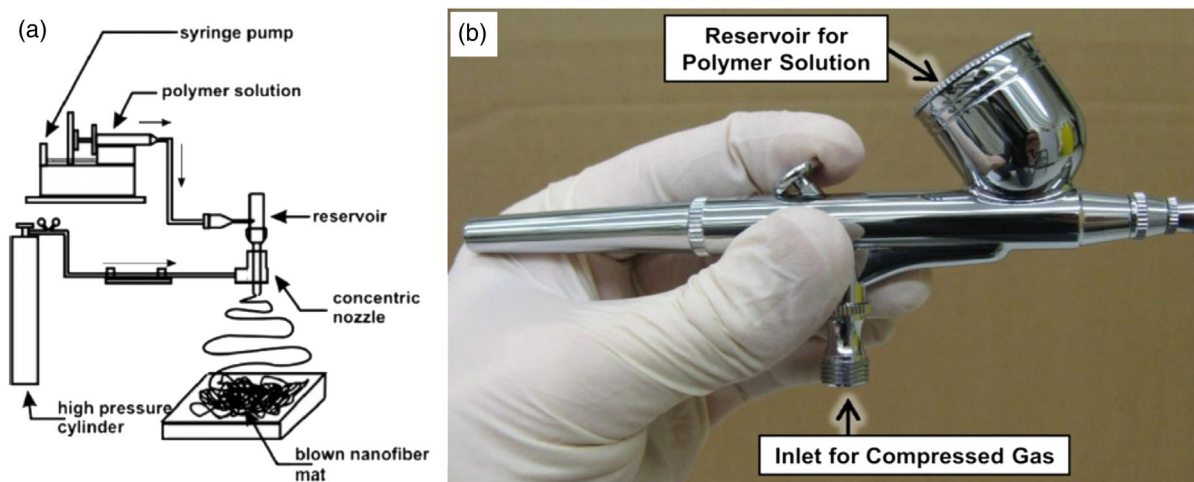

FIG. 9. Scheme of a solution-blowing bench setup. From Sinha-Ray, Yarin, and Pourdeyhimi, 2010b. (b) A commercially available airbrush for portable solution blowing of nanofibers. From Tutak *et al.*, 2013.

2015; Magaz *et al.*, 2018), and for the formation of self-healing vascular nanocomposites (Yarin *et al.*, 2019).

Another fundamental feature of liquid jets concentric with gas flows is the resulting hydrodynamic flow-focusing effect driven by the external fluid. For example, this can be implemented in a configuration with the external gas stream surrounding a manifold jet in turn composed by two immiscible solutions, and with the internal capillary delivering the core fluid protruding by about one diameter length from the outer capillary, delivering the sheath fluid. Such arrangement was analyzed in terms of working conditions (solution viscosities, capillary diameters, gas pressure, etc.) and found to overcome surface tension effectively and to lead to the generation of continuous, steady capillary jets down to the submicrometer cross-sectional size (Gañán-Calvo, 2007).

IV. REQUIREMENTS OF THEORETICAL METHODS FOR MODELING ELECTRIFIED AND BLOWING LIQUIDS

Modeling of electrified and solution-blown fluids is a practical tool to achieve reliable predictions of the geometries and sizes of nanofibers, assembly, or internal molecular structure, guiding the choice of specific process parameters. For instance, this could aim at providing a likely starting point for the fabrication process of fibers with desirable geometry or architecture, thus significantly saving experimental resources and time. Modeling would be even more important to rationalize the fundamental properties of polymer solutions, in particular, their spinnability in fiber-forming processes, which are predominantly uniaxial elongation processes. The description is based on a system of highly nonlinear partial differential equations (PDEs) for the electrified or blowing jet dynamics. In principle, this could be tackled by standard grid methods, such as finite differences or finite volumes. However, the large material stretching in space and the characteristic times of the competing physical phenomena in electrospinning and solution blowing are such that they make a standard grid approach (the Eulerian approach) extremely challenging on computational grounds. The main problem is the major stretching of polymer jets accompanied by reduction in their cross-sectional size from, say, ∼100 μm at the exit of the nozzle down to 1 μm or less at the collector. Even when modeling the shrinkage of the polymer jet via a constitutive law, the jet representation would require at least ten grid points; hence, to correctly describe a jet diameter of about 1 μm at the collector the length scale would be 0.1 μm. With a static Eulerian grid, covering a 3D cubic domain of about 10 cm would then require 10^{18} grid points. The simple storage of a corresponding array of a scalar variable in double floating numbers would require 8×10^6 Tbytes, which will be out of reach for any computer in the foreseeable future.

Of course, this naive estimate can be considerably softened by resorting to moving-grid Lagrangian techniques (Sec. V.B), whereby high resolution would also be put in place where needed, i.e., in the vicinity of the jet, by meshing adaptively "on the fly" in the course of the simulation (Sec. V.C.4). The corresponding procedure is computationally less demanding. For instance, the discretization of a jet length equal to 300 cm

with a typical length step of 0.02 cm would be stored in only 15 000 grid points (120 kbytes in double floating numbers to store an array of a scalar variable). The Lagrangian approach is one of the two options traditionally used in fluid mechanics, and it implies that the grid follows the individual fluid particles, i.e., the grid is frozen in the fluid rather than in an arbitrary surrounding space as in the case of the Eulerian grid (Lamb, 1959; Loitsyanskii, 1996; Batchelor, 2002). Moreover, this strategy provides low data traffic, low input or output operations, and lean communication between threads on parallel machines. The last point is of extreme importance, since it is increasingly apparent that as performance ramps up, accessing data could become more expensive than to perform floating-point operations (Succi *et al.*, 2019).

The discrete-particle representation is an approximation of the fluid in a quasi-one-dimensional (1D) object, but in problems related to electrospinning, meltblowing and solution blowing, and hydroentanglement (Reneker *et al.*, 2000; Yarin, Koombhongse, and Reneker, 2001a; Yarin, Sinha-Ray, and Pourdeyhimi, 2011; Yarin, Pourdeyhimi, and Ramakrishna, 2014; Sinha-Ray *et al.*, 2015; Li *et al.*, 2019a, 2019b), it has a substantial advantage in that particles naturally flow in the spatial regions where the relevant physics of the jet takes place.

In fact, denoting with r the jet cross-sectional radius and with z the longitudinal coordinate along which the jet is delivered, jets can frequently be considered slender bodies with slow changes of r along z, i.e., with $|dr/dz| \ll 1$. This is also referred to as the slenderness assumption (Eggers, 1997). These long and thin fluid threads, whose velocity fields are directed mostly along one axis, can be well described by quasi-1D fluid flows. In this framework, the velocity field in the radial direction is usually expanded to the lowest-order terms, which should be sufficient to describe the radial motion (Lee, 1974; Pimbley, 1976; Entov and Yarin, 1984b; Yarin, 1993; Eggers and Dupont, 1994). Hence, equations of motion (EOM) are written only for the expansion coefficients depending on the axial variable z. Nonetheless, observables related to the remaining dimensions such as radial velocity, curvature radius, and jet cross section survive, but they are now dependent on the 1D expansion coefficients. This is the core of the quasi-1D description, which can be implemented in jets, waves, drop dynamics, and thin-film flows (Middleman, 1995). In the jet context, several other assumptions are usually included in the quasi-1D description (Yarin, 1993; Eggers, 1997; Eggers and Villermaux, 2008), such as incompressible velocity field, fluid volume preservation, locally axisymmetric flow, isotropic expansion or contraction in the jet cross section, and absence of shearing forces on the lateral jet surface. However, some experimentally relevant cases may go beyond one or more of these assumptions (e.g., considering an elliptical cross section for the thread) so that a critical evaluation of all approximations adopted in each specific model should always be addressed. Quasi-1D equations for electrified jets are presented in Sec. V.A.3 in their EHD form [see Eqs. (5)–(8)], and in Sec. V.A.4 in their fundamental Lagrangian descriptions; see Eq. (11). The limitations of this approach, leading to the need for a fully 3D representation for
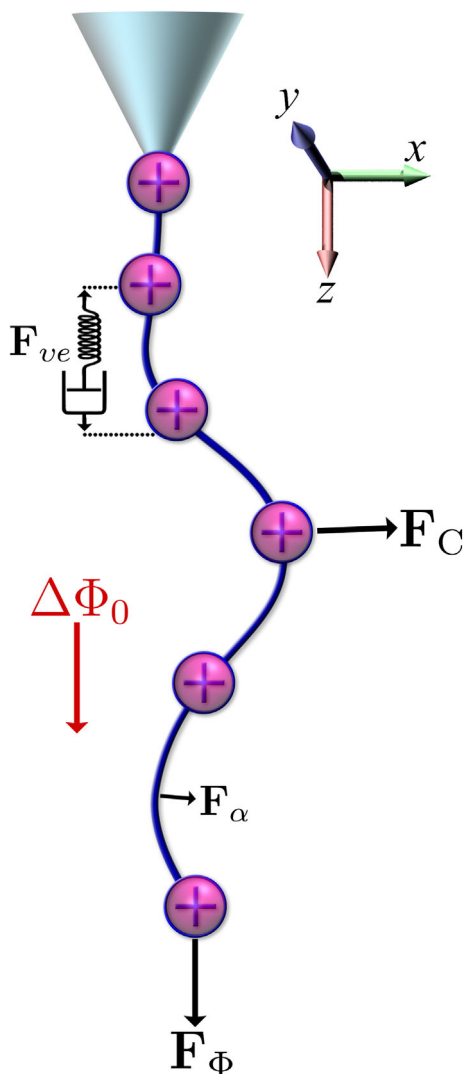
FIG. 10. Sketch of the Lagrangian representation for electrospun jets. Each discrete element representing a jet segment is drawn by a bead, with a plus sign denoting the positive charge of the segment. The scheme shows the viscoelastic force $\mathbf{F}_{ve}$, the surface tension force $\mathbf{F}_\alpha$ pointing to the center of curvature to restore a rectilinear shape, and the Coulomb repulsive term $\mathbf{F}_C$, which is in the opposite direction with respect to the local center of curvature, thus laterally destabilizing the filament. The cone at the top of the figure represents the nozzle, whereas the external electric potential bias $\Delta\Phi_0$ provides a field indicated by the red arrow, and the electric force term $\mathbf{F}_\Phi$ on the jet beads.

comprehensively catching bending jets, are discussed in Sec. V.B.3.

In fact, in Lagrangian descriptions of a jet as n individual particles (Secs. V.B and V.C), schematized in Fig. 10, the computational complexity of solving the associated system of equations scales like n^2, mostly on account of unscreened electrostatic interactions (all-to-all, long-range coupling). This is the so-called direct summation technique, where each particle interacts nonhierarchically with all other particles. With the simpler paradigm of direct summation, on a standard personal computer the number of viable particles is limited to

about 1000, which based on the existing literature appears to be largely sufficient to deliver informative insights into the jet behavior. Nonetheless, more sophisticated approaches imply a hierarchical organization of the long-range Coulomb interactions, whose complexity scales like $n\log(n)$. In this framework, the charge elements of the discretized jet are recursively clustered and the monopole coefficients of the clusters are computed (Kowalewski, Barral, and Kowalczyk, 2009). The scheme can be augmented by including higher orders of the multipole expansion, usually referred to as the fast multipole method.

These considerations are also valid within the framework of parallel computing. Two main paradigms are usually pursued for exploiting the parallelism. The first is the replicated data (RD) strategy, where fundamental data of the simulated system are reproduced on all processing nodes. The second paradigm is based on the domain decomposition (DD) strategy, which exploits the decomposition of the space in subdomains distributed over several processors so that each process deals only with its subset of particles. The RD strategy provides satisfactory results of parallel efficiency in simulations on up to 100 processors, involving up to 30 000 particles (Smith and Forester, 1996). Given the small number of particles used to represent the jet, practical cases (Lauricella, Pontrelli, Coluzza *et al.*, 2015a; Lauricella *et al.*, 2016) have shown that such volume of data is by no means prohibitive on current parallel codes exploiting the RD strategy. However, all floating-point operations should be distributed in equal portions (as much as possible) for each processor to balance the load over participated processors. The load balancing is crucial since it guarantees that the computational work is performed cooperatively and simultaneously on all processing nodes.

In the parallel framework, all of the n-body force terms, such as Coulomb intrajet forces, must be obtained as a global sum of the contributing terms calculated over all nodes. As a consequence, a communication overhead is paid whenever the forces should be updated. Both DD and RD strategies pay a time lag, which depends on the information size to be communicated. Nonetheless, the exchanged information could be collected in smaller pieces to mitigate the latency time in data communication. For instance, the aforementioned fast multipole method may be used to pass cluster information of the repulsive Coulomb interaction, thus decreasing the communication data size. Although this is just a sample of the types of problems encountered in parallel coding, an efficient numerical implementation should always consider a fair trade between the largest distribution of computational work and the smallest data communication between processors.

To describe electrified and solution-blown jets, a number of parameters from experiments are generally needed. In addition, different models might have specific regions of validity. For instance, the validity of polymer network modeling (Sec. V.D) is restricted to the initial part of the jet, near the Taylor cone, where elastic elongation is still possible. Assuming mass conservation in this region of the jet, details are required relating to jet radius, velocity, and strain rate. In addition, data on the polymer solution are required such as the shear viscosity, concentration, and type of solvent (e.g., θ

solvent). The voltage applied in electrospinning, needle-collector distance, needle internal diameter, and bulk velocity of the polymeric fluid in the needle, as well as the mass and charge density, zero-shear viscosity, elastic modulus, and surface tension of the used polymer solutions, are generally the parameters needed as input of simulation tools based on Lagrangian models of electrospinning (Lauricella, Pontrelli, Coluzza *et al.*, 2015a). Nonetheless, simulating advanced electrospinning experiments may require further input parameters. As an example, magnetic and gas-assisted electrospinning simulations (Sec. V.C) need the magnetic-field and gas velocity flow field as an extra parameter, respectively. Whenever the case, additional input parameters are introduced later.

V. MODELING METHODS FOR ELECTROSPINNING

In the following we present the current status of modeling methods developed for electrified polymer solution jets, not just as a list of sequential findings but with a logical flow in which the historical background will be accompanied by a critical review of research progress.

A. Electrohydrodynamic models

1. Taylor cone

As explained in Sec. II, the liquid in a static drop attached to an electrode located at some distance from a counterelectrode can be considered a perfect ionic conductor, even though its conductivity might be low (Taylor, 1964; Ramos and Castellanos, 1994a). As a result the excess anions or cations have enough time to escape to the droplet surface, on which they are distributed nonuniformly to maintain zero electric field inside the liquid. This means that droplet surface is equipotential. The shape evolution of small droplets attached to a conducting surface and subjected to electric fields has been studied both experimentally and numerically (Reznik *et al.*, 2004; Collins *et al.*, 2008). The following scenarios can be distinguished for either perfectly conducting (Reznik *et al.*, 2004) or moderately conducting (Collins *et al.*, 2008) drops:
  (i) In sufficiently weak electric fields, droplets are stretched by the electric Maxwell stresses in air and acquire steady-state shapes, where equilibrium is achieved by means of surface tension.
  (ii) In stronger electric fields, the Maxwell stresses overcome surface tension and jetting can be initiated.
Conditions corresponding to (i) and (ii) can be called subcritical and supercritical, respectively. The ultimate equilibrium droplet shape (i.e., the "critical" condition) resulting from the competition of electric and surface forces reveals the Taylor cone configuration (Saville, 1997; Yarin, Koombhongse, and Reneker, 2001b; Yarin, Pourdeyhimi, and Ramakrishna, 2014). This corresponds to a solution in power-law form of the Laplace equation for the electric potential Φ in the surrounding air. Such a solution is scaling invariant over different length scales of its variables, a property consisting of reproducing itself at different timescales and space scales (Barenblatt, 1994), which is also called self-similarity.
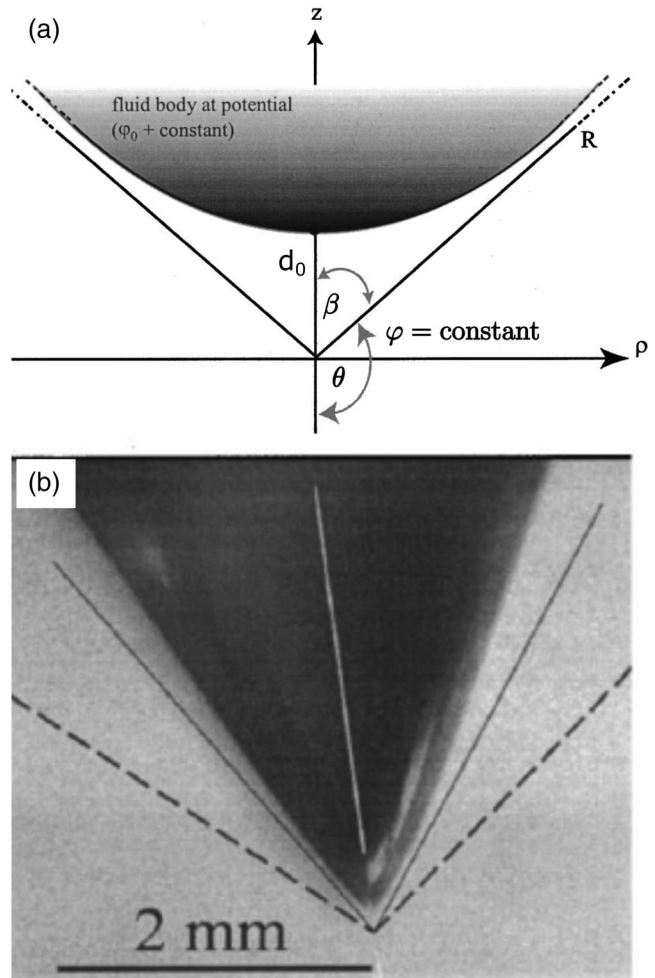

FIG. 11. (a) Axisymmetric, "infinite" fluid body kept at potential, $\Phi_0 = \varphi_0 + \text{const}$ at a distance d_0 from an equipotential plane sustained at $\Phi = \text{const}$. (b) Critical shape observed for a pendant droplet in this configuration. The half angle associated with the self-similar solution for the Taylor cone is indicated by the dashed lines. The tangent to the experimentally observed droplet of the polymer solution has half angle 31° (shown by solid line). Adapted from Yarin, Koombhongse, and Reneker, 2001b.

An axisymmetric liquid body kept at a potential $\varphi_0 + \text{const}$ with its tip at a distance d_0 from an equipotential plane that might be the counterelectrode in electrospinning experiments is considered in Fig. 11(a), where the distribution of the electric potential $\Phi = \varphi + \text{constant}$ is described in terms of the spherical coordinates R and θ (Yarin, Koombhongse, and Reneker, 2001b). The potential φ_0 can always be expressed in terms of the surface tension coefficient α and of d_0, i.e., $\varphi_0 = C(d_0\alpha)^{1/2}$, where C is a dimensionless factor, which follows from the dimensional analysis. In addition, also because of the dimensional arguments, the general representation of the electric potential φ is $\varphi = \varphi_0 F_1(R/d_0, \theta)$, where F_1 is a dimensionless function of the R/d_0 ratio and of the θ angular coordinate (Yarin, 2012). Hence, the value of the potential Φ throughout the space that surrounds the liquid droplet is given by

$$\Phi = (d_0\alpha)^{1/2}F(R/d_0, \theta) + \text{const}, \qquad (1)$$

where $F = CF_1$ is a dimensionless function. At distances $R \gg d_0$, equivalent to the mathematical assumption $R \to \infty$, one can assume that the influence of the gap d_0 is small. Under this condition, the function F should approach a power-law scaling form (Yarin, 2007):

$$F(R/d_0, \theta) \approx (R/d_0)^{1/2}\Psi(\theta), \qquad (2)$$

where $\Psi(\theta)$ is a dimensionless function. Finally, Eq. (1) takes the asymptotic self-similar form, independent of d_0:

$$\Phi = (\alpha R)^{1/2}\Psi(\theta) + \text{const}. \qquad (3)$$

The solution in Eq. (3) should also satisfy the Laplace equation (Landau, Lifshitz, and Pitaevskii, 1984; Smythe, 1989; Feynman, Leighton, and Sands, 2006). Thus, one finds the function Ψ (Taylor, 1964):

$$\Psi(\theta) = P_{1/2}(\cos\theta), \qquad (4)$$

where $P_{1/2}$ is the Legendre function of the order of $1/2$, which takes value $P_{1/2}(\cos\theta) = 0$ whenever $\theta = \theta_0$, with θ_0 the angle value matching the equipotential condition $\Phi = \text{const}$. In other words, the free surface becomes equipotential only when θ corresponds to the single zero of $P_{1/2}(\cos\theta)$ in the range $0 \le \theta \le \pi$, which Taylor found to be equal to $\theta_0 = 130.7°$ (Taylor, 1964) using the tabulated values (Gray, 1953) of the function $P_{1/2}(\cos\theta)$. According to the self-similar equilibrium solution, the fluid body should so be enveloped by a cone with the half angle at its tip, $\beta_T = \pi - \theta = 49.3°$, i.e., the half-angle value associated with the Taylor cone [Fig. 11 (b)]. Other studies on self-similar solutions analyzed dielectric liquids with varied permittivity (Ramos and Castellanos, 1994a, 1994b), finding that stationary cones can be formed only for $\varepsilon > 17.6$ (in cgs). By including the effect of the deviation of the surface shape from the conic one, such an inferior limit for the permittivity was later increased to 22.2, corresponding to a half-angle value 39.25° (Zubarev, 2002). The local behavior of various physical quantities (e.g., fluid velocity, surface curvature, electric current) could be determined, analyzing the nonlinear dynamics of the liquid cone for inviscid incompressible fluids (Zubarev, 2002, 2006; Belyaev, Zubarev, and Zubareva, 2019).

Power-law scalings resulting in self-similar solutions like that shown in Eq. (3) are common in the boundary-layer theory (Zel'dovich, 1937; Schlichting, 1979; Zel'dovich, 1992; Yarin, 2007). In particular, such self-similar solutions for jets and plumes, considered to be issuing from a pointwise origin, in reality correspond to the non-self-similar solutions of the boundary-layer equations (the Prandtl equations) for jets and plumes that are issued from finite-size needles, at distances much larger than the needle size (i.e., such solutions constitute remote asymptotics). For instance, the self-similar solution for capillary waves generated by a weak impact of a droplet onto a thin liquid layer emerges at distances from the center of impact much greater than the droplet diameter (Yarin and Weiss, 1995; Yarin, Roisman, and Tropea, 2017). The

self-similar solution in Eq. (3), motivated by the same idea, was expected by Taylor to correspond to the limiting behavior of all non-self-similar solutions at $R \gg d_0$. In fluid dynamics, there are several contexts where self-similar asymptotics can be experimentally realized. For example, fluid flows involving boundary layers near a solid wall or free flows reveal the self-similar asymptotics, even though the experimental setup contains some details that are noncompliant with the assumptions of self-similarity (Yarin, 2007). In this situation, one can say that the flow pattern evolves to the self-similar solution, i.e., that a dynamic system evolves toward its attractor. Then, the non-self-similar solutions (e.g., the initial flow pattern) are "attracted" by the self-similar solutions. Indeed, the fact that the self-similar behavior can be experimentally realized directly evidences that it attracts the initially non-self-similar fluid flows, a behavior that is usually consistent with physical phenomena governed by parabolic PDEs for submerged jets (Schlichting, 1979; Yarin, 2007) and plumes (Zel'dovich, 1992). On the other hand, the self-similar Taylor cone solution, stemming from the elliptic Laplace equation, significantly disagrees with the experimental data (Yarin, Koombhongse, and Reneker, 2001b; Yarin, Pourdeyhimi, and Ramakrishna, 2014) for electrified polymer fluids, leading to the conclusion that realizing the self-similar solution could be experimentally impracticable. It was also shown, by means of numerical simulations, that it does not attract the transient evolution at the tip of the fluid cone (Reznik *et al.*, 2004). An analogous observation on a self-similar solution that does not attract the corresponding non-self-similar one was found in the problem described by the biharmonic (elliptic operator squared) equation, namely, in the case of a wedge subjected to a concentrated couple of forces at its tip. This is known as the Sternberg-Koiter paradox (Sternberg and Koiter, 1958; Barenblatt, 1996) in the theory of elasticity. In electrospinning, an approximate non-self-similar solution was found instead in the form of a prolate hyperboloid of revolution (Yarin, Koombhongse, and Reneker, 2001b; Yarin, Pourdeyhimi, and Ramakrishna, 2014), which has finite curvature at the tip; see Yarin, Koombhongse, and Reneker (2001b) for a detailed explanation of the procedure used to find this solution. Here we recall that the half-angle at the tip of the cone to which the hyperboloid leans is 33.5°, which is significantly smaller than the angle originally obtained for the Taylor cone (49.3°), and quite close to experimental data [Fig. 11(b)].

In experiments with water (Taylor, 1964), it would be difficult to approach the critical drop shape because perturbations disrupt the equilibrium much earlier, thus making it impossible to measure the critical half angle at the tip accurately. On the other hand, in experiments with polymer solutions perturbations are suppressed by the viscoelastic behavior of the fluid jet (Yu, Fridrikh, and Rutledge, 2006), and equilibrium can be approached closely [Fig. 11(b)]. Figure 12 shows the predicted and measured shapes of a polycaprolactone (PCL) droplet at different moments. The numerical predictions slightly underestimate the stretching rate, but the overall agreement is fairly good. The early supercritical regime leads to jets generated from the cones with half angles of 25° to 30°, which supports the assumption that the critical droplet shapes are close to those predicted with a half angle of
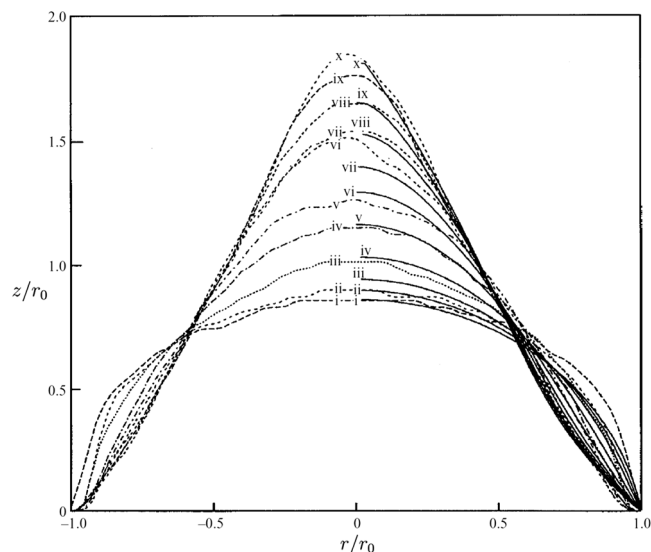
FIG. 12. Measured and predicted shapes (vertical coordinate z vs radial coordinate r) of a PCL droplet at different times during deformation under an applied electric field: (i) $t = 0$, (ii) 101.5, (iii) 201.5, (iv) 351.5, (v) 501.5, (vi) 601.5, (vii) 651.5, (viii) 701.5, (ix) 731.5, and (x) 756.5 ms. Both r and z are rescaled by the initial base radius r_0 of the droplet. Results from calculations are shown by solid lines on the right side of the drop (numerals are located at their tip points). The experimental shapes are plotted as dotted lines. On the left side of the drop, the values of the radial coordinate (here r) are made negative. Adapted from Reznik *et al.*, 2004.

33.5° rather than to 49.3° in this specific regime (Reznik *et al.*, 2004). However, this statement should be made with caution because in early supercritical dynamical cases half angles can be smaller because of the presence of the jet protrusion.

This dynamics strongly depends on the viscoelastic properties of the used fluid. For instance, experiments on drop evolution in a high-voltage electric field have also been reported with water (Zhang and Basaran, 1996), showing a behavior quite different from that of highly viscous and elastic fluids used in electrospinning. For low-viscosity liquids, with Ca in the range 10^{-5}–10^{-3} (Zhang and Basaran, 1996), electrospraying can occur; i.e., the dripping regime is easily reached, as described in Sec. II. Sometimes small droplet emission from the cone tip begins at half angles close to 45° (Michelson, 1990), and sometimes close to 49° (Fernandez de la Mora, 1992, 2007). The dynamical evolution of the fluid cone in presence of an electric field was theoretically investigated in the context of liquid-metal ion sources and found to reach an angle equal to the Taylor value (Zubarev, 2001; Suvorov and Zubarev, 2004; Boltachev, Zubarev, and Zubareva, 2008). The cone dynamics was also studied for a perfectly conducting liquid to describe the mode of drop formation changing from simple dripping to so-called micro-dripping (Notz and Basaran, 1999). Furthermore, the critical droplet shapes and the dripping regime from a liquid film of finite conductivity were carefully studied and numerically simulated in the framework of electrospray ionization, showing that EHD tip streaming phenomena do not occur if the liquid is perfectly conducting or perfectly insulating and

highlighting a universal scaling law for the size and for the charge carried by the droplets that are emitted (Collins, Harris, and Basaran, 2007; Collins *et al.*, 2013). Recent works aimed at also including the effects of charge relaxation to catch the transient EHD response in low-conductivity fluids (Gañán-Calvo *et al.*, 2016; Pillai *et al.*, 2016).

In general, dripping from low-viscosity liquids can lead to significant space charge from these small droplets. The backward electric effect of the charged droplets on the tip of the cone was shown to lead to the half-angle in the 32°–46° range (Fernandez de la Mora, 1992). On the contrary, since breakup of small threads and filaments is generally prevented by viscoelastic effects in electrospinning (Yarin, 1993; Reneker *et al.*, 2000; Yarin, Koombhongse, and Reneker, 2001a; Yarin, Pourdeyhimi, and Ramakrishna, 2014), it is highly unlikely that the half-angle values found in the experiments with electrospun polymeric liquids can be attributed to space charge effects.

2. Onset of electrified jets

Electrospun jets are straight in their initial path (Fig. 13), where the growing bending perturbations are still small (Reneker *et al.*, 2000; Yarin, Pourdeyhimi, and Ramakrishna, 2014). Indeed, the longitudinal stress σ due to the external electric field (acting on the charge carried by the jet) stabilizes the fluid filament for some distance from the nozzle (Reneker *et al.*, 2007). A similar trend was also noted in uncharged fluid threads of cylindrical shape, where the time of growth of the hydrodynamic instability was reported to scale logarithmically with the strain rate in hyperbolic extensional flow (Khakhar and Ottino, 1987). Furthermore, as long as the jet is sufficiently thick, it has a high bending stiffness since this stiffness scales with the jet cross-section radius
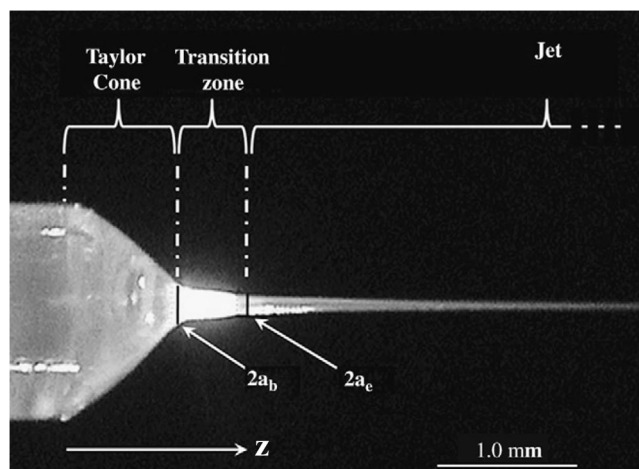
FIG. 13. Modified Taylor cone, with the transition zone, and the beginning of a thin, electrified polymer solution jet. Here the cross-sectional radii at the beginning and the end of the transition zone are denoted a_b and a_e, respectively. These quantities are measured by analyzing a 6 wt % aqueous solution of PEO (solution density $\cong 1$ g/cm^3, zero-shear viscosity 50 g cm^{-1} s^{-1}, surface tension = 61 g/s^2). Adapted from Han, Yarin, and Reneker, 2008.

as $\sim r^4$ (Reneker *et al.*, 2000; Yarin, Pourdeyhimi, and Ramakrishna, 2014). The combined effects of the bending stiffness and of the longitudinal stress thus lead to the initial straight path of the jet. A detailed investigation, including measurements of longitudinal stresses and thinning rates on a 6 wt % aqueous solution of PEO, found that longitudinal stress rescaled to the capillary pressure $\sigma r/2\alpha$ span approximately from 10 up to 100 in the straight path zone (Han, Yarin, and Reneker, 2008).

This straight region is relatively easy to investigate experimentally compared to that of the droplet-jet transition. Therefore, the theoretical description of the straight jet profile attracted significant attention. For describing the flow near the origin of the electrified jet, it is natural to use quasi-1D equations (Yarin, 1993; Yarin, Pourdeyhimi, and Ramakrishna, 2014) and to consider jets as slender bodies with slow changes of the cross-sectional radius r in the longitudinal direction, as illustrated in Sec. IV. This approach was adopted in a number of works for Newtonian fluids (Taylor, 1966; Melcher and Warren, 1971; Kirichenko *et al.*, 1986; Li, Halsey, and Lobkovsky, 1994; Gañán-Calvo, 1997a, Gañán-Calvo, 1997b; Cherney, 1999a, 1999b; Stone, Lister, and Brenner, 1999; Hohman *et al.*, 2001a; Feng, 2002, 2003; Fridrikh *et al.*, 2003; Barrero and Loscertales, 2007). The regime of steady, straight stretching, and particularly the asymptotic behavior at a sufficiently long distance from the spinneret, was also studied for non-Newtonian fluids with rheology described by the Oswald–de Waele power law (Spivak and Dzenis, 1998; Spivak, Dzenis, and Reneker, 2000). Other approaches, incorporating empirical models for the elongational viscosity (Feng, 2002) or the Giesekus constitutive equation (Feng, 2003) in the slender body theory, have also been developed.

In solving the quasi-1D equations, solutions for the jet flow should also be matched with the droplet or meniscus region. For example, this could be achieved by the standard method of matched asymptotic expansions (van Dyke, 1964). In this way, one could match the jet flow with a conical semi-infinite meniscus (Cherney, 1999a, 1999b). A drop shape with a Taylor cone of 49.3° was chosen, which could be rather questionable, as described in Sec. V.A.1. Moreover, complete asymptotic matching was not achieved, as the solutions for the velocity, the potential and the field strength, and the free-surface configuration are all discontinuous (Cherney, 1999a, 1999b). A formal inconsistency of Cherney's analysis was pointed out in a later study (Higuera, 2003). Approximate approaches were largely tested to tackle these difficulties, particularly by extending the quasi-1D jet equations through the entire droplet up to its attachment to the needle (Gañán-Calvo, 1997a, 1997b, 1999; Hohman *et al.*, 2001a; Feng, 2002, 2003). This is quite reasonable as a first approximation; one should keep in mind that the flow in the drop region might have 2D character. Another complication arises from the electric part of the problem, where the image effects (Hohman *et al.*, 2001a) at the solid wall should be taken into account. In fact, the electrical prehistory effects, namely, the image effects responsible for a detailed electrode shape, etc., were found to be important only for a thin boundary layer (Feng, 2002), adjacent to the cross section where the initial conditions are

imposed (i.e., at the needle exit). Accordingly, the quasi-1D equations (Feng, 2002) could be applied when moving the jet origin to a cross section in the droplet (to the distance of the order of the apparent height of the droplet tip). Based on this idea, the flow in the jet region was matched to the one in the droplet (Reznik *et al.*, 2004). The electric current-voltage characteristic $I = I(\Delta\Phi_0)$ was predicted in this way, as well as the flow rate Q in electrospun viscous jets. The predicted $I(\Delta\Phi_0)$ dependence is nonlinear due to the convective mechanism of charge redistribution superimposed on the conductive (Ohmic) one. Several other 2D calculations of the transition zone between a droplet and the electrically pulled Newtonian jet have been published (Hayati, 1992; Reneker *et al.*, 2000; Higuera, 2003; Yan, Farouk, and Ko, 2003; Han, Yarin, and Reneker, 2008; Yarin, Pourdeyhimi, and Ramakrishna, 2014), studying the straight part of electrified, viscoelastic jets, and highlighting large elastic stresses and thus elongational viscosity, which is an additional stabilizing factor disfavoring the early onset of bending instabilities, as well as suppressing the capillary instability.

3. Electrohydrodynamic behavior

Models highlighting EHD effects in jets benefited from studies in the fundamental physics of uncharged, fluid cylindrical threads moving in air or other fluids (Tomotika, 1936; Kase and Matsuo, 1965; Matovich and Pearson, 1969; Khakhar and Ottino, 1987). Results obtained in these contexts were supplemented by elements of electrohydrodynamics to analyze charged fluids stressed by electric fields (Saville, 1970, 1971a, 1971b). Both axisymmetric (Bassett, 1894) and nonaxisymmetric (Saville, 1971b) modes were predicted for charged viscous cylindrical threads, and viscous effects were found to damp axisymmetric deformations (responsible for the capillary instability) more than nonaxisymmetric ones (Saville, 1971b). In particular, following experimental insights (Magarvey and Outhouse, 1962; Huebner, 1969, 1970), Saville theoretically observed that an increasing amount of electrical charge carried by a liquid jet causes the amplification of nonaxisymmetric disturbances, today commonly known as bending and whipping instabilities, which imprint a sinusoidal shape on the cylindrical thread (Saville, 1971b). Later several groups investigated the stability of nonaxisymmetric modes in electrified cylindrical jets under an external electric field (Reneker *et al.*, 2000; Hohman *et al.*, 2001a, 2001b; Shin *et al.*, 2001; Yarin, Koombhongse, and Reneker, 2001a; Fridrikh *et al.*, 2003; Li *et al.*, 2013). Extending the overview to the dripping regime, Collins, Harris, and Basaran (2007) numerically probed the breakup of electrified jets in the range of slightly viscous and moderate viscous jets, corresponding to capillary number values $\sim 10^{-3}$ and 10^{-1}. Further, López-Herrera, Gañán-Calvo, and Perez-Saborid (1999) and López-Herrera and Gañán-Calvo (1999) investigated the capillary jet breakup of conducting liquids with different viscosities under external electrostatic fields. In the framework of electrospinning, starting from a previous 1D approximation of the Navier-Stokes equation (Entov and Yarin, 1984b; Eggers and Dupont, 1994; Eggers, 1997), Hohman *et al.* (2001a, 2001b) extended the Saville model to account for the presence of surface charge on the jet with a finite conductivity
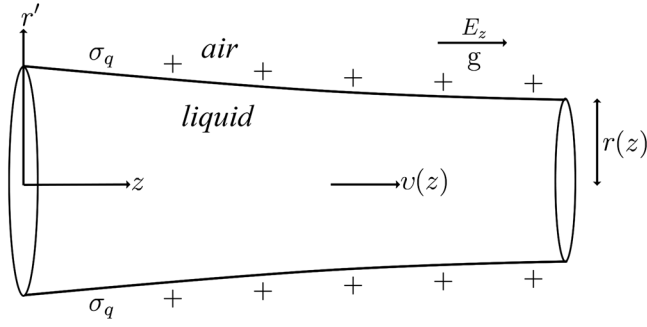
FIG. 14. Scheme of the continuous slender body representing the jet in Eqs. (5)–(8). The coordinates (z, r') used in Eqs. (5)–(8) are reported alongside the main parameters employed in the model.

between two plane metallic electrodes, leading to an E_z axial component of the electric field. The jet was schematized as shown in Fig. 14, namely, as a continuous slender body with surface charge density σ_q and the fluid assumed to have permittivity ε, density ρ, and kinematic viscosity ν. The dynamics was described in a gravitation field with acceleration g directed along the jet axis, and in a surrounding medium with dielectric constant ε_{air} (free space outside the jet). The following quasi-1D equations account for the mass conservation (the continuity equation), the charge conservation, the momentum balance (following from the Navier-Stokes equation) of a fluid element along a cylindrical jet of radius r and electrostatic potential Φ between the parallel electrodes, respectively (Hohman *et al.*, 2001a):

$$\frac{\partial}{\partial t}(\pi r^2) + \frac{\partial}{\partial z}(\pi r^2 v) = 0, \tag{5}$$

$$\frac{\partial}{\partial t}(2\pi r \sigma_q) + \frac{\partial}{\partial z}(\pi r^2 \sigma_e E_z + 2\pi r \sigma_q v) = 0, \tag{6}$$

$$\frac{\partial v}{\partial t} + \frac{\partial}{\partial z}\left(\frac{v^2}{2}\right) = -\frac{1}{\rho}\frac{\partial p}{\partial z} + g + \frac{2\sigma_e E_z}{\rho r} + \frac{3\nu}{r^2}\frac{\partial}{\partial z}\left(r^2 \frac{\partial v}{\partial z}\right), \tag{7}$$

$$\Phi(z, r') = \Phi_\infty - \left(\frac{1}{\varepsilon}\sigma_q r - \frac{\varepsilon - \varepsilon_{air}}{2\varepsilon_{air}}\frac{d(E_z r^2)}{dz}\right)\ln\frac{r'}{L}. \tag{8}$$

Here p is the internal pressure in the fluid, estimated by Hohman and co-workers as $p = k\alpha - E^2[(\varepsilon - \varepsilon_{air})/2] - \sigma_q^2[1/(2\varepsilon_{air})]$, with k the local curvature and α the surface tension since the pressure term also includes the Laplace contribution due to the surface tension. v is the axial velocity of the jet to the leading-order constant in the jet cross section. In Eq. (8), L indicates the characteristic axial length scale (determined by the shape of a jet as it thins away from the nozzle), whereas Φ_∞ indicates the electrostatic potential at a large radial distance r'. Asymptotic descriptions of the EHD equations were developed for a quantitative comparison with experiments (Hohman *et al.*, 2001a). It was also noted that the Laplace contribution is itself depending on the jet radius, which could be explicitly taken into account, i.e.,

$k\alpha = \alpha/[1 + (\partial r/\partial z)^2]^{1/2}\{(1/r) - (\partial^2 r/\partial z^2)/[1 + (\partial r/\partial z)^2]\}$, where $r(z, t)$ is the radius at the jet position z at time t (Lee, 1974). The electric current I carried by the jet is given by the sum of a bulk Ohmic component and a surface advection component associated with the surface charge density $I = \pi r^2 \sigma_e E_z + 2\pi r \sigma_q v$. Finally, the solvent evaporation and the jet viscoelasticity are neglected.

Using the linear stability analysis, three modes of the instability can be identified (Reneker *et al.*, 2000; Hohman *et al.*, 2001a, 2001b; Shin *et al.*, 2001; Yarin, Koombhongse, and Reneker, 2001a; Yarin, Kataphinan, and Reneker, 2005): (i) an axisymmetric instability that extends the classical phenomenon of the Rayleigh capillary instability (Rayleigh, 1878) to the case of electrified jets; (ii) another instability mode that is also axisymmetric, named conducting since it is found only for fluids with finite, nonzero conductivity; (iii) a nonaxisymmetric, bending or whipping instability, that is, also electrically driven, in which the jet axis bends but the cross section stays circular. Branching instability is also found, which is the electrically driven instability developing on the background of the bending instability, but with the jet cross section acquiring multilobe shapes rather than staying circular.

In other works, the boundary conditions at the nozzle were analyzed in detail and non-Newtonian rheology was considered (Feng, 2002, 2003), which is important for polymer solutions. Furthermore, the effects of the electrical conductivity and viscoelasticity on the jet profile during the initial stage of electrospinning have been examined in depth (Carroll and Joo, 2006). Viscoelasticity could be incorporated in the EHD equations by modeling the fluid rheology with the Oldroyd-B constitutive equation (Prilutski *et al.*, 1983; Mackay and Boger, 1987), or the upper-convected Maxwell (UCM) model (Reneker *et al.*, 2000; Yarin, Koombhongse, and Reneker, 2001a; Yarin, Pourdeyhimi, and Ramakrishna, 2014). Increasing the conductivity (which can be attempted, for instance, by adding a salt to the solution) or the fluid viscoelasticity resulted in delayed and more rapid jet thinning. Indeed, how fast the jet thins is complex and depends on other parameters, such as the applied potential difference, namely, the electric field in the region of space where electrospinning takes place (Carroll and Joo, 2006). Axisymmetric instabilities, and particularly axisymmetric conducting modes, were reanalyzed for viscoelastic polymer solutions (Carroll and Joo, 2008, 2009). The EHD equations for viscoelastic fluids were also studied by using the PDE module in the COMSOL MULTIPHYSICS software, which has also been applied to analyze the electric field in a multijet configuration (Angammana and Jayaram, 2011a, 2011c).

4. Electrically driven bending instability

Significant stretching and thinning of electrically driven polymer jets diminishes bending stiffness (which, as anticipated in Sec. V.A.2, is proportional to r^4, where r is the local cross-sectional radius of the jet). Then, at some distance from the needle, nonaxisymmetric perturbations begin to grow and the electrically driven bending instability sets in (Reneker *et al.*, 2000). A typical bending path is shown in Fig. 4(b). As explained in Sec. II, in this regime the characteristic hydrodynamic time is significantly shorter than the charge

relaxation time. Under such conditions the same liquid, which behaved as a perfect conductor in the Taylor cone, behaves as a perfect dielectric in the jet. Then the conduction component of the electric current along the jet can be neglected, and the charge transport is attributed entirely to the jet flow; i.e., the charge is frozen in the liquid, leading to a purely advection current.

The reason for the bending instability observed in experiments may be understood as follows (Reneker *et al.*, 2000). In the frame of reference moving with a rectilinear electrified jet, the electrical charges can be regarded as static and mutually interacting according to Coulomb's law (without the external field). Such systems are known to be unstable according to Earnshaw's theorem (Jeans, 1958). Indeed, an off-axis misalignment rapidly triggers bending instability driven by electrostatics, with an exponentially increasing amplitude. To illustrate this mechanism, one can consider three pointlike charges, each with a value of q and originally located on a straight line at A, B, and C, along the longitudinal axis of the jet, as shown in Fig. 15. Two Coulomb forces with magnitudes $F = q^2/\ell_1^2$ push against charge B from opposite directions. Here ℓ_1 indicates the distance between two charges and the Coulomb constant is left out because $k_C = 1$ in cgs units (Sommerfeld, 1952). If a perturbation causes the charge B to move off the line by a distance δ to point B', a net force $F_1 = 2F\cos\theta = (2q^2/d_C^3)\delta$ acts on that charge, where θ is the angle between the perturbed AB' and CB' directions and the perpendicular to the jet axis. This net force is acting in the direction perpendicular to the original jet line and leads the charge initially at point B to move farther in the direction of the perturbation, namely, away from the line between the two fixed charges A and C. The growth of the small bending perturbation in the linear approximation is then given by

$$m\frac{d^2\delta}{dt^2} = \frac{2q^2}{\ell_1^3}\delta, \qquad (9)$$

where m is the mass of the particle and ℓ_1 is shown in Fig. 15. The growing solution of Eq. (9), $\delta = \delta_0 \exp[(2q^2/m\ell_1^3)^{1/2}t]$,
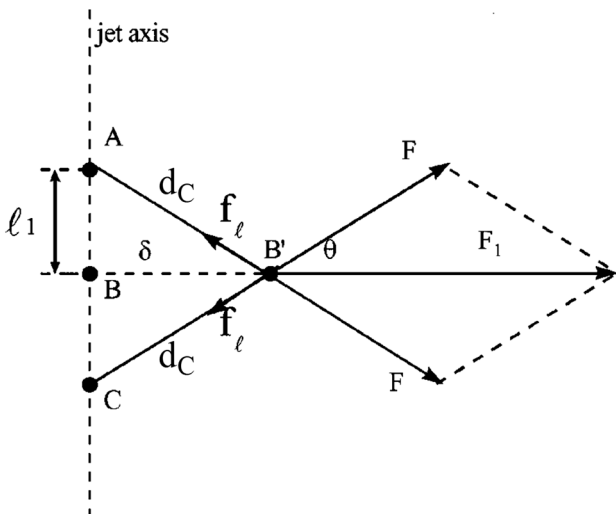

FIG. 15. Sketch of the Earnshaw instability, leading to bending of the electrified jets. Adapted from Reneker *et al.*, 2000.

highlights that small bending perturbations increase exponentially, sustained by the corresponding decrease of the electrostatic potential energy. If the charges A, B, and C are attached to a liquid jet, other forces that are associated with the liquid tend to counteract the electrically driven instability. For thin liquid jets, the influence of the shearing force related to bending stiffness $\sim r^4$ can be neglected compared with the stabilizing effect of the longitudinal forces f_ℓ, which are of the order of r^2 (Yarin, 1993). In fact, the longitudinal force at the cross section at the onset of the bending instability is determined by the end of the straight section of the jet. The forces f_ℓ are directed along $B'C$ or $B'A$ according to the scheme in Fig. 15 and are the opposite of the local Coulomb force. If such Coulomb force F is larger than the viscoelastic resistance, the bending perturbation continues to increase, but at a rate diminished by f_ℓ. To describe the viscoelastic response, the Maxwell model (Maxwell, 1867; Ferry, 1980; Morozov and Spagnolie, 2015) assumes that the dumbbell defined by each pair of particles supports a stress σ that changes as that of system with a spring (Hooke's law) and a damper having a relaxation time $\theta = \mu/G$, where G is the elastic modulus and μ is the viscosity. In addition, the surface tension also counteracts the bending instability because bending always leads to an increase in the jet surface area. Hence, surface tension resisting the reaching of significant curvature tends to limit the smallest possible perturbation wavelengths, although surface tension effects might be negligibly small compared to the electric and viscoelastic forces in electrospinning.

The linear stability theory of bending in an electrified polymer solution jets yielded the following characteristic equation for the growth rate γ of such perturbations (Yarin, Koombhongse, and Reneker, 2001a):

$$\gamma^2 + \frac{3}{4}\frac{\mu\chi^4}{\rho r_0^2}\gamma + \left(\frac{\alpha}{\rho r_0^3} - \frac{e_0^2 \ln(L/r_0)}{\pi\rho r_0^4}\right)\chi^2 = 0, \qquad (10)$$

where $\chi = 2\pi r_0/\ell_P$ is the dimensionless wave number (ℓ_P is the wavelength of the perturbation), μ is the dynamic viscosity, r_0 and e_0 are the unperturbed values of the cross-sectional jet radius and of the electric charge per unit jet length, respectively, and L is the cutoff jet length. Equation (10) accounts for the shearing force and moment of forces in the jet cross section, namely, for the bending stiffness. It also shows that the destabilizing electric force overcomes the stabilizing effect of the surface tension (the only stabilizing effect here) if $e_0^2 \ln(L/r_0) > \alpha\pi r_0$. If this condition is not fulfilled, the capillary and bending instabilities are concurrent, as indeed observed in experiments with viscous organic oils (Malkawi, Yarin, and Mashayek, 2010) and shown in Fig. 16. More details about these aspects are reviewed in Sec. V.B.2.

The nonlinear theory of the bending instability of viscoelastic polymeric jets in electrospinning was developed by Reneker *et al.* (2000), Yarin, Koombhongse, and Reneker (2001a), and Yarin, Pourdeyhimi, and Ramakrishna (2014). As previously explained, for thin jets the effect of the shearing force, as well as the bending stiffness, can be neglected (Yarin, 1993). Then, in this momentless approximation, a curvilinear
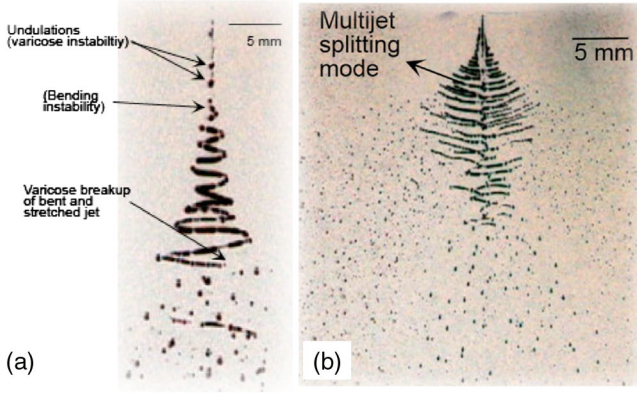
FIG. 16. Breakup of electrified corn oil jets, generated with a fixed flow rate of 30 ml/ min (corresponding to a velocity of 10 m/s at the injection orifice) and applied voltages (a) −8 kV and (b) −10 kV applied between the needle orifice and the nozzle of an atomizer. Adapted from Malkawi, Yarin, and Mashayek, 2010.

FIG. 17. Sketch of an element of a curved jet of length $\Delta\xi$ and the associated internal frame of reference, with normal $\mathbf{n}$, binormal $\mathbf{b}$, and tangent vector $\boldsymbol{\tau}$, used in Eq. (11b).

parameter s can be introduced. It might be considered a Lagrangian coordinate reckoned along the jet, and it takes the values $s = 0$ and ℓ_0 at the nozzle and at the free jet termination, respectively. Here ℓ_0 is the initial arc length of the jet, and any value of $s \in (0, \ell_0)$ represents a jet element in an univocal way (the s value is frozen in the jet elements). Thus, the quasi-1D continuity equation and the momentum balance equation take the form

$$\lambda f = \lambda_0 f_0, \tag{11a}$$

$$\rho\lambda_0 f_0 \frac{\partial \boldsymbol{v}}{\partial t} = \boldsymbol{\tau}\frac{\partial P}{\partial s} + \lambda|k|P\mathbf{n} - \rho g\lambda_0 f_0\mathbf{k}$$
$$+ \lambda|k|\left[\alpha\pi r - e_L^2 \ln\left(\frac{L}{r}\right)\right]\mathbf{n} - \lambda e_L \frac{\Delta\Phi}{h}\mathbf{k}. \tag{11b}$$

Equation (11a) is the continuity equation, where λ is the geometrical stretching ratio, i.e., $\lambda = |\partial\xi/\partial s|$, with $\xi(s,t) \in [0,\ell]$ the arc length reckoned along the bent jet axis and $f(s,t) = \pi r^2$ the cross-sectional area. The cross section can be assumed to stay circular even in bending jets, which is a plausible approximation (Yarin, 1993). The fluid is incompressible (fluid volume preserved). The subscript 0 denotes the parameter values at time $t = 0$, namely, the unperturbed values. Equation (11b) expresses the momentum balance, with $\boldsymbol{v}(s,t)$ the liquid velocity, $P(s,t) = (\lambda_0 f_0/\lambda)\sigma(s,t)$ the longitudinal force in the jet cross section (of viscoelastic origin in the case of electrospun polymeric jets, or solution-blown jets), $g\mathbf{k}$ the gravity acceleration (the unperturbed jet is, in general, implied to be in the vertical direction), t the time, e_L the electric charge per unit length, and $\mathbf{n}$ the local principal normal unit vector of the jet axis. $\Delta\Phi_0/h$ is the external electric field intensity (the external field is assumed to be parallel to the unit vector $\mathbf{k}$, with $\Delta\Phi_0$ and h the values of the electrical potential bias and the distance between the jet origin and a collector, respectively). The overall configuration is displayed in Fig. 17. On the right-hand side of the momentum equation (11b), the 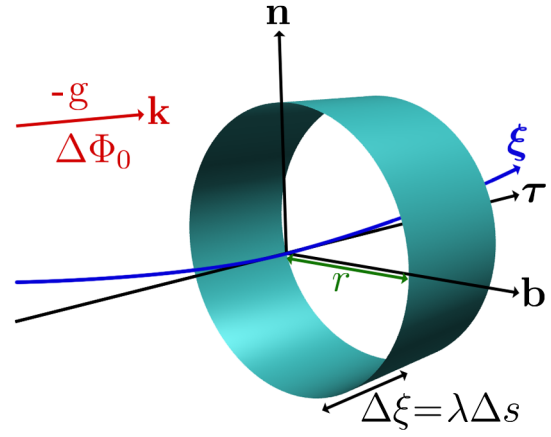following forces are accounted for: the longitudinal internal force of rheological origin acting on the jet (the first two terms), gravity (the third term), the bending electric force versus the stabilizing effect of the surface tension (the fourth term), and the force due to the external electric field (the fifth term).

B. Lagrangian models

This section reviews the general features of the Lagrangian formulation for modeling of the electrospinning process. The advantages of the Lagrangian formulation are summarized at first, contextualizing some aspects anticipated in Secs. IV and V.A through some electrospinning models based on it. Then several application scenarios are reviewed, with specific attention paid to physical insight obtained in the theoretical framework.

1. Why the Lagrangian formulation?

It is possible to write the momentum balance, quasi 1D in Eq. (11b), in the 3D framework, allowing for the simulation of the full electrospinning process by numerical solvers. At a first inspection of the force terms, it is easy to realize that although the external electric field provides a global force the other force terms driving the jet dynamics are mostly local [Eq. (11b)]. The locality would seem to suggest numerically solving the momentum balance equation at specific positions in space as a function of time, i.e., with an Eulerian frame of reference. Nonetheless, the presence of constitutive relations between stress and strain, describing the deformation of the jet, makes the Eulerian description less than optimal for the numerical solution of actual models. Indeed, jets flowing at high speed undergo stress-induced deformations that depend on rheology. As a consequence, a memory of such deformations is locally stored on the traveling jet as a "fingerprint." If viscous forces do not dissipate the local signatures, they are transported by the flow field. The electrospinning process presents exactly these features, with a deformable interface moving rapidly over the space toward the collector counterelectrode.

The strength of the Lagrangian formulation is the retention of fluid element identity that is stored in memory with a set of

observables (e.g., position, velocity, etc.) describing its state at a given instant. Instead, the Eulerian description of the jet over a grid of fixed points would suffer memory loss because the jet elements are not tracked over the fluid dynamics.

Summarizing, the choice of the optimal description is usually dependent on how far a piece of local information is transported by the dynamics. As a consequence, it is not surprising that the Lagrangian formulation has mostly been adopted in simulations of turbulent flows, where the ratio of inertial forces to viscous forces (the Reynolds number) is of the order of several thousand (Meneveau, Lund, and Cabot, 1996; Bennett, 2006). Moreover, a number of Lagrangian methods have been introduced to treat several problems of fluid dynamics where a local state of a system is moved over the space. Among them, we recall molecular dynamics, dissipative particle dynamics, and smoothed particle hydrodynamics (Gui-rong, 2003; Liu and Liu, 2016), to name a few.

In 1994, the first notable example of a Lagrangian particle method for the simulation of electrically driven fluid dynamics was presented in the context of electrospray modeling (Gañán-Calvo *et al.*, 1994). This effort highlighted the efficiency of the Lagrangian formulation in modeling highly dispersed charged droplets emitted from an electrified conical meniscus toward a collector. In this description, each particle represented a charged droplet with appropriate mass and charge.

An electrospun jet is a more complex system that, however, lies in a 1D space over its arc length $\ell_{\rm jet}$, namely, the length of the curve drawn by the axis of the jet. As mentioned in Sec. IV, in 2000, the Reneker and Yarin groups introduced the first Lagrangian model for electrospinning (Reneker *et al.*, 2000), where the jet was treated as a 1D chain of particles, connected pair by pair through viscoelastic springs extending over the jet curve. In this framework, each particle represents a volumetric portion of the jet with given mass and charge. Each pair of two consecutive connected particles along the chain acts as a viscoelastic dumbbell, with the distance between the two extreme points modeling the stretch ratio of the jet (as well as the surface to volume ratio).

2. Quasi-one-dimensional Lagrangian models

An electrospun fluid undergoes an increase in the tensile stress as it passes from the Taylor cone to the straight jetting region through a transient zone. The experimental data show that the rate of strain $\dot{\varepsilon}$ is of the order of 100–1000 s^{-1} in this region, which provides an extremely high longitudinal viscoelastic stress (Han, Yarin, and Reneker, 2008). This widely affects both the shape and the charge distribution of the jet already at the initial stage of the dynamics; hence, developing a reliable modeling for this zone is critically important. The charge distribution formed here has a substantial effect on the further evolution of the jet, considering that the bending instabilities are related mainly to the intrajet repulsive Coulomb force. Thus, the Lagrangian discretization of the quasi-1D set of Eqs. (11a) and (11b) reported in Sec. V.A.4 has been employed in multiple theoretical investigations (Reneker *et al.*, 2000; Kowalewski, Błoński, and Barral, 2005; Carroll and Joo, 2011; Rafiei *et al.*, 2013; Lauricella, Pontrelli, Coluzza *et al.*, 2015a). In a 1D framework, given the

z axis and approximating the stretching ratio $\lambda = |\partial\xi/\partial s| \approx \ell_{\rm jet}(t)/\ell_0$, the position of a jet element under stretching is traced by the relation $z(t) = \lambda(t)\,s$ in an univocal way. Thus, a discrete set of position values $\{z_i\}_{i=1,\ldots,n}$ with $z_i = \lambda\,s_i$ can be inserted into Eq. (11b), obtaining a Lagrangian discretization of the continuous object.

The simplest model exploits the jet discretization in two particlelike beads u and d with the same mass m and charge q describing a charged drop (Fig. 18). The upper bead u is held fixed to the nozzle at $z_u = 0$, while the lower one d is free to move and initially placed at distance $z_d = \ell_0$. Neglecting the gravitational force, the quasi-1D momentum balance equation along the unit tangent jet vector $\boldsymbol{\tau}$ for the free d bead reads

$$m\frac{\partial v}{\partial t} = -\pi r^2\sigma + q\frac{\Delta\Phi_0}{h} + \frac{q^2}{\ell^2}, \tag{12}$$

where $\ell = z_d - z_u$ is the mutual distance between the two beads equal to the entire jet length, $\ell = \ell_{\rm jet}$, by construction, r is the cross-sectional radius, and $\Delta\Phi_0$ is, as usual, the difference in electric potential between the nozzle and the
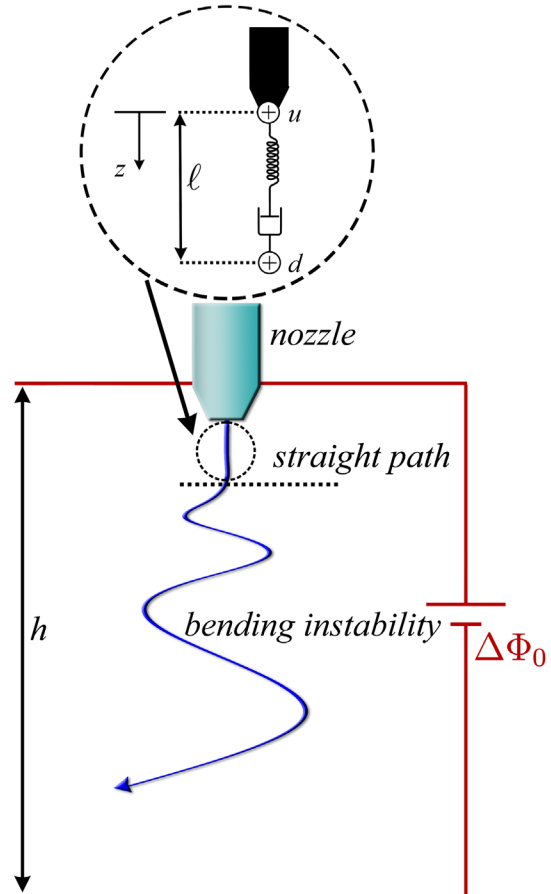
FIG. 18. Schematic drawing of the electrospinning process (not in scale), highlighting the two particle-like beads used in the quasi-1D model. The two beads are connected by a linear, viscoelastic dumbbell. h, distance between the collector plate and the nozzle; $\Delta\Phi_0$, applied voltage difference between the two elements; z, reference axis coordinate, whose origin is fixed at the injection point. Adapted from Lauricella, Pontrelli, Coluzza *et al.*, 2015b.

collector placed at distance h. Here the internal viscoelastic force $\pi r^2 \sigma$ is modeled by a constitutive equation. The UCM model is a plausible rheological representation for semidilute and concentrated polymeric liquids under uniaxial, strong elongational flows (Chang and Lodge, 1972; Stelter *et al.*, 2000; Yarin, Pourdeyhimi, and Ramakrishna, 2014). Denoting G as the elastic modulus and μ as the viscosity of the fluid, the simplest UCM in its linear version, namely, the Maxwell model (Maxwell, 1867; Ferry, 1980; Morozov and Spagnolie, 2015), reads

$$\frac{\partial \sigma}{\partial t} = G\dot{\varepsilon} - \frac{G}{\mu}\sigma, \qquad (13)$$

where $\dot{\varepsilon} = \partial \ell / \ell \partial t$ is the strain rate. Applying the condition of volume conservation $\pi r_0^2 \ell_0 = \pi r^2 \ell$ and the kinematic relation

$$\frac{\partial z}{\partial t} = \frac{\partial \ell}{\partial t} = v, \qquad (14)$$

this simple model allows one to probe the initial dynamics of the electrified jet. To adopt a dimensionless form of the EOM, the dimensionless quantities reported in Table II can be conveniently used so that, for instance, the dimensionless form of Eq. (12) reads

$$\frac{\partial \bar{v}}{\partial \bar{t}} = F_{ve}\frac{\bar{\sigma}}{\bar{\ell}} + V + \frac{Q_e^2}{\bar{\ell}^2}. \qquad (15)$$

Using Eq. (15), Reneker *et al.* (2000) inspected the time evolution of the viscoelastic force term for the typical values of experimental relevance, $Q_e = 12$, $V = 2$, and $F_{ve} = 12$. As shown in Fig. 19, the external electric field acts along all of the dynamics, stretching the initial jet with magnitude proportional to the distributed charge (Lauricella, Pontrelli, Coluzza *et al.*, 2015b). While the dynamics proceeds, the viscoelastic force increases up to a peak value within the dimensionless time $\bar{t} \leq 1$, remaining the dominant force term up to $\bar{t} \sim 2$. As the stress reaches its peak value [Fig. 19(a)], lasting about up to $\bar{t} \sim 1$, the velocity comes to nearly constant value, then reaching a linear regime in the jet length evolution in time, $\bar{\ell} \propto \bar{t}$ [Fig. 19(b)]. After this point, the viscoelastic force starts

TABLE II. Definitions of the characteristic scales, dimensionless derived variables, and groups employed in Sec. V.B.2.

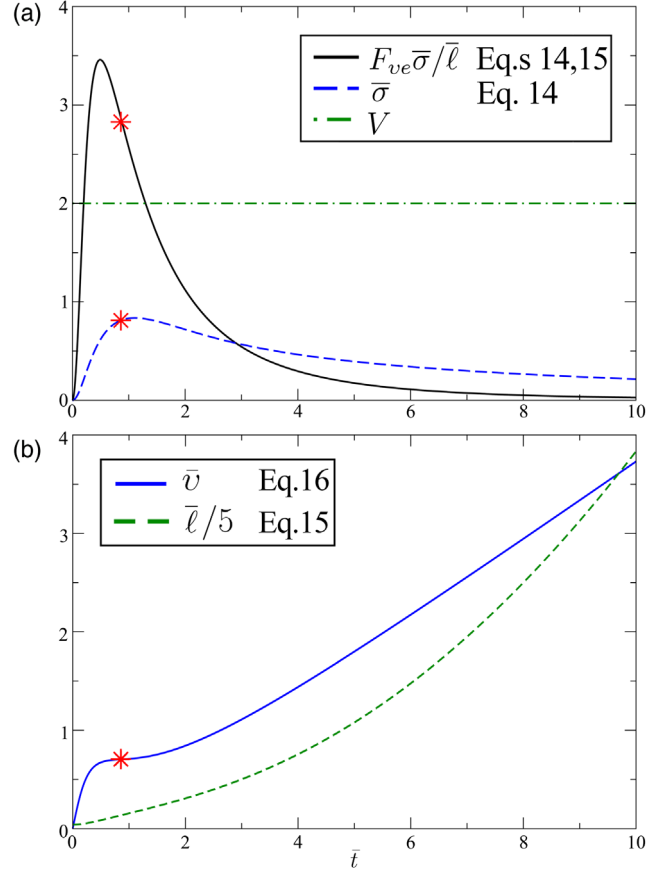| Characteristic scales	
$L_0 = \ell_{\text{step}}\sqrt{\pi a_0^2 \rho_V^2 / G}$	$t_0 = \mu/G$
$\sigma_0 = G$	
Dimensionless derived variables	
$\bar{\ell}_i = \ell_i/L_0$	$\bar{R}_{ij} = R_{ij}/L_0$
$\bar{k} = kL_0$	
Dimensionless groups	
$V_i = q_i V_0 \mu^2 / m_i h L_0 G^2$	$Q_{e,ij} = q_i q_j \mu^2 / L_0^3 m_i G^2$
$F_{ve,i} = \pi a_0^2 \mu^2 / m_i L_0 G$	$A_i = \alpha \pi a_0^2 \mu^2 / m_i L_0^2 G^2$
$F_g = g\mu^2 / L_0 G^2$	$K_s = \omega(\mu/G)$
$H = h/L_0$	$L_{\text{step}} = \ell_{\text{step}}/L_0$

FIG. 19. (a) The longitudinal force $F_{ve}\bar{\sigma}/\bar{\ell}$ (solid line) and the longitudinal stress $\bar{\sigma}$ (dashed line) in the rectilinear part of the jet for the case $Q_e = 12$, $V = 2$, $F_{ve} = 12$. (b) Time evolution of the velocity $\bar{v}$ (solid line) and the length $\bar{\ell}$ (dashed line), here rescaled by a factor of $1/5$ (dotted line) to have both quantities conveniently plotted along the same vertical axis. Two stages of the elongation process are observed. The first stage comes to a quasistationary point (asterisk in both panels). At the second stage, the velocity comes to a near linearly increasing regime. Adapted from Lauricella, Pontrelli, Coluzza *et al.*, 2015b.

to decay due to viscoelastic relaxation with relaxation time θ and is no longer able of sustain the expanding "pressure" of the electrostatic interactions (repulsive Coulomb and external potential forces). Thus, the linear regime cannot last long and the jet expansion is described by a regime with a jet length evolving in time as $\bar{\ell} \propto \bar{t}^2$. In this portrait of regimes, the quasistraight path is experimentally observed as the initial dynamics of the process (the linear regime). Here the viscoelastic force not only provides stiffness necessary to maintain the jet straight but also plays the dominant role in stabilization. Given the importance of the viscoelastic term, the model was extended to account for different types of non-Newtonian behavior in the initial jet dynamics (Pontrelli *et al.*, 2014), particularly by adding a Herschel-Bulkley stress term in Eq. (13) and including the yield stress for the description of Bingham fluids (Bird, Armstrong, and Hassager, 1987). In this way, Eq. (13) takes the form $\dot{\sigma} = (G/\mu)[\sigma - \sigma_Y + K(\dot{\ell}/\ell)^n]$ so that the effective viscosity is $\mu = K|\dot{\ell}/\ell|^{n-1}$, with K a prefactor having units of $\mathrm{g\,s}^{n-2}\,\mathrm{cm}^{-1}$ and n a power-law

exponent. In particular, whenever the ratio σ_Y/G is set equal to 0.8, a halved value was found in the jet linear extension during the initial stage of electrospinning, due to an increase by nearly 2 times in the value of the longitudinal viscoelastic stress σ (Pontrelli *et al.*, 2014). As a consequence, the jet would soon start to show bending oscillations.

To simulate the electrospinning process in its entire dynamics, one also needs to properly model the fluid injection at the nozzle. Several algorithms addressed this issue (Reneker *et al.*, 2000; Kowalewski, Barral, and Kowalczyk, 2009; Carroll and Joo, 2011; Lauricella, Pontrelli, Coluzza *et al.*, 2015a). Let us consider a simulation starting again with two beads: a single massless point labeled $i = 0$ and fixed at $z_0 = 0$ representing the spinneret nozzle, and a second bead (labeled $i = 1$) modeling a pendant element of fluid of mass m_1 and charge q_1. The second bead is placed at the initial distance $z_1 = \ell_0 = \ell_{\text{step}}$ from the nozzle along the z axis, with initial velocity v_s equal to the bulk fluid velocity in the syringe needle. ℓ_{step} represents the length step used to discretize the jet in a sequence of beads. Once the traveling jet bead reaches the distance $z_1 = 2\ell_{\text{step}}$ away from the nozzle, a new jet bead ($i = 2$) is placed at a distance $z_2 = \ell_{\text{step}}$ from the nozzle with the initial velocity $v_2 = v_s + v_d$, where v_d denotes the dragging velocity computed as $v_d = (v_1 - v_s)/2$. The dragging velocity acts as an additional term accounting for the drag effect of the electrospun jet on the last inserted segment, which preserves the strain rate value at the jet point z_2 before and after the bead insertion. Hence, the procedure is repeated until a chain of n beads representing the jet is obtained (Fig. 20). Note that the injection bead does not alter the curvilinear parameter s, which preserves its domain, $s \in [0, \ell_0]$, but adds an extra element only in the set of values used to discretize the jet path. On the other hand, the added bead represents a new jet parcel of volume $\ell_{\text{step}}\pi r_0^2$, mass m_i, and charge q_i so that the extensive properties of the jet (total volume, mass, and charge) increase after the insertion.

Adding the injection algorithm to Eq. (12), the momentum balance equation along the unit tangent jet vector $\boldsymbol{\tau}$ for the ith bead reads

$$m_i \frac{\partial v_i}{\partial t} = -\pi r_{ui}^2 \sigma_{ui} + \pi r_{di}^2 \sigma_{di} + q_i \frac{\Delta \Phi_0}{h}$$
$$+ q_i \sum_{\substack{j=1,n \\ j \neq i}} \frac{q_j}{|z_i - z_j|^3}(z_i - z_j), \qquad (16)$$

where the Coulomb repulsive force takes into account all interactions with the other $n - 1$ jet segments and the tensile force is computed as the stress difference between the upper and lower dumbbell elements with extremes $(i + 1, i)$ for the ui dumbbell and $(i, i - 1)$ for the di dumbbell, respectively, along the bead chain (Fig. 20). In fact, the finite difference $(-\pi r_{ui}^2 \sigma_{ui} + \pi r_{di}^2 \sigma_{di})$ approximates the derivative of the longitudinal force along the fiber, that is, the term $\partial P/\partial s$ in the continuum description of Eq. (11b).

Results from this quasi-1D model were compared to experimental data (Carroll and Joo, 2011), with some discrepancies found in stable jet profiles, which were
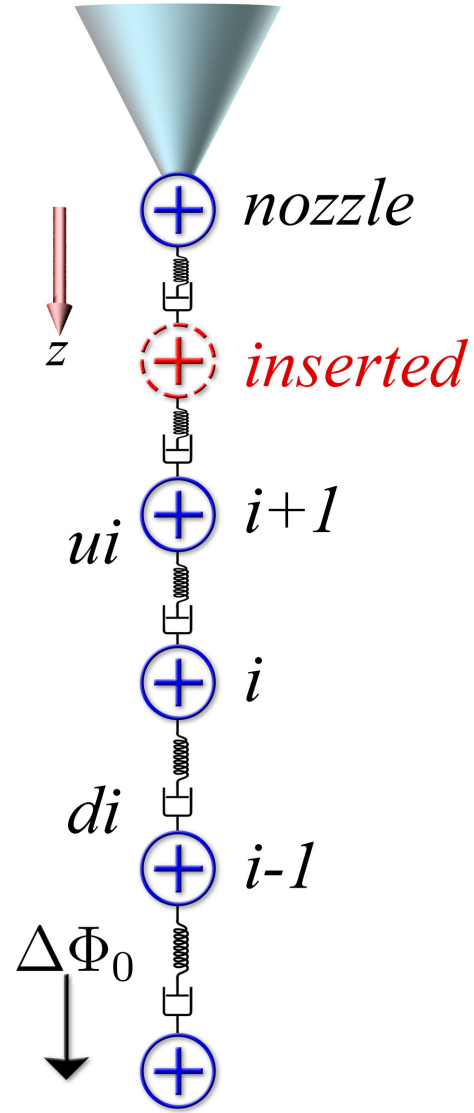

FIG. 20. Diagram of the jet modeled as a chain of 1D discrete elements. Each element representing a jet segment is drawn as a circle with a plus sign denoting its positive charge. The ith element is along the chain between the upper and lower dumbbell elements with extremes $(i + 1, i)$ for the ui dumbbell and $(i, i - 1)$ for the di dumbbell, respectively, and it is stretched under the external electric potential difference $\Delta \Phi_0$. The cone at the top of the figure represents the nozzle.

subsequently recovered by an amended version of the model. First, the polymer fluid was described as an Oldroyd-B fluid, whose rheology is described using two distinct contributions. These include both a σ_p stress term, from the viscoelastic dumbbell term (using the Maxwell model) due to the polymeric component, and $\sigma_s = \mu_s \dot{\gamma}$, from a Newtonian solvent in which the viscoelastic elements are immersed. Consequently, the total tensile stress $\sigma = \sigma_p + \sigma_s$ is computed for each ith bead and inserted into Eq. (16). Second, the liquid jet was considered a leaky dielectric rather than a perfect conductor, thereby including the effect of finite conductivity in the fluid. Thus, the charge q_i in Eq. (16) is replaced by an
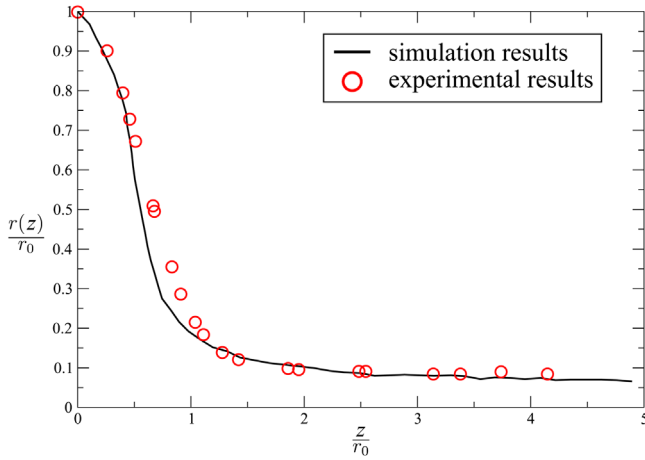
FIG. 21. Radius profile obtained from bead-spring simulations and from experiments for the electrospinning of 4000 ppm polyisobutylene Boger fluid. The parameters used in the simulation are estimated from experiments (Carroll and Joo, 2006): jet initial radius, $r_0 = 0.05$ cm; surface tension, $\alpha = 14.6$ g s^{-2}; elastic modulus, $G = 328$ g cm^{-1} s^{-2}; electrical conductivity, $\sigma_e = 270$ s^{-1}; zero-shear viscosity, $\mu_0 = 1.02$ g cm^{-1} s^{-1}; solvent viscosity ratio, $\mu_s/\mu = 0.471$; and total current carried by the jet, $I_{\text{total}} = 5.4$ StatC s^{-1}. Adapted from Carroll and Joo, 2011.

effective charge $q_{\text{eff},i} = c_{\text{eff},i}\, q_i$, where $c_{\text{eff},i} = 1 - (I_{\text{conduction}}/I_{\text{total}})$ is the charge fraction on the jet surface that actually interacts with the electric field and the other charges. In particular, $c_{\text{eff},i}$ is computed by setting the total current $I_{\text{total}} = I_{\text{convection}} + I_{\text{conduction}}$ as an input parameter and evaluating step by step at each ith bead the quantity $I_{i,\text{conduction}} = \pi r_i^2 \sigma_e \Delta\Phi_0/h$, with σ_e the electrical conductivity. With these amendments, the jet cross-section profiles $r(x)$ obtained by the Lagrangian model were found to be much closer to the experimental data (Carroll and Joo, 2011). This is illustrated in Fig. 21, which compares the jet profiles of polyisobutylene Boger solutions at concentration of 4000 ppm in low molecular weight polybutene solvent. Moreover, a trend of the tensile stress was provided (Carroll and Joo, 2011), consisting of a rapid increase during the initial jet stretching and subsequent decrease due to the stress relaxation, which is in agreement with theoretical findings (Reneker *et al.*, 2000). Thus, the comparison shows that the simplest two-body version of the Lagrangian model was already able to qualitatively catch the stretching process of the quasistraight path in the jet. In a recent variant, the convection current term $I_{i,\text{convection}} = 2\pi r_i^2 v_i \sigma_q$ was included in an extra ordinary differential equation of the charge, which was solved to compute the conduction charge fraction along the time evolution (Divvela and Joo, 2017).

The fluid representation as a 1D chain of beads is valid only if the dynamics lies entirely in the jetting regime. In this respect, the magnitude of the tensile force plays a crucial role. In fact, thin rectilinear jets may endure varicose perturbations under the action of capillary forces, whose magnitude is affected by the surface tension α (Khakhar and Ottino, 1987). In addition to the dimensionless capillary number described in Sec. II, another way to measure the competition between instability growth and the viscoelastic response is to compare

their respective timescales. The viscoelastic response takes place within the relaxation time $\theta = \mu_e/G$, while the timescale of the capillary instability growth is the inverse of the dimensionless instability growth rate ω_c. The fastest-growing capillary instability occurs with dimensionless frequency $\omega_c^{\text{max}} = 1/\sqrt{2}(1 + 3S\sqrt{\text{Ca}/2})^{1/2}$, where $S = 1/(1 + G\theta/\mu_s)$ accounts for non-Newtonian behavior of the jet, with μ_s the zero-shear viscosity of the solvent (Chang, Demekhin, and Kalaidin, 1999). The ratio of the viscoelastic relaxation time and instability growth time leads to another convenient expression of the Deborah number (Sec. II) De $= \theta\omega_c^{\text{max}}/t^*$, given the characteristic time $t^* = r_0^2 S\rho/\mu_e$ (Jian, Fridrikh, and Rutledge, 2006). For the typical case of the polyisobutylene Boger fluid at a concentration of 4000 ppm in polybutene (Carroll and Joo, 2011) taking a jet radius $r_0 = 0.05$ cm, jet velocity $v = 200$ cm s^{-1} (Montinaro *et al.*, 2015), surface tension $\alpha = 14.6$ g s^{-2}, relaxation time $\theta = 3.11 \times 10^{-3}$ s, zero-shear viscosity $\mu_0 = 1.02$ g cm^{-1} s^{-1} with $\mu_s/\mu_0 = 0.471$ (Carroll and Joo, 2006), and extensional viscosity $\mu_e \sim 20\mu_0$ (Ng *et al.*, 1996), one would estimate the dimensionless numbers Ca ~ 280 and De ~ 680, indicating that the capillary instability is arrested by viscoelastic forces at an early stage of perturbation growth. In this framework, the dimensionless critical stress $\bar{\sigma}^*$ in the jet, necessary for a complete suppression of the Rayleigh-Tomotika instability, is also assessed and found to be equal to $\bar{\sigma}^* = r(z^*)/(2r_0\text{Ca})$, where $r(z^*)$ is the cross-sectional radius measured at a distance z^* from the needle, at which the instability is observed to begin (Jian, Fridrikh, and Rutledge, 2006). Taking the ratio $r(z^*)/r_0 = 0.1$, the critical value of the tensile stress is thousands of times smaller than values obtained in simulations (Lauricella, Pontrelli, Coluzza *et al.*, 2015a; Lauricella, Pisignano, and Succi, 2016) $\sigma(z^*) \sim 4000\sigma^*$. Hence, one can conclude that the quasi-1D representation of the polymeric fluid as a chain of beads is fully justified given the stability of the early jetting regime.

3. Three-dimensional Lagrangian models

At a certain point during stretching of the electrified polymeric jets, the destabilizing electric force prevails. As a consequence, the bending instability starts to grow along the jet. Although the slenderness assumption is still valid, a complete description of the spiraling and looping path requires a 3D model of the electrospun jet. Thus, the quasi-1D model can be extended to describe the jet evolution in the 3D framework, keeping, however, the fundamental original assumptions (e.g., isotropic expansion or reduction of the jet cross section, absence of shearing forces at the lateral surface, and dependence of the jet cross section on the longitudinal expansion). To this purpose, one can exploit the usual curvilinear parameter $s \in [0, \ell_0]$ (see Sec. V.A) to describe the jet in the 3D framework (Reneker *et al.*, 2000) by introducing the vector $\mathbf{R}(s)$ of coordinates $x(s), y(s), z(s)$ in Eq. (16) for a discrete set of values $\{s_i\}_{i=1,\dots,n}$. Exploiting the approximated form of the stretching ratio $\lambda(t)$ introduced in Sec. V.B.2, the total arc length of the jet path at time t is $\ell_{\text{jet}}(t) = \lambda(t)\ell_0$. The momentum balance for the ith bead provides

$$m_i \frac{\partial \boldsymbol{v}_i}{\partial t} = -\pi r_{ui}^2 \sigma_{ui} \boldsymbol{\tau}_{ui} + \pi r_{di}^2 \sigma_{di} \boldsymbol{\tau}_{di} + + k\pi \left(\frac{r_{ui} + r_{di}}{2} \right)^2 \alpha \mathbf{n}_i$$

$$+ q_i \frac{\Delta \Phi_0}{h} \mathbf{k} + q_i \sum_{\substack{j=1,n \\ j \neq i}} \frac{q_j}{|\mathbf{R}_i - \mathbf{R}_j|^2} \mathbf{u}_{ij} + m_i g \mathbf{k}, \quad (17)$$

where the subscripts *ui* and *di* denote, as in Sec. V.B.2, the upper and lower dumbbell elements in the bead chain, $\boldsymbol{\tau}_{ui} = (\mathbf{R}_i - \mathbf{R}_{i+1})/|\mathbf{R}_i - \mathbf{R}_{i+1}|$ and $\boldsymbol{\tau}_{di} = (\mathbf{R}_{i-1} - \mathbf{R}_i)/|\mathbf{R}_{i-1} - \mathbf{R}_i|$ are the unit tangent vector of the upper and lower dumbbells, respectively, $\mathbf{u}_{ij}$ is the unit vector pointing the *i*th bead from the *j*th bead, and $\mathbf{n}_i$ is the principal unit normal vector pointing to the center of the local curvature from the *i*th bead. Here $\mathbf{n}_i$ is multiplying the force term associated with surface tension, i.e., $k\alpha\pi[(r_{ui} + r_{di})/2]^2$, which acts to restore the rectilinear shape of the bent portion of the jet with curvature k. For each *i*th bead, the set of EOM is completed with three kinematic relations (in vector notation $\partial \mathbf{R}_i / \partial t = \boldsymbol{v}_i$) and two constitutive equations of the type reported, for instance, in Eq. (13) for the independent variables σ_{ui} and σ_{di} and schematized in Fig. 20, obtaining a total of eight ordinary differential equations. Finally, the model exploits the injection bead strategy (Sec. V.B.2), with the discretization step length ℓ_{step} as an input parameter, and it is accompanied by a specific set of two EOMs of the nozzle coordinates describing possible mechanical perturbations at the spinneret. In particular, the spinneret nozzle is represented by a single massless point (labeled 0) of charge q_0 fixed at $z_0 = 0$. The charge q_0 is taken equal to the mean charge value of the jet beads and can be interpreted as a small portion of jet, which is glued at the nozzle. The set of EOMs describing the evolution in time of the nozzle reads $\partial x_0(t)/\partial t = \omega y_0(t)$ and $\partial y_0(t)/\partial t = -\omega x_0(t)$, where the initial position at time $t = 0$ is defined by an input phase φ so that $x_0 = A \sin(\varphi)$ and $y_0 = A \cos(\varphi)$, with ω and A the frequency and amplitude of the perturbation, respectively. Alternatively, the nozzle perturbation can be modeled by adding a simple random displacement in the position of the inserted bead (labeled 1) in the injection step so that $x_1 = x_1 + A_{\text{rand}} \sin \varphi_{\text{rand}}$ and $y_1 = y_1 + A_{\text{rand}} \cos \varphi_{\text{rand}}$, with A_{rand} and φ_{rand} the random amplitude and phase, respectively (Kowalewski, Błoński, and Barral, 2005).

The dimensionless form of the EOM, using the quantities reported in Table II, is

$$\frac{\partial \bar{\boldsymbol{v}}_i}{\partial \bar{t}} = L_{\text{step}} \left(-F_{ve,ui} \frac{\bar{\sigma}_{ui}}{\bar{\ell}_{ui}} \boldsymbol{\tau}_{ui} + F_{ve,ui} \frac{\bar{\sigma}_{di}}{\bar{\ell}_{di}} \boldsymbol{\tau}_{di} \right)$$

$$+ L_{\text{step}} \frac{\bar{k}}{4} A_i \left(\frac{1}{\sqrt{\bar{\ell}_{ui}}} + \frac{1}{\sqrt{\bar{\ell}_{di}}} \right)^2 \mathbf{n}_i + V_i \mathbf{k}$$

$$+ \sum_{\substack{j=1,n \\ j \neq i}}^{n} \frac{Q_{e,ij}}{\bar{\ell}_{ij}^2} \mathbf{u}_{ij} + F_g \mathbf{k}, \quad (18)$$

where $\bar{\ell}_{ui} = |\mathbf{R}_i - \mathbf{R}_{i+1}|/L_0$ and $\bar{\ell}_{di} = |\mathbf{R}_{i-1} - \mathbf{R}_i|/L_0$ denote the dimensionless distance between the upper and lower beads with respect to the *i*th bead, respectively, while $\bar{\ell}_{ij} = |\mathbf{R}_i - \mathbf{R}_j|/L_0$.
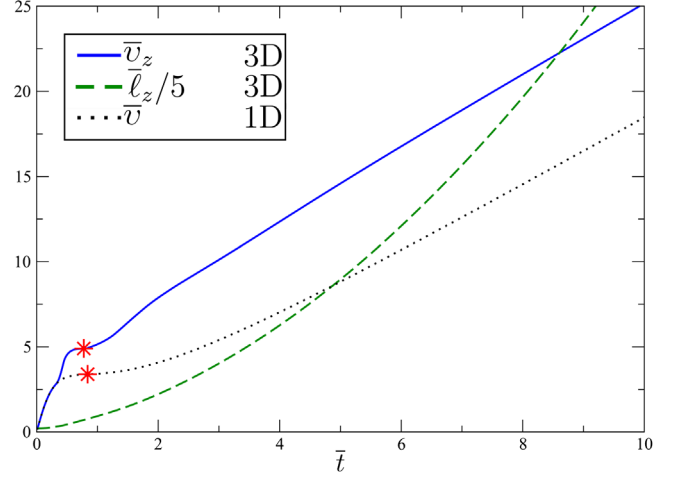

FIG. 22. Time evolution of the velocity $\bar{v}_z$ (continuous line) and the position $\bar{\ell}_z$ (here rescaled by a factor of 5, dashed line) of the jet termination, along the z axis and in dimensionless units (see Table II), from a 3D model [Eqs. (17) and (18)]. Input parameters are $Q_e = 12$, $V = 2$, and $F_{ve} = 12$. The corresponding velocity from quasi-1D simulations [Eqs. (12)–(15)], conducted with identical input parameters, is also shown for comparison (dotted line). A quasistationary point is found during the initial elongation (star).

To compare the 3D model of the electrospun jet with the quasi-1D representation [Eqs. (12)–(15)], one can consider the time evolution of the jet termination ℓ_z and its velocity v_z along the z axis, which is shown in Fig. 22 (Lauricella, Pontrelli, Coluzza *et al.*, 2015a). Here the same typical input values are used for the dimensionless parameters, $Q_e = 12$, $V = 2$, and $F_{ve} = 12$, as those employed in the quasi-1D case analyzed in Fig. 19 (Reneker *et al.*, 2000). In the 3D case, two sequential stages can be identified in the elongation process: the first stage is mainly biased by the sum of the viscoelastic and Coulomb forces, and the second one is dominated by the external electric field. Hence, a quadratic regime is observed in the second part of the dynamics, with the jet length evolving in time as $\ell_z \propto t^2$ and the velocity increasing nearly linearly in time. While all these results are consistent with findings for the quasi-1D case, the 3D model provides higher values of the achieved velocity (Fig. 22). In fact, this is related to the injection algorithm used to add new particles at the nozzle, which leads to extra charge, i.e., to further repulsive Coulomb force (~1.7 times the corresponding force value obtained in the 1D simulation).

A comparison between 3D simulations and experimental data was performed considering an electrospun solution of polyvinylpyrrolidone (PVP) prepared by a mixture of ethanol and water (17:3 v:v), at a concentration about 2.5 wt % (Lauricella, Pontrelli, Coluzza *et al.*, 2015a). The applied voltage is around 30 statV (~10 kV), and the collector is placed 16 cm from the nozzle. Other parameters of the test case are the jet radius $r_0 = 0.05$ cm, jet velocity $v = 200$ cm s^{-1} (Montinaro *et al.*, 2015), surface tension $\alpha = 21.1$ g s^{-2} (Yuya *et al.*, 2010), elastic modulus $G = 5 \times 10^4$ g cm^{-1} s^{-2} (Morozov and Mikheev, 2012), charge density $\rho_q = 44\,000$ statC cm^{-3}, zero-shear viscosity $\mu_0 = 0.2$ g cm^{-1} s^{-1} (Bühler, 2005; Yuya *et al.*, 2010), and extensional viscosity
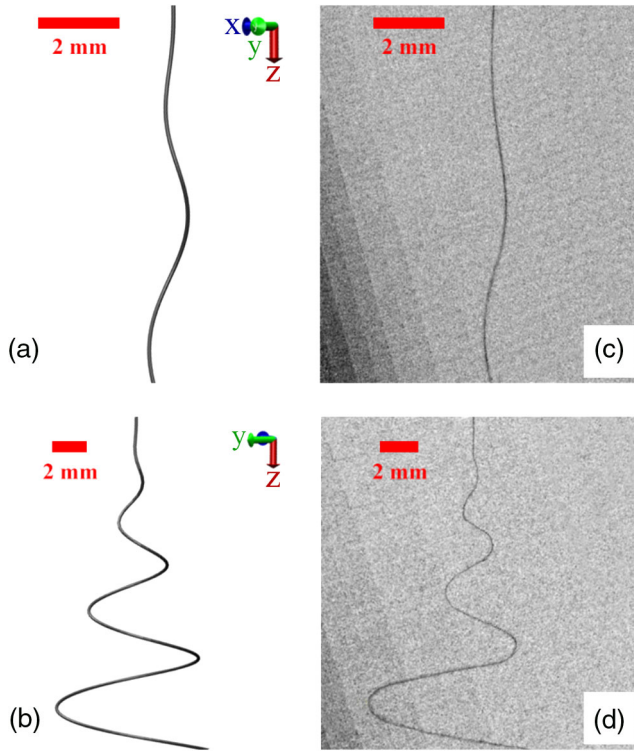
FIG. 23. Snapshots of the (a),(b) simulated and (b),(d) experimental jets, taken close to the nozzle (a),(c) at an early stage and (b),(d) in the bending regime of their dynamics. The experiment was performed with a solution of PVP prepared using a mixture of ethanol and water (17:3 v:v) (Montinaro *et al.*, 2015). The simulation is performed with the same conditions as in the experimental setup: applied voltage 30 statV (∼10 kV), and the collector placed 16 cm from the nozzle. The parameters of the PVP solution are taken from the literature: jet initial radius $r_0 = 0.05$ cm (Montinaro *et al.*, 2015), surface tension $\alpha = 21.1$ g s^{-2} (Yuya *et al.*, 2010), elastic modulus $G = 5 \times 10^4$ g cm^{-1} s^{-2} (Morozov and Mikheev, 2012), charge density $\rho_q = 44\,000$ statC cm^{-3}, zero-shear viscosity $\mu_0 = 0.2$ g cm^{-1} s^{-1} (Bühler, 2005; Yuya *et al.*, 2010), and extensional viscosity $\mu_e \sim 100\mu_0$ (Jian, Fridrikh, and Rutledge, 2006). From Lauricella, Pontrelli, Coluzza *et al.*, 2015a.

$\mu_e \sim 100\mu_0$ (Jian, Fridrikh, and Rutledge, 2006). The simulations showed that the model is able to reproduce the slight perturbation from the linear path to bending instability, along with fully 3D, out-of-axis motion. This is seen in Fig. 23, which compares the bending oscillations between two snapshots of the simulated jet [Figs. 23(a) and 23(b)] and high-frame-rate experimental micrographs [Figs. 23(c) and 23(d)] (Montinaro *et al.*, 2015) collected at an early stage and later regime of instability. Further, the bending instability can be described in terms of angular aperture Θ of the instability cone. The Θ value measured in the simulation is in the 30°–36° range, which is consistent with the experimental 29°–37° range (Montinaro *et al.*, 2015).

Lagrangian methods have been used extensively to span the space of parameters to probe the effects of different quantities on the electrospinning process (Thompson *et al.*, 2007; Kowalewski, Barral, and Kowalczyk, 2009; Sun, Zeng, and Wang, 2011; Coluzza *et al.*, 2014; Lauricella, Pontrelli,

Coluzza *et al.*, 2015a; Lauricella, Pisignano, and Succi, 2016; Yousefi *et al.*, 2018). For instance, 13 different parameters were studied, changed one at a time in the model to determine their effect on the final jet cross-sectional radius (Thompson *et al.*, 2007). The growth rate of the bending instability was also investigated by the stability analysis on a similar 3D Lagrangian model (Divvela and Joo, 2017). The jet was perturbed with an initial normal mode disturbance at an amplitude δ and frequency ω_p applied on several parameters (position, velocity, jet radius, viscosity, tensile stress, and external electric field). For instance, the perturbed ith bead charge $q_{p,i}$ reads $q_{p,i} = q_i + \delta q_\epsilon \exp(\omega_p t)$. At higher voltage and lower viscosity, the nonaxisymmetric bending instabilities were found to become dominant.

The versatility of this model allows extra force terms to be incorporated, as well as further algorithmic expedients to probe innovative experimental setups. In Sec. V.C, we review a few of these extensions, together with scenarios for their practical applications.

C. Advanced Lagrangian models

This section is focused on more recent advancement in the Lagrangian models for electrified polymer jets. The main improvements aim to address essentially two key points: First, refining the model by including force terms that were neglected as a first approximation. Physical mechanisms considered in the past decade include aerodynamics, focusing electric fields, and nanoparticles in the jet. Second, but no less important, is the attempt to improve the jet representation via different descriptive techniques and algorithms. Both improvements are reviewed here.

1. Aerodynamic effects

All Lagrangian models involve a set of EOM that can be modified flexibly to account for new force terms and extend applicability. For instance, aerodynamics and air-drag effects were not initially considered (Reneker *et al.*, 2000) because their contribution to stretching is much smaller than that from electrical forces under the typical conditions of electrospinning experiments. Nonetheless, not only may higher accuracy of the models be desirable, but there also exist variants of the experimental setup that involve a gas stream surrounding the nozzle, as in electroblowing (Um *et al.*, 2004; Wang *et al.*, 2005; Hsiao *et al.*, 2012). In these processes, the effects of air drag and lift cannot be neglected. Hence, these terms should be added in the momentum balance, Eq. (17). The dissipative air-drag term is a braking force oriented along the tangent to the axis of the jet, with its magnitude depending on the geometry of the jet, which evolves in time. Based on experimental results (Yarin, 1993), the air-drag force acting on the ith bead can be assessed by the empirical relation (Ziabicki, 1961; Ziabicki and Kawai, 1991)

$$\mathbf{f}_{\mathrm{drag},i} = -\xi \pi r_i \ell_{ui} \rho_{\mathrm{air}} \left(\frac{2r_i}{\nu_{\mathrm{air}}} \right)^{-\zeta} (v_i^{\parallel})^{1+\eta} \boldsymbol{\tau}_{ui}, \quad (19)$$

where ν_{air} and ρ_{air} are the air kinematic viscosity and density, respectively, $\ell_{ui} = |\mathbf{R}_i - \mathbf{R}_{i-1}|$ is the distance between the ith

bead and its upper bead, and the term $v_i^{\parallel} = (\boldsymbol{v}_i - \boldsymbol{v}_{\text{air}}) \cdot \boldsymbol{\tau}_{ui}$ denotes the tangent component of the relative jet velocity with respect to the airflow velocity $\boldsymbol{v}_{\text{air}}$. In Eq. (19), the symbols ξ, ζ, and η denote three coefficients to empirically assess. As plausible values of these coefficients, Ziabicki and Kawai (1991) empirically determined them as $\xi = 13/20$, $\zeta = 4/5$, and $\eta = 1/5$. These coefficients can be fitted to the drag force data measured in polymeric freely moving filaments using an experimental apparatus equipped with an electronic tensiometer (Ziabicki, 1961). Overall, the air drag plays the role of a dissipative term absorbing the air perturbations in a nonlinear way with respect to $v_i^{\parallel}$. Using Eq. (19) and assuming the volume conservation so that $r_i = r_0 \sqrt{\ell_{\text{step}}/\ell_{ui}}$, it is possible to write the dissipative friction coefficient γ_i as (Lauricella, Pisignano, and Succi, 2016)

$$\gamma_i = \xi \pi \frac{\rho_{\text{air}}}{m_i} \left(\frac{2}{\nu_{\text{air}}}\right)^{-\zeta} \ell_{\text{step}}^{(1/2)(1-\zeta)} r_0^{1-\zeta}. \qquad (20)$$

Inserting Eq. (20) into Eq. (19), the drag force reads

$$\mathbf{f}_{\text{drag},i} = -m_i \gamma_i \ell_{ui}^{(1/2)(1-\zeta)} (v_i^{\parallel})^{1+\eta} \boldsymbol{\tau}_{ui}, \qquad (21)$$

which dissipates the air fluctuations. The perturbations are in turn due to local interactions of random high-frequency collisions of the gas molecules with the jet, providing a Brownian motion component that contributes to the overall dynamics. The macroscopic force resulting from such fluctuations is taken as a stochastic process with zero mean and diffusion coefficient D_v in the velocity space, modeling the total displacement of the jet due to the sum of particle impacts over a time window much longer than the inverse of the particle collision frequency. Hence, the random force reads (Lauricella, Pisignano, and Succi, 2016)

$$\mathbf{f}_{\text{rand},i} = \sqrt{2m_i^2 D_v} \boldsymbol{\eta}_i(t), \qquad (22)$$

where D_v is assumed constant and equal for all beads, and $\boldsymbol{\eta}_i$ is a three-dimensional vector of independent stochastic processes, where each component along one of the three unit vectors ($\mathbf{i}$, $\mathbf{j}$, $\mathbf{k}$) is taken as $\eta_i = d\xi_i(t)/dt$. Here $\xi_i(t)$ denotes a Wiener process, namely, a stochastic process with stationary independent increments (Durrett, 2019). It is worth observing that the insertion of the last term in Eq. (17) yields a nonlinear Langevin-like stochastic differential equation in the set of EOMs (Lauricella, Pontrelli, Pisignano, and Succi, 2015). As a consequence, the simulation requires a time marching scheme able to integrate the random processes preserving a reasonable order of convergence (Tuckerman, 2010; Kloeden and Platen, 2013). An example of a strong convergence scheme was reported (Lauricella, Pontrelli, Pisignano, and Succi, 2015) for the numerical integration of the stochastic term in Eq. (22). A smaller time step $\Delta t \sim 10^{-8}$ s in the integration scheme improves the numerical accuracy, although it increases the computational cost. As an alternative, the energy spectrum (provided as an input parameter) of the random process can be exploited to simulate the random velocity displacement as a sum of m harmonic functions

(Battocchio, Sutcliffe, and Teschner, 2017). These functions would have frequencies ω_j with $j \in [1, \dots, m]$, and amplitude derived from the energy spectrum, assumed constant up to a cutoff frequency and 0 at higher frequencies. This approach may be numerically integrated with a larger time step Δt by setting a low-frequency cutoff, thus saving significant computational time.

In a 3D framework, the lift force is also acting on the jet dynamics along the normal (curvature) vector. The aerodynamic lift force related to the flow speed can be written for the ith bead in the linear approximation (for small bending perturbations) as (Yarin, 1993; Lauricella, Pisignano, and Succi, 2016)

$$\mathbf{f}_{\text{lift},i} = -\ell_{ui} k_i \rho_{\text{air}} (v_i^{\parallel})^2 \pi \left(\frac{r_{i+1} + r_i}{2}\right)^2 \mathbf{n}_i, \qquad (23)$$

where the factor ℓ_{ui} denotes the length of the jet segment. The lift term scales quadratically with $v_i^{\parallel}$, thus playing a significant role for high enough relative velocity of the airflow.

The effects of the three terms given by Eqs. (21)–(23) on the extended EOM were investigated in the electrospinning simulations of a PVP solution under three different conditions of airflow velocity, $\boldsymbol{v}_{\text{air}} \in [0, -1000, -2000]$ cm s^{-1}, oriented along the unit vector $\mathbf{k}$ (Lauricella, Pisignano, and Succi, 2016). The air kinematic viscosity was set to $\nu_{\text{air}} = 0.151$ cm^2 s^{-1}, while $D_{v,i}$ was taken equal to γ_i for all beads for simplicity. In the case $\boldsymbol{v}_{\text{air}} = -2000$ cm s^{-1}, the larger lift force contributes to the bending instabilities (Fig. 24). In particular, the synergic action of the lift and Coulomb repulsive forces boosts bending instabilities at an earlier stage and increases the chaotic behavior of the jet in the subsequent dynamics. This is seen in Fig. 24 by the larger statistical dispersion of the shadowed cone (the thickness of the instability envelope cone wall) computed as the isosurface with constant value 0.001 of the normalized numerical density field $\rho_{\text{bead}}(x, y, z)$, namely, the probability to find a jet bead in
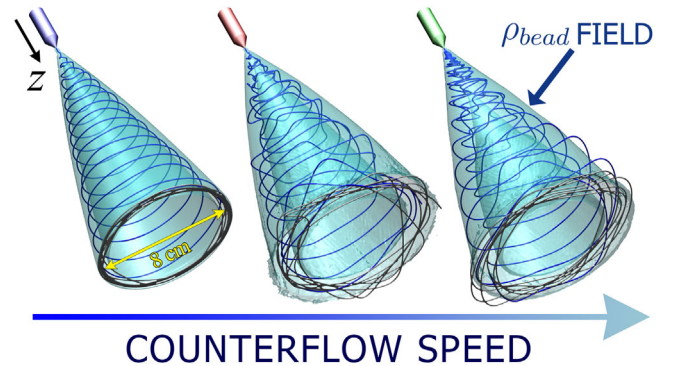

FIG. 24. Simulation snapshots of the three different cases of an electrospun polymer solution jet with air counterflow. From left to right, the airflow velocity along the unit vector $\mathbf{k}$ (collinear with the z direction) is $\boldsymbol{v}_{\text{air}} = 0$, -1000, and -2000 cm/s, respectively. The jet is shaded in the cones, and the nanofibers deposited on the collector are in black at the termination of the cones. The shaded isosurfaces represent the normalized numerical density field $\rho_{\text{bead}}(x, y, z)$ of constant value equal to 0.001. Adapted from Lauricella, Pisignano, and Succi, 2016.

a control volume near the coordinates (x, y, z). As a consequence, the high-speed gas flow significantly affects the distribution of the deposited nanofibers, providing a broader deposition pattern and a decreased fiber radius due to the larger bending instabilities. In these simulations, the jet was assumed to interact with a uniform airflow field. Nonetheless, computational fluid dynamics software can be used to simulate an arbitrary airflow field. As an example, the velocity flow field $\mathbf{v}_{\mathrm{air}}(x, y, z)$ could be computed by solving the corresponding Navier-Stokes equation (Sun, Zeng, and Wang, 2011). Hence, $\mathbf{v}_{\mathrm{air}}$ was coupled with the Lagrangian model to investigate the effect of airflow in the spinning process (Sun, Zeng, and Wang, 2011).

2. Electric and magnetic focusing fields

Thus far the external electric field $\mathbf{E}_0 = (\Delta\Phi_0/h)\,\mathbf{k}$ in Eq. (17) had been assumed to be oriented along the $\mathbf{k}$ axis over the entire space. Nonetheless, in a real electrospinning setup, the electric field distribution $\mathbf{E}_0(x, y, z)$ depends on both the collector and needle electrode shapes, and this might alter the direction of the jet stretching. Several works investigated the effects of auxiliary electrodes used for the generation of extra electric fields (also named focusing electric fields) that drive the electrospun jet and affect the bending instability (Deitzel, Kleinmeyer, Hirvonen, and Beck Tan, 2001; Bellan and Craighead, 2006; Neubert *et al.*, 2012). Such effects can be accounted for by resolving the electric field distribution $\mathbf{E}_0(x, y, z)$ over the space. Despite being computationally expensive, finite difference or finite element methods are usually exploited to solve the Poisson equation $\nabla^2\Phi_0(x, y, z) = \rho_q(x, y, z)/\varepsilon$ and obtain the field $\mathbf{E}_0(x, y, z) = -\nabla\Phi_0(x, y, z)$. For instance, the Lagrangian model was extended to investigate the effect of a conical needle electrode on the radius of electrospun nanofibers (Hamed, Shehata, and Elosairy, 2018). The Poisson equation could be solved only once at the beginning of the simulation and the result inserted into Eq. (17) as an input parameter. However, a correct computation of the electric field should also account, in the Poisson equation, for the time-dependent charge distribution on the jet path, paying high computational costs for the solution of the Poisson problem at each time step. Within this context, since the electric potential difference $\Delta\Phi_0$ should be constant at the nozzle tip, another strategy, shown in Fig. 25, exploited the method of images, where fictitious mirror charges are placed symmetrically to the collector plane to always match the condition $\Phi_0 = 0$ at the collector (Kowalewski, Barral, and Kowalczyk, 2009). Thus, the total electric field is the superposition of the external static field and a time-dependent intrajet field generated by the jet charges, with the latter computed as in Eq. (17) but now with the direct summation over both real and mirror jet charges.

Furthermore, it is possible to drive both the stretching direction and preferential orientations of the jet at the collector by a time-dependent manipulation of the external electric field, acting as a dynamic focusing field. It was experimentally observed that a time-varying square wave potential is able to periodically deflect the jet between two symmetric, rotatable platelike electrodes, coaxially placed near the needle at a distance of 8.5 cm (Grasl *et al.*, 2013). Rotating electric fields
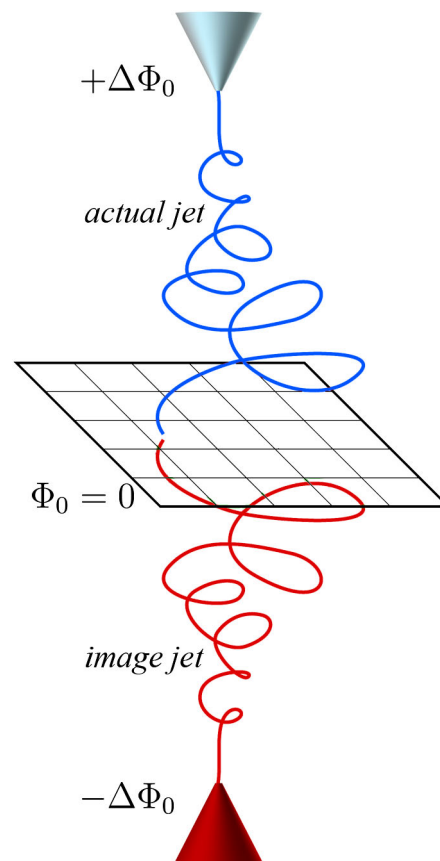

FIG. 25. Idealized electrostatic setup with fictitious charges of the image jet, which are used to maintain the electric potential condition $\Phi_0 = 0$ at the grounded plane during process modeling.

can also be generated by a series of fixed capacitor plates appropriately arranged in space and connected to an alternating power source (Kyselica and Enikov, 2016; Kyselica *et al.*, 2018). For instance, assuming the hexagonal arrangement of the plates and a three-phase power source connected to them (Fig. 26), as a first approximation the external electric field can be assumed to be uniformly distributed in space so that the total electric field $\mathbf{E}_0 = \mathbf{E}_0^{\parallel} + \mathbf{E}_0^{\perp}$ is the superposition of a stretching electric field $\mathbf{E}_0^{\parallel} = (E_x, 0, 0)$ parallel to the $\mathbf{k}$ axis and an orthogonal rotating term $\mathbf{E}_0^{\perp} = (0, E_y, E_z)$. In equations,

$$E_y(A, \omega, t) = A\cos(\omega^{\perp} t), \tag{24a}$$

$$E_z(A, \omega, t) = A\sin(\omega^{\perp} t), \tag{24b}$$

where $A(\mathrm{g}^{1/2}\,\mathrm{cm}^{-1/2}\,\mathrm{s}^{-1})$ is the magnitude of $\mathbf{E}_0^{\perp}$ and $\omega(\mathrm{s}^{-1})$ is the angular (switching) frequency of the field. By inserting the term $q_i\mathbf{E}_0^{\perp}(A, \omega, t)$ into Eq. (17), the morphology of electrospun materials could be studied for several pairs of A and ω values (Lauricella *et al.*, 2017). In agreement with both experimental observations (Grasl *et al.*, 2013; Kyselica and Enikov, 2016; Kyselica *et al.*, 2018) and further numerical simulations (Kyselica, Enikov, and Anton, 2019), the jet was found to support rather regular oscillatory patterns, which are
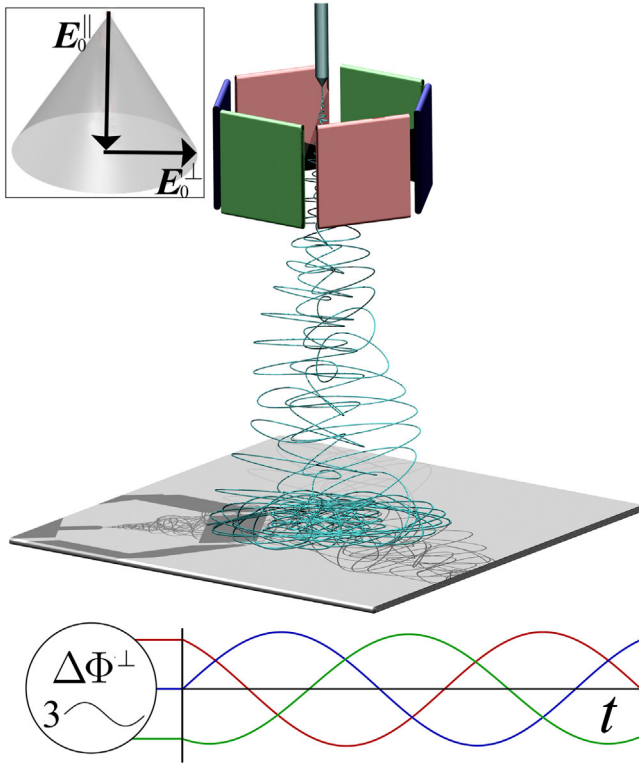
FIG. 26. Simulation snapshot of the electrospinning process in the presence of an orthogonal rotating electric field at high frequency ($\sim 10^4$ Hz). The jet is stretched by a longitudinal electric field $\mathbf{E}_0^{\parallel}$. The orthogonal electric field ($\mathbf{E}_0^{\perp}$) can be generated by a series of capacitor plates, hexagonally arranged and connected to a three-phase power source, as represented in the bottom part of the figure. Here the three-phase voltage differences $\Delta\Phi_0$ correspond to the different pairs of capacitor plates. Adapted from Lauricella *et al.*, 2017.

controlled by tuning A and ω. This offers an opportunity to deposit oriented nanofibers even on a static collector, which is interesting for the design of new porous materials.

In the context of magnetic-field-assisted electrospinning, Lagrangian models can be easily modified to simulate the effect of a stationary, space-distributed magnetic field. In particular, the Lorentz force $\mathbf{f}_L$ for an ith bead with velocity $\boldsymbol{v}_i$ and charge q_i is given by

$$\mathbf{f}_{L,i} = q_i \boldsymbol{v}_i \times \mathbf{B}_0(x, y, z), \quad (25)$$

where $\mathbf{B}_0(x, y, z)$ is the magnetic field at the coordinates (x, y, z) of the ith bead. Hence, the term is added to the momentum equation (17) to simulate the coupling effects of electric forces and the magnetic field. Theoretical works agree well with the experimental data, showing that $\mathbf{B}_0$ could significantly alter the nonaxisymmetric bending or whipping instabilities of the jet (Xu, Wu, and Nawaz, 2011; Badieyan and Janmaleki, 2015). The jet can be focused to obtain nanofibers with preferential orientation in given regions of the collector.

3. Multiple jets in electrospinning

Multiple jets were introduced in electrospinning to increase the fiber production rate. In addition, the rational design of nozzle patterns, issuing many jets simultaneously, might be important to obtain areas uniformly covered with nanofibers. Thus, numerical investigations were performed to explore the physics of the jet-jet interactions. For instance, the Lagrangian model (Sec. V.B.3) was generalized for the case of multiple bending jets with mutual Coulombic interactions (Theron *et al.*, 2005). A simple way to compute the Coulomb force acting on the ith bead of the kth jet is to extend the direct summation of the Coulomb term in Eq. (17) as follows:

$$\mathbf{f}_{c,ik} = q_{ik} \sum_{l=1,m} \sum_{\substack{j=1,n(l) \\ jl \neq ik}} \frac{q_{jl}}{|\mathbf{R}_{ik} - \mathbf{R}_{jl}|^3} (\mathbf{R}_{ik} - \mathbf{R}_{jl}), \quad (26)$$

where j is now running over the $n(l)$ beads of the lth jet among the m jets. In this way, the bending instabilities of a jet in a multinozzle setup were predicted to be driven not only by self-induced Coulomb forces but also by mutual interjet Coulombic repulsive interactions (Fig. 27). Further numerical studies (Angammana and Jayaram, 2011b; Li *et al.*, 2015) showed that the stretching ratio in a multijet setup is larger than that observed in single-jet electrospinning. In particular, the stretching ratio of a jet increases by decreasing the mutual distance between neighboring jets.

4. Dynamic refinement in Lagrangian models

All Lagrangian models reviewed thus far exploit the injection algorithm mentioned in Sec. V.B.2: all beads are uniformly inserted at the nozzle, with the mutual distance ℓ_{step}. Nonetheless, the distances ℓ_{ui} and ℓ_{di} between any couple of consecutive elements in the bead chain increase along the dynamics because of the stretching induced by the intense electric forces. Assuming volume conservation, a typical value $r/r_0 = 10^{-2}$ in the jet cross section measured at the collector provides the increase, $\ell_{ui} = 10^4 \ell_{\text{step}}$, in the discretization length of the jet. Thus, the discretization close to the collector becomes rather coarse (both ℓ_{ui} and $\ell_{di} \gg \ell_{\text{step}}$) to effectively model the filament, and the information (position, velocity, radius, stress, etc.) describing the jet is scattered downstream. To tackle this issue, an adaptive dynamic refinement procedure was developed, maintaining the lengths ℓ_{ui} and ℓ_{di} for any ith element below a prescribed characteristic threshold length $\ell_{\max}$ (Lauricella *et al.*, 2016). Whenever a bead length ℓ_{ui} or ℓ_{di} is larger than $\ell_{\max}$, the jet description is refined by discretizing it uniformly at the length step value ℓ_{step}, given as an input. The discretization was performed by cubic spline interpolations (De Boor, 1978) of the main quantities describing the jet beads (positions, jet radius, velocities, stress). To perform the interpolation, the total arc length at time t is assessed as

$$\ell_{\text{jet}}(t) = \sum_{i=1}^{n} \ell_{ui}(t), \quad (27)$$

where the sum is over the n beads so that all distances between the element pairs $(i + 1, i)$ are accounted for. Note that the
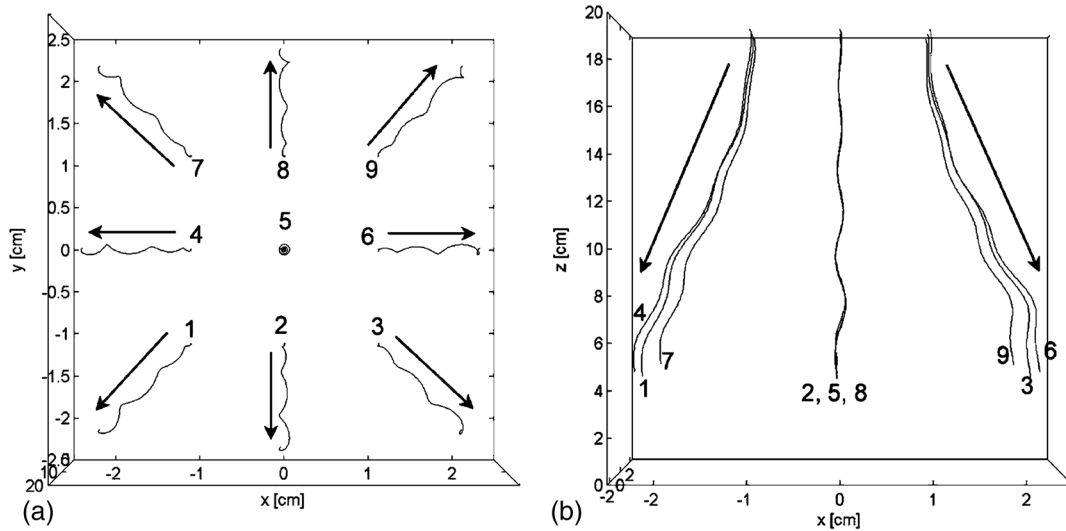
FIG. 27. The paths of nine jets in a 3×3 matrix arrangement of the nozzles shown from two different points of view. (a) Top view of all jets of the 3×3 matrix. (b) Side view of all jets. Adapted from Theron *et al.*, 2005.

stretching ratio $\lambda(t)$ at time t is assessed as $\lambda(t) = \ell_{\text{jet}}(t)/\ell_{\text{jet}}^0$. Hence, the usual curvilinear parameter s is introduced (Secs. V.A.4 and V.B.3) and used to define the discretization mesh of the jet. In particular, the discrete set of values $\{s_k\}_{k=1,\ldots,n}$ of the curvilinear parameter $s \in [0, \ell_{\text{jet}}^0]$ is estimated for each kth bead by using

$$s_k(t) = \frac{1}{\lambda(t)} \sum_{i=1}^{k} \ell_{ui}(t). \qquad (28)$$

Despite the s values still being frozen in the jet element, the set $\{s_k(t)\}_{k=1,\ldots,n}$ is now time dependent since the jet discretization is adapted to always satisfy the condition $\ell_{ui} < \ell_{\max}$ during the jet evolution. Hence, the set of $\{s_k(t)\}_{k=1,\ldots,n}$ values represents the mesh used to build the cubic spline. Given a generic quantity y, the data y_k are tabulated over the set of values $s_k \lambda$, where $s_k(t)\lambda(t)$ denotes the arc length from the nozzle to the kth bead of the jet at time t. Thus, $y_k = y(s_k \lambda)$ were used to compute the coefficients of the cubic spline, following a well-established algorithm (Press *et al.*, 1996). Then a uniform parametrization was enforced by imposing all lengths of the elements equal to ℓ_{step}. The new mesh s_i^* is defined as

$$s_i^* = \ell_{\text{jet}}^0 \frac{i}{n^*}, \qquad i = 1, 2, \ldots, n^*, \qquad (29)$$

where $n^* = \lambda(t)\ell_{\text{jet}}^0/\ell_{\text{step}}$ is the number of jet beads in the new representation. Another possible criterion for building the new mesh is to keep all the old beads at their positions and to add only new beads where the bead distance in the pair $(i+1, 1)$ is $\ell_{ui} > \ell_{\max}$. Indeed, since all the old beads are maintained as knots of the mesh along the dynamic refinement, the errors introduced by the interpolation procedure are mitigated because they affect only the new inserted bead.

Finally, the new values $y(s_i^*\lambda)$ are computed for any ith bead by the spline interpolation. The procedure is repeated for

positions, jet radius, stress, and velocities of the jet beads to provide the quantities in the new mesh $\{s_i^*\}_{i=1,\ldots,n^*}$ (Lauricella *et al.*, 2016). As a practical application of the mesh refinement procedure, the algorithm was applied to simulate the electrospinning of a polymeric solution containing heavy nanoparticles, which trigger varicosity along the jet modifying the path from the nozzle toward the collector (Fig. 28) (Lauricella, Pisignano, and Succi, 2017). Here the mesh refinement showed the capability of representing the fluctuation of the cross section along the jet, also preserving a fine jet
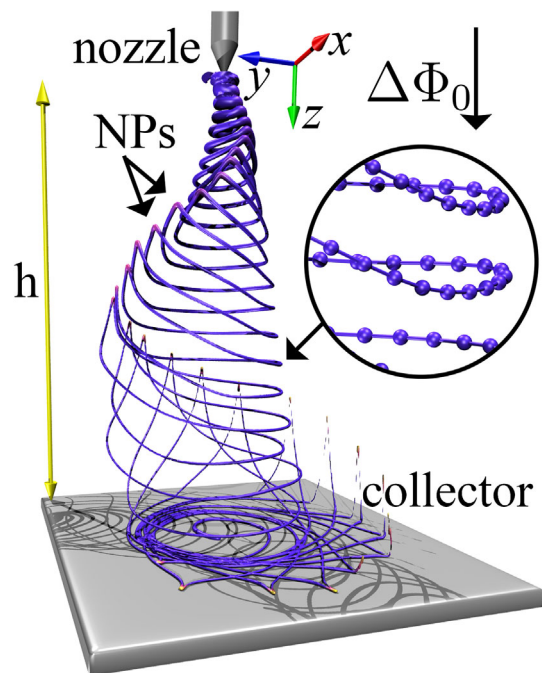

FIG. 28. Simulation snapshot illustrating an electrified polymer solution jet embedding nanoparticles. h, distance between the collector plate and the nozzle; $\Delta\Phi_0$, applied voltage difference. Adapted from Lauricella, Pisignano, and Succi, 2017.

representation close to the collector. Small values of the threshold length ℓ_{max} increase the number of beads in the simulation and the associated computational costs; see also Sec. IV and strategies reviewed there for saving computational time.

5. Limits of Lagrangian models

All Lagrangian models reviewed here assume the polymer solution as fully spinnable. In particular, relevant dimensionless numbers (e.g., the capillary and Deborah numbers) should be preliminarily considered to justify the assumption of the solution spinnability as described in Secs. II and V.B.2. In other words, one should note that a Lagrangian model is not to be used to foresee the spinnability of a polymer solution numerically because this is already assumed in the model. As a second limit, since the jet is represented as a continuous chain of particles connected pair by pair through viscoelastic springs, Lagrangian models are ineffective for investigating failure modes, such as jet breaking and splitting, in fluid polymeric filaments. These deformations could be analyzed for the case of conducting liquids in terms of a critical value of the linear electric charge density carried by the jets (Zubarev and Zubareva, 2004, 2005). Similarly, Lagrangian models cannot display varicose instabilities in the jet, such as those due to capillary pressure.

Further, we point out that the rheological behavior is highly sensitive to the phenomenological, constitutive law embedded in the viscoelastic springs connecting neighbor particles. This fact is not unlike what is generally remarked upon in Eulerian descriptions (e.g., numerical solvers of the Navier-Stokes equations), where a constitutive law is also needed.

Finally, any Lagrangian model exploits proper algorithms to treat the fluid injection at the nozzle; see Sec. V.B.2. As a consequence, the modeling of the Taylor cone is missed. However, this specific limit could be tackled by coupling Lagrangian models with Eulerian solvers of the EHD equations governing the fluid cone used, for instance, to model the tip streaming of charged droplets (Reznik *et al.*, 2004; Collins *et al.*, 2008, 2013).

D. Polymer network dynamics in electrified jets

This section reviews efforts describing the polymer network dynamics for highly elongated, electrified polymer solution jets. With strain rate $\dot{\varepsilon} \geq 10^3$ s^{-1} (Reneker *et al.*, 2000, 2007; Bellan, Craighead, and Hinestroza, 2007), stretching in these jets can potentially increase the structural order within spun nanofibers, enhance their mechanical properties (such as the elastic modulus and strength) (Rein *et al.*, 2007; Burman, Arinstein, and Zussman, 2008; Greenfeld *et al.*, 2011; Zussman and Arinstein, 2011), and shift the phase transition temperature, e.g., the melting temperature (Arinstein *et al.*, 2011; Liu *et al.*, 2011). At the same time, rapid solvent evaporation during electrospinning can lead to an increased polymer concentration at the jet boundary (Koombhongse, Liu, and Reneker, 2001; Guenthner *et al.*, 2006; Dayal and Kyu, 2007), forming a solid skin or a heterogeneous and porous structure (Casper *et al.*, 2004; Dayal and Kyu, 2007; Dayal *et al.*, 2007; Greenfeld *et al.*, 2011), which may lead to
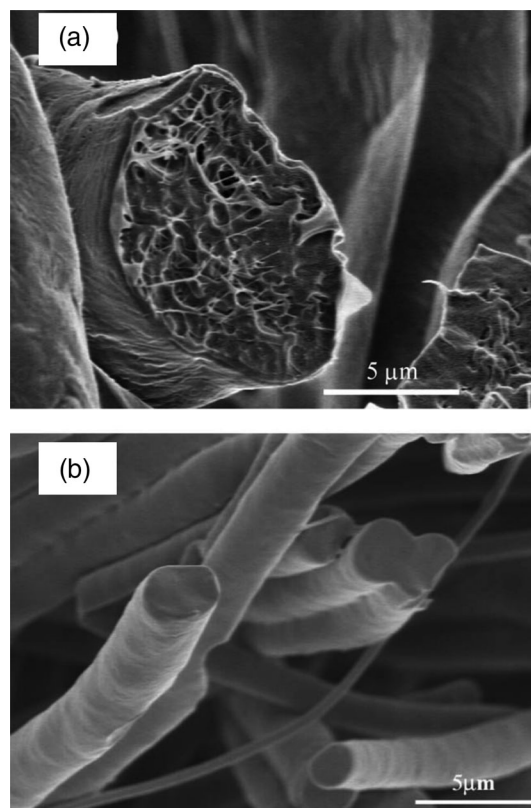

FIG. 29. Stretching and evaporation involving electrified polymer solution jets. SEM images of nanofibers with 10 wt % PCL with molar mass 80 kDa, dissolved in dichloromethane and DMF (75 : 25 wt %), electrospun by an electric field of 0.63 kV/cm. (a) High flow rate (20 ml/hr) resulting in heterogeneous fibers. (b) Low flow rate (3 ml/hr) resulting in homogeneous fibers. From Arinstein and Zussman, 2011.

buckling of the fibers (Arinstein, Avrahami, and Zussman, 2009). The simultaneous effects of stretching and evaporation (Arinstein and Zussman, 2011) are illustrated in Fig. 29. In this respect, the study of electrified polymer solution jets, and specifically of the evolution of the polymer entangled network during electrospinning, which is typically followed by stress relaxation (Vasilyev *et al.*, 2017), was aimed at clarifying the microstructure of spun nanofibers, and at improving their mechanical, electrical, and optical properties. Modeling of the dynamic evolution of the entangled polymer network in electrospun jets predicted substantial longitudinal stretching and radial contraction of the network, i.e., a transformation from an equilibrium state to an almost fully stretched state (Arinstein and Zussman, 2011; Greenfeld *et al.*, 2011). This prediction was verified by x-ray phase-contrast imaging of electrospun jets, which revealed a noticeable increase in polymer concentration at the jet center, as well as a concentration crossover within a short distance of the jet initiation point (Greenfeld *et al.*, 2011, 2012).

1. Polymer dynamics during electrospinning

The flow of a solution jet consists of both axial and radial velocity components (Fig. 30). The analysis of electrically driven fluid jets revealed that the axial velocity of the jet v
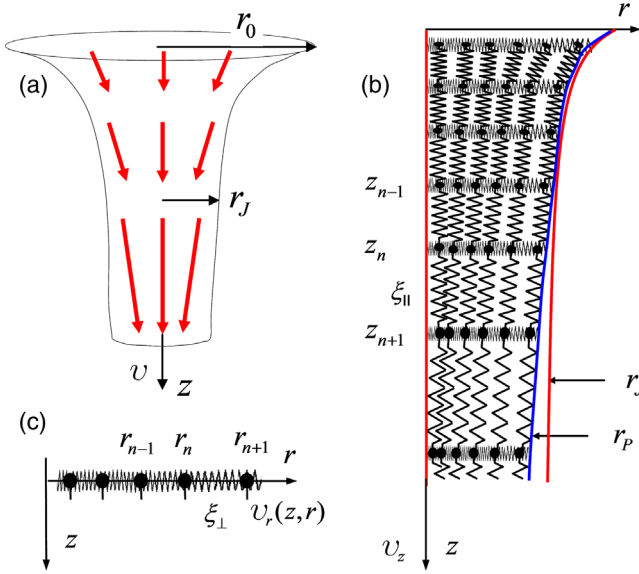
FIG. 30. (a) Illustration of the flow of an electrified polymer solution jet. Definition of an effective 1D beads-and-springs system (b) in the axial direction and (c) in the radial direction (Greenfeld *et al.*, 2011).

FIG. 31. Universal plot of the polymer network conformation. Relative axial stretching ξ_{II}/bN_s, radial contraction $\xi_\perp/\xi_0$, and molecular orientation O vs the normalized axial position kz/r_0. bN_s is the length of a fully extended subchain. The point S at the top of the plot indicates the criterion for "full" network extension. The results were obtained by random walk simulations and theoretical modeling (Greenfeld *et al.*, 2011).

reaches an asymptotic regime sufficiently far from the needle, which can be described by a power law of the distance along the jet z:

$$\frac{v}{v_0} \approx k_V^2 \left(\frac{z}{r_0}\right)^{2\beta}, \tag{30}$$

where the exponent β varies between $1/4$ and 1 (Kirichenko *et al.*, 1986; Spivak and Dzenis, 1998; Hohman *et al.*, 2001b; Higuera, 2006; Reznik and Zussman, 2010), k_V is a dimensionless parameter, r_0 is the jet initial radius, and v_0 is the initial velocity, $v_0 = Q/\pi r_0^2$. Assuming volume conservation, the jet local radius $r_J = r_0(v/v_0)^{-1/2}$ (see Fig. 31) and the radial velocity v_r can be derived. A rough approximation of k_V in Eq. (30) can be obtained by using a simple scaling approach: the velocity gradient scales as $\nabla v \approx v_0 k_V^2/r_0^2$; the upper bound for σ_q (the surface charge density on the jet), assuming static conditions, scales as $\sigma_q/\sigma_e E$, where σ_e is the solution electric conductivity and E is the electric field. The electric shear stress is therefore $\tau_t \approx \sigma_q E \approx \sigma_e E^2$, producing a velocity gradient $\nabla v \approx \tau_t/\mu \sim \sigma_e E^2 \mu^{-1}$. Hence, $k_V \sim \nabla v^{1/2} v_0^{-1/2} r_0$ or $k_V \sim r_0^1 \sigma_e^{1/2} \mu^{-1/2} v_0^{-1/2} E^1$. A more accurate calculation yielded $k_V \cong r_0^{2/3} v_0^{-2/3} \sigma_e^{1/4} \mu^{-5/12} E^{5/6} \sim 1$ (Reznik and Zussman, 2010).

Polymer chains dissolved in a sufficiently concentrated solution create an entangled network [Fig. 30(b)], a prerequisite for spinnability. A chain section between two subsequent entanglements is a strand, or a subchain, consisting of N_s rigid segments (Kuhn monomers), each of size $b \cong 1$ nm. Given the solution concentration ϕ (in terms of the polymer volume fraction), the network mesh size (i.e., the average subchain length) is given by $\xi_0 \approx b\phi^{-1} \approx bN_s^{1/2}$ for ideal chains,
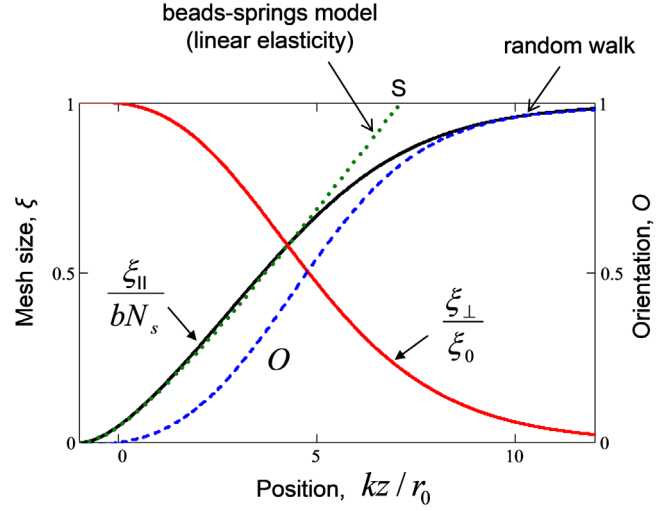
allowing one to model the network as a 3D beads-and-springs lattice, where each bead represents the mass m and size ξ_{eff} of a subchain ($\xi_{eff} \propto \xi_0$) and the springs represent the linear entropic elasticity T/ξ_0^2 (here T is the temperature in units of the Boltzmann constant k_B) of the subchains connected to each bead.

The hydrodynamic force acting on a subchain can be defined, and the dynamics of the network can then be described using the following difference-differential equations (Greenfeld *et al.*, 2011):

$$m\frac{d^2 z_n}{dt^2} = \xi_{eff}\mu\left[v(z_n) - \frac{dz_n}{dt}\right] + \frac{T}{\xi_0^2}\{[z_{n+1} - z_n - \xi_0]$$
$$- [z_n - z_{n-1} - \xi_0]\}, \tag{31a}$$

$$\xi_{eff}\mu v_r(r_n) + \frac{T}{\xi_0^2}\{[r_{n+1} - r_n - \xi_\perp] - [r_n - r_{n-1} - \xi_\perp]\} = 0. \tag{31b}$$

The corresponding solution, depicted in Fig. 31, predicts an affine stretching of the network:

$$\frac{\xi_\|(z)}{\xi_0} \approx \frac{v/v_0}{1 - (1/\alpha_v)d(v/v_0)/d(z/r_0)} \approx \frac{v(z)}{v_0}, \tag{32}$$

where α_v is a dimensionless parameter ($\alpha_v \gg 1$).

The dynamic conformation of subchains can be described using a random walk simulation, where each step represents a single monomer. The probability of stepping in a specific direction is determined by an effective potential, which arises from the external forces acting at the subchain ends, which propagate along the subchain, and the local hydrodynamic force acting directly on monomers (Fig. 32). For a given force
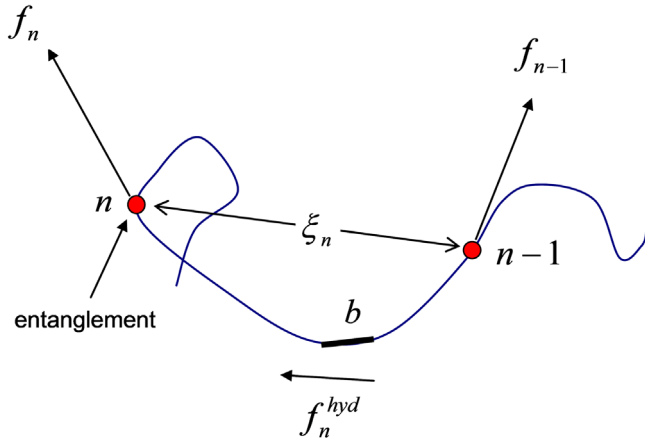
FIG. 32. Forces acting on a subchain. External forces (f_n, f_{n-1}) act at the chain ends, and a hydrodynamic force f_n^{hyd} acts on each monomer.

vector F acting on a monomer (normalized as $f = Fb/k_BT$), the probabilities for a random walk step are

$$P_x^{\pm} = \frac{\exp(\pm f_x)}{2\Sigma_x \cosh(f_x)} \qquad (33)$$

in each of the Cartesian directions (Greenfeld *et al.*, 2011). The monomer forces in the radial and axial directions are given by

$$f_z \cong f_0 + \sum_{i=1}^{n} f_i^{\text{hyd}} \cong f_0 + \tau_0(v_z - v_0)/b, \qquad (34a)$$

$$f_r \cong f_0 \approx 3b/\xi_0 \approx 3\phi, \qquad (34b)$$

where f_0 is caused by an effective stretching force acting on subchains in a network at rest and $\tau_0 \approx \mu_s b^3/k_BT$ is the monomer relaxation time related to the solvent viscosity μ_s. The hydrodynamic force in the radial direction is small compared to the force in the axial direction since $f_r f_z \cong v_r/v \cong r/z \ll 1$ and was therefore neglected. Since the dominant force acts at the subchain ends, the stepping probabilities are assumed to remain uniform along the subchain, and the axial stretching and radial contraction can be written using Eqs. (33) and (35) (Greenfeld *et al.*, 2011):

$$\frac{\xi_{\parallel}}{\xi_{\max}} \cong \frac{\sinh(f_z)}{Q}, \qquad (35a)$$

$$\frac{\xi_{\perp}}{\xi_{\max}} \cong \frac{\sinh(f_r)}{Q}, \qquad (35b)$$

$$Q = \cosh(f_z) + 2\cosh(f_0). \qquad (35c)$$

Shortly after the jet start but before the network approaches full stretching ($f < 1$), the relative longitudinal elongation of a subchain can be approximated by

$$\frac{\xi_{\parallel}}{\xi_0} \approx \frac{\xi_0 v_0 \tau_0}{3b^2}\left(\frac{v}{v_0}\right) \approx \frac{v}{v_0}, \qquad (36)$$

as obtained using the dynamic model, Eq. (32). The condition for the affine stretching is satisfied with a prefactor $\xi_0 v_0 \tau_0/(3b^2) = 1$. The simulation allows the analysis to be expanded to large chain elongations with nonlinear elasticity, showing that subchains approach full extension not far from the jet start (<1 mm) (Fig. 31). The criterion established for such a full extension (marked by point S in Fig. 31) using Eq. (32) or (36) is when the jet velocity rises above its initial value by a factor equal to the inverse of the polymer volume fraction:

$$\frac{v_S}{v_0} \approx \frac{\xi_{\parallel,S}}{\xi_0} \approx \frac{bN_s}{bN_s^{1/2}} \approx N_s^{1/2} \approx \phi^{-1}, \qquad (37)$$

which occurs at a jet radius reduction ratio of $r_0/r_S \approx N_s^{1/4} \approx \phi^{1/2} \sim 2 - 10$. Note that the relative velocity and radius at the stretching crossover point are found to depend only on the solution concentration and to be completely independent of the electrospinning materials and conditions (e.g., molar mass and electric field). The transformation of subchains from a coil-like equilibrium state into a stretched state was found to occur as a continuous crossover and no phase transition was observed, in contrast to the well-known coil stretch transition in unentangled chains (de Gennes, 1974, 1979). The dominant local force acting on a subchain is the elastic force arising from the action of the linked subchains, whereas the local hydrodynamic forces, whose accumulation along the network gives rise to global elastic stretching, are negligible. Theoretically, since a vertical sequence of subchains in a network is analogous to a long chain, a network stretch transition is possible if the jet strain rate is low; however, under such conditions the flow will be dominated by viscosity and network relaxation rather than elasticity. The strong increase in the longitudinal mesh size $\xi_{\parallel}$ results in a decrease in the radial mesh size $\xi_{\perp}$ due to redistribution of the random walk stepping probabilities (Fig. 31). This results in a lateral contraction of the network toward the jet center, which is proportional to the decrease in the subchains radial mesh size. An approximation for the decrease of the polymer network radius with respect to the jet radius is given by

$$r_P(z) \cong \frac{\xi_{\perp}(z)}{\xi_0} r(z). \qquad (38)$$

As depicted in Fig. 33, this shows the dominant effect of axial stretching on the radial contraction. This result allows a significant increase of the polymer concentration at the jet center to be predicted. The concentration (in terms of the polymer volume fraction) can be calculated using $\phi_P = b^3 N_s/\xi_{\parallel}\xi_{\perp}^2$ or by using Eqs. (36) and (38) and the relationship $\phi \approx b/\xi_0$, where ϕ is the solution initial concentration:

$$\phi_P = \phi\left(\frac{r}{r_P}\right)^2 = \phi\left(\frac{\xi_0}{\xi_{\perp}}\right)^2 \cong \frac{\phi}{9}\left[\cosh\left(3\phi\frac{v}{v_0}\right) + 2\right]^2. \qquad (39)$$

Here the right term assumes affine stretching by means of the vertical force $f_z \cong 3\phi v/v_0$. When full stretching occurs, the polymer at the jet core is fully compacted ($\phi_P \cong 1$) and the corresponding jet radius can be approximated by $r_j/r_0 \approx \phi^{1/2}$,
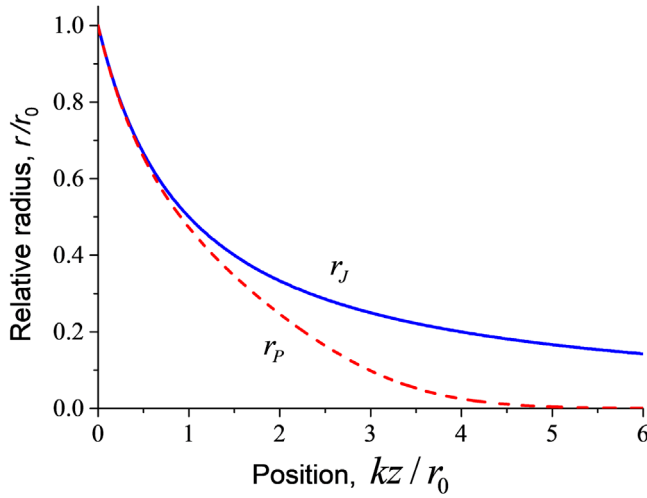
FIG. 33. Universal plot of the simulated polymer network radius r_P/r_0 vs the normalized axial position kz/r_0 compared to the jet radius r_J/r_0. Adapted from Greenfeld *et al.*, 2011.

the same result as in Eq. (37). These predictions were validated by x-ray absorption measurements on electrospun jets (Greenfeld *et al.*, 2011, 2012), as better explained later. The validity of the network modeling is restricted to the initial stage of the jet (the first few millimeters), where elastic elongation is still possible, and therefore the model does not describe the final state of the polymer matrix in electrospun nanofibers. In fact, additional processes, such as rapid solvent evaporation and polymer entanglement loss (Greenfeld and Zussman, 2013), which can result in chain relaxation, are not accounted for in this model. Nevertheless, the results strongly indicate nonequilibrium, ordered nanostructures that could remain in the nanofibers after solidification, set a new internal scale, and affect the nanofiber elasticity through confinement (Arinstein *et al.*, 2007).

2. Experiments: X-ray imaging of electrospun jets

The theoretically predicted longitudinal stretching and lateral contraction of the polymer network, as well as the additional effects of rapid evaporation, were investigated experimentally by fast x-ray, phase-contrast, high-resolution imaging of the first 10 mm of electrospun jets (Greenfeld *et al.*, 2011, 2012), using solutions of PEO (Fig. 34). The power law assumed in Eq. (30) is validated by detailed measurements of the jet profile under a wide range of electrospinning conditions, demonstrating that the jet diameter narrows faster under higher electric fields, lower flow rates, and lower polymer concentrations (Fig. 35).

The polymer concentration mapping along and across the jet makes use of the different x-ray mass absorption coefficients of the polymer and solvent ς_p and ς_s, respectively. The absorption coefficient of the polymer solution is given by $\text{Abs}(r, z) = \varsigma_p m_p(r, z) + \varsigma_s m_s(r, z)$ (Roe, 2000), where m_p and m_s denote the mass concentrations of the polymer and solvent, respectively, the (r, z) coordinates are the radial and axial positions in the jet, respectively, and $m_s/\rho_s + m_p/\rho_p = 1$, where ρ_s and ρ_p indicate the densities of the solvent and the polymer. Thus, the change in the local
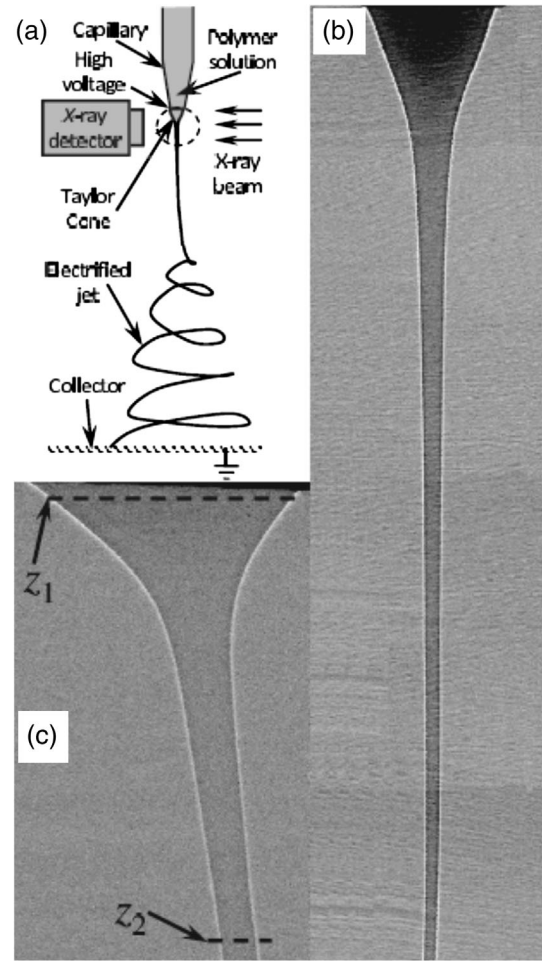

FIG. 34. (a) Schematics of electrospinning with *in situ* x-ray imaging. The imaged region is circled. Electric field gap, 6.5 cm. (b) Straight jet region (5 mm length) consisting of a sequence of ten images. Solution, 5 wt % PEO (600 kDa) in water; electric field, 0.6 kV/cm; flow rate, 3.2 ml/hr. (c) Solution, 3 wt % PEO in water; electric field, 1.6 kV/cm; flow rate, 2 ml/hr. The lines at z_1 and z_2 (0.02 and 0.5 mm, respectively) highlight the cross sections of regions used for absorption measurements across the electrospun jet. From Greenfeld *et al.*, 2011.

polymer concentration $\Delta\phi_p(r, z)$ with respect to the initial concentration ϕ is linearly dependent on the change in the local absorption coefficient ΔAbs:

$$\Delta\phi_p(r, z) = \phi_p(r, z) - \phi_p = \Delta\text{Abs}(r, z)\rho_p/(\varsigma_p\rho_p - \varsigma_s\rho_s). \tag{40}$$

$\Delta\text{Abs}(r, z)$ is calculated by comparing the measured x-ray transmission Tr_{exp} to a simulated transmission for a "still" jet (Tr_{sim}), at a given beam travel distance $d(r, z)$, through the jet:

$$\Delta\text{Abs}(r, z) \cong -\frac{1}{d(r, z)} \ln\left[\frac{\text{Tr}_{\text{exp}}(r, z)}{\text{Tr}_{\text{sim}}(r, z)}\right]\left[\frac{\text{Abs}_0}{\text{Abs}_{\text{sim}}(r, z)}\right], \tag{41}$$

where the correction factor $\text{Abs}_0/\text{Abs}_{\text{sim}}$ filters out the effects of scattering in a homogeneous jet and is used as an approximation for the heterogeneous electrified polymer
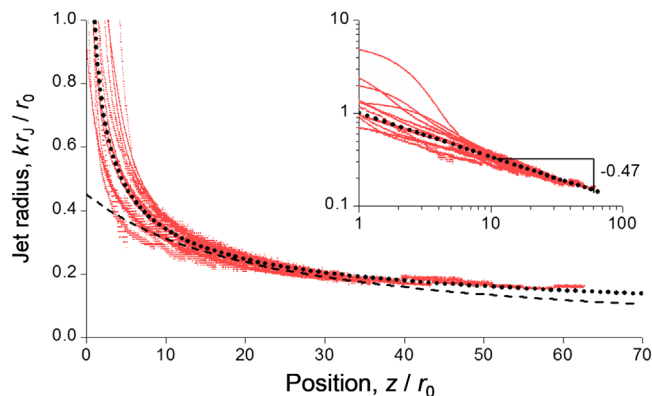
FIG. 35. Normalized jet radius kr_J/r_0 at position z/r_0 along a jet, for combined data from various electrospinning tests, where each experimental set is multiplied by the constant k pertaining to that test. (Dotted line) Power fit with the expression $r_J/r_0 = (z/r_0)^{-0.47}$, where the exponent is that measured in the inset. (Dashed line) Hyperbolic fit with the expression $r_J/r_0 = (z/r_0 + p)^{-1}$, with $p = 23.1$. (Inset) Data shown in bilog scale, highlighting the power fit exponent. The measured dimensionless parameter k compares well with the theoretical prediction. Adapted from Greenfeld *et al.*, 2012.

solution jet. Concentrations are found to rapidly increase below a critical jet radius of $\sim$25 μm (equivalent to a radius reduction ratio of 0.2; Fig. 36), possible evidence for a full network extension and for rapid evaporation that occurs much earlier than theoretical predictions found in the literature. When depicted versus the jet radius, the concentration curves collapse into groups of common initial solution concentration. The concentration crossover occurs at a lower radius for the lower solution concentration, as predicted in Eq. (37).
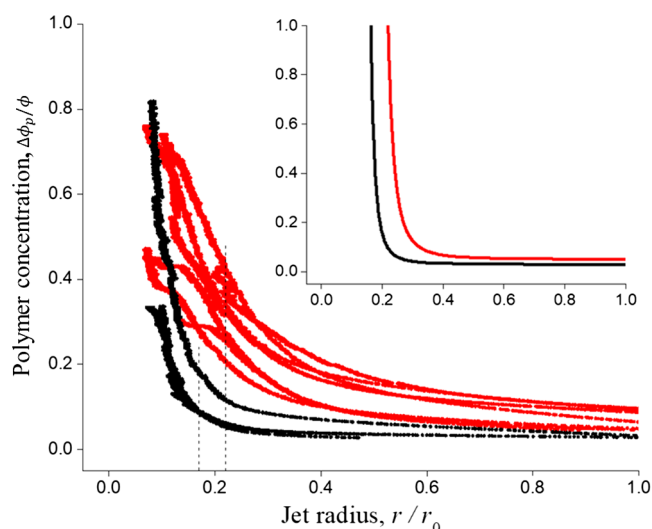

FIG. 36. Polymer concentration vs relative jet radius r_J/r_0, derived from x-ray absorption measurements at the jet center, for experiments with solution jets of PEO 3 wt % (black lines) and PEO 5 wt % (red lines). The predicted crossover radius from Eq. (37) is highlighted for both solution concentrations. (Inset) Corresponding theoretical prediction. Adapted from Greenfeld *et al.*, 2012.
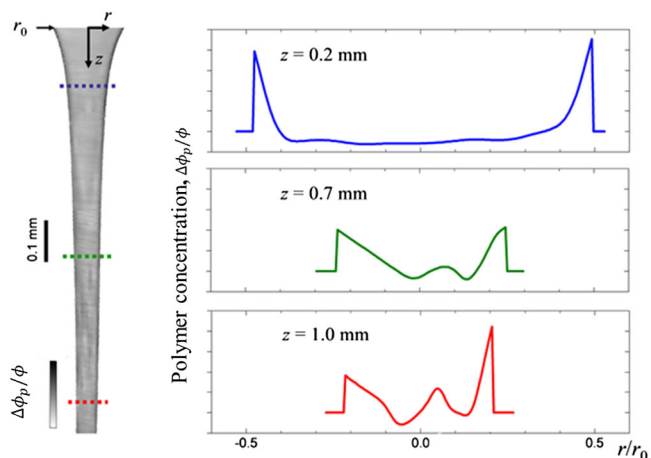

FIG. 37. Relative polymer concentration change across the jet vs relative radial distance from the jet center r/r_0 for several axial positions z along the jet. Data are from x-ray absorption measurements of PEO 5 wt %, electric field, 2.8 kV/cm; flow rate, 1.9 ml/h. Adapted from Greenfeld *et al.*, 2012.

The theoretical prediction [Eq. (39)], depicted in the inset of Fig. 36, is found to conform well to the experimental results, hence favoring the stretching premise over evaporation. These results confirm that the stretching crossover position depends predominantly on the solution initial concentration. Note that in Fig. 36 the concentration increase is slightly slower in the experiment than with the theoretical curve, possibly accounting for the stretching and stress relaxation.

The variation of concentrations across the jet also reveals high concentrations at the jet boundary due to evaporation, as well as a concentration rise at the jet center within $\sim$1 mm from the jet origin (Fig. 37), in agreement with the model and simulation. Evaporation becomes dominant when stretching is weaker, e.g., at lower electric field and/or higher flow rate, inhibiting the concentration peaks measured at the jet center. Such a tuning of parameters evidences the balance between the effects of evaporation and stretching, which determines the nonequilibrium conformation of the polymer network during electrospinning and explains the diversity of macrostructures and properties found in solid nanofibers.

VI. MODELING OF POLYMER SOLUTION BLOWING

This section reviews the works dealing with detailed modeling of solution blowing, which allows one to predict the evolution of polymer jets toward nanofibers, as well as such laydown properties as thickness, porosity, and permeability, i.e., the 3D microstructure, fiber-size distribution, and polymer mass distribution resulting from the process. Two monographs (Yarin, 1993; Yarin, Pourdeyhimi, and Ramakrishna, 2014) triggered a group of interrelated works devoted to modeling of meltblowing (Sinha-Ray, Yarin, and Pourdeyhimi, 2010a, 2011, 2013; Yarin, Sinha-Ray, and Pourdeyhimi, 2010; Ghosal, Sinha-Ray, Yarin, and Pourdeyhimi, 2016) and solution blowing (Sinha-Ray *et al.*, 2015; Ghosal, Sinha-Ray, Sinha-Ray *et al.*, 2016). The effects of the governing process parameters on variation of laydown properties were predicted, primarily the influence of the

velocity of moving collectors. For instance, it was shown and explained how an increase in the velocity of the collector screen leads to an increase in the porosity and permeability of the nonwoven laydown. The modeling was based on the system of quasi-1D equations of the dynamics of polymer solution jets moving, evaporating, and solidifying when driven by a surrounding air jet, as discussed later. The governing equations were solved numerically.

Multiple polymer jets are considered simultaneously when they are deposited on a moving screen and forming a non-woven laydown of nanofibers. A scheme that visualizes the process in the context of the model reported in this section is shown in Fig. 38(a), where two nozzles at which the polymer solution and compressed air are delivered are supported by a nosepiece. The polymer jet–air-jet interaction and the various forces acting on the jet, together with the solvent evaporation, are illustrated in Fig. 38(b). Similarly to electrified jets, the initial part (∼1 mm long) of the solution-blown jets is too thick to bend since its bending stiffness is high. Here the straight parts of polymer jets are stretched by the surrounding high-speed air jets, leading to a strong elongational flow and corresponding cross-sectional reduction. Similarly to electro-spinning, when the jet becomes thin its bending stiffness $\sim r^4$ is strongly reduced and a vigorous bending, which in the case of solution blowing is driven by aerodynamic forces, begins. Both the straight and the bending regimes are described in the framework of quasi-1D equations with the following continuity and momentum balance equations (Yarin, 1993; Yarin, Pourdeyhimi, and Ramakrishna, 2014; Sinha-Ray *et al.*, 2015; Ghosal, Sinha-Ray, Sinha-Ray *et al.*, 2016):

$$\frac{\partial \lambda f}{\partial t} + \frac{\partial f W}{\partial s} = -D_a b \pi \lambda, \qquad (42a)$$

$$\frac{\partial \lambda f \boldsymbol{v}}{\partial t} + \frac{\partial f W \boldsymbol{v}}{\partial s} = \frac{1}{\rho}\frac{\partial P\boldsymbol{\tau}}{\partial s} + \lambda f \mathbf{g} + \frac{\lambda}{\rho}\mathbf{q}_{\text{TOT}}. \qquad (42b)$$

In Eq. (42), most of the symbols have the same meaning as in Eq. (11). In particular, λ is the stretching factor, $f = \pi r^2$ is the cross-sectional area of the jet, s is an arbitrary coordinate reckoned along the jet axis that might be understood, as usual, as a Lagrangian coordinate marking material elements along the jet axis, D_a is the vapor diffusion coefficient in air, $\boldsymbol{v}$ is the absolute velocity of the polymer solution in the jet, W is the liquid velocity along the jet relative to a cross section with a certain value of s. P denotes the magnitude of the longitudinal internal viscoelastic force in the jet cross section, $\boldsymbol{\tau}$ denotes the unit tangent vector of the jet axis, $\mathbf{g}$ is the gravity acceleration, and $\mathbf{q}_{\text{TOT}}$ is the overall force acting on a jet element. In this case, the force is the aerodynamic force applied by the surrounding gas on a unit jet length rather than the electric force (Sinha-Ray, Yarin, and Pourdeyhimi, 2010a, 2011, 2013; Yarin, Sinha-Ray, and Pourdeyhimi, 2010; Sinha-Ray *et al.*, 2015; Ghosal, Sinha-Ray, Sinha-Ray *et al.*, 2016; Ghosal, Sinha-Ray, Yarin, and Pourdeyhimi, 2016). The term on the right-hand side in the continuity equation (42a) describes the solvent evaporation. The factor b in this term reads (Yarin, Pourdeyhimi, and Ramakrishna, 2014)

$$b = 0.495 \, \text{Re}_a^{1/3} \, \text{Sc}^{1/2} [C_{s,\text{eq}}(T) - C_{s,\infty}], \qquad (43)$$

where Re_a is the local Reynolds number of a jet element based on its velocity relative to the surrounding air, Sc is the Schmidt number ($\text{Sc} = \nu_{\text{air}}/D_a$, where ν_{air} is the kinematic viscosity of air), and C_s is the solvent concentration. The subscript "eq" corresponds to the equilibrium vapor pressure over the polymer solution surface determined by temperature T, whereas the subscript ∞ corresponds to the vapor content far from the jet surface in the surrounding air. Therefore, the solvent evaporation rate is dependent on T through the equilibrium solvent concentration $C_{s,\text{eq}}(T)$. This dependence can be derived from the Antoine equation (Reid, Prausnitz, and Poling, 1987) or similar equations (Seaver, Galloway, and Manuccia, 1989; Alduchov and Eskridge, 1996).

The projections of the momentum balance equation onto the accompanying trihedron of the jet axis, namely, the unit tangent vector $\boldsymbol{\tau}$, the unit principal normal vector $\mathbf{n}$, and the unit binormal vector $\mathbf{b}$, are akin to a hyperbolic wave equation. Accordingly, they can be solved numerically using the implicit numerical scheme of the generalized Crank-Nicolson type, with the central difference spatial discretization at three time levels (Sinha-Ray, Yarin, and Pourdeyhimi, 2010a, 2011, 2013; Yarin, Sinha-Ray, and Pourdeyhimi, 2010; Sinha-Ray *et al.*, 2015; Ghosal, Sinha-Ray, Sinha-Ray *et al.*, 2016; Ghosal, Sinha-Ray, Yarin, and Pourdeyhimi, 2016). The implementation of the initial and boundary conditions and the postprocessing procedure that allows one to reconstruct the 3D architecture of the laydown of nanofibers have been discussed in detail (Sinha-Ray *et al.*, 2015; Ghosal, Sinha-Ray, Sinha-Ray *et al.*, 2016) using the touchdown times of the individual jet elements, their locations on the collecting screen, and the cross-sectional radii of as-deposited filaments (Ghosal, Sinha-Ray, Sinha-Ray *et al.*, 2016; Ghosal, Sinha-Ray, Yarin, and Pourdeyhimi, 2016).

Solution blowing is an isothermal process, with the temperature T in Eq. (43) being room temperature. This temperature is typically above the θ temperature at which solvent-polymer and polymer-polymer interactions equal each other, and thus the solvents are initially good, which means that polymer molecules preferentially possess extended, elongated configurations. However, during solution blowing the solvent concentration in the polymer jet decreases due to evaporation and, accordingly, the polymer concentration C_p increases. In addition, the local polymer concentration varies due to stretching as $C_p = C_{p,0}\lambda_0 f_0/\lambda f$, where as usual the subscript 0 denotes the values at the initial cross section of the jet bending part. The rheological parameters of the viscoelastic polymer solution, namely, its viscosity and relaxation time, also vary along the jet as (Yarin, Pourdeyhimi, and Ramakrishna, 2014)

$$\mu = \mu_0 \times 10^{J(C_p^m - C_{p,0}^m)}, \qquad (44a)$$

$$\theta = \theta_0 C_{p,0}/C_p, \qquad (44b)$$

where μ_0 and θ_0 are the initial values of the viscosity and the elastic relaxation time (namely, again, those at the initial cross section of the jet bending part) and J and m are
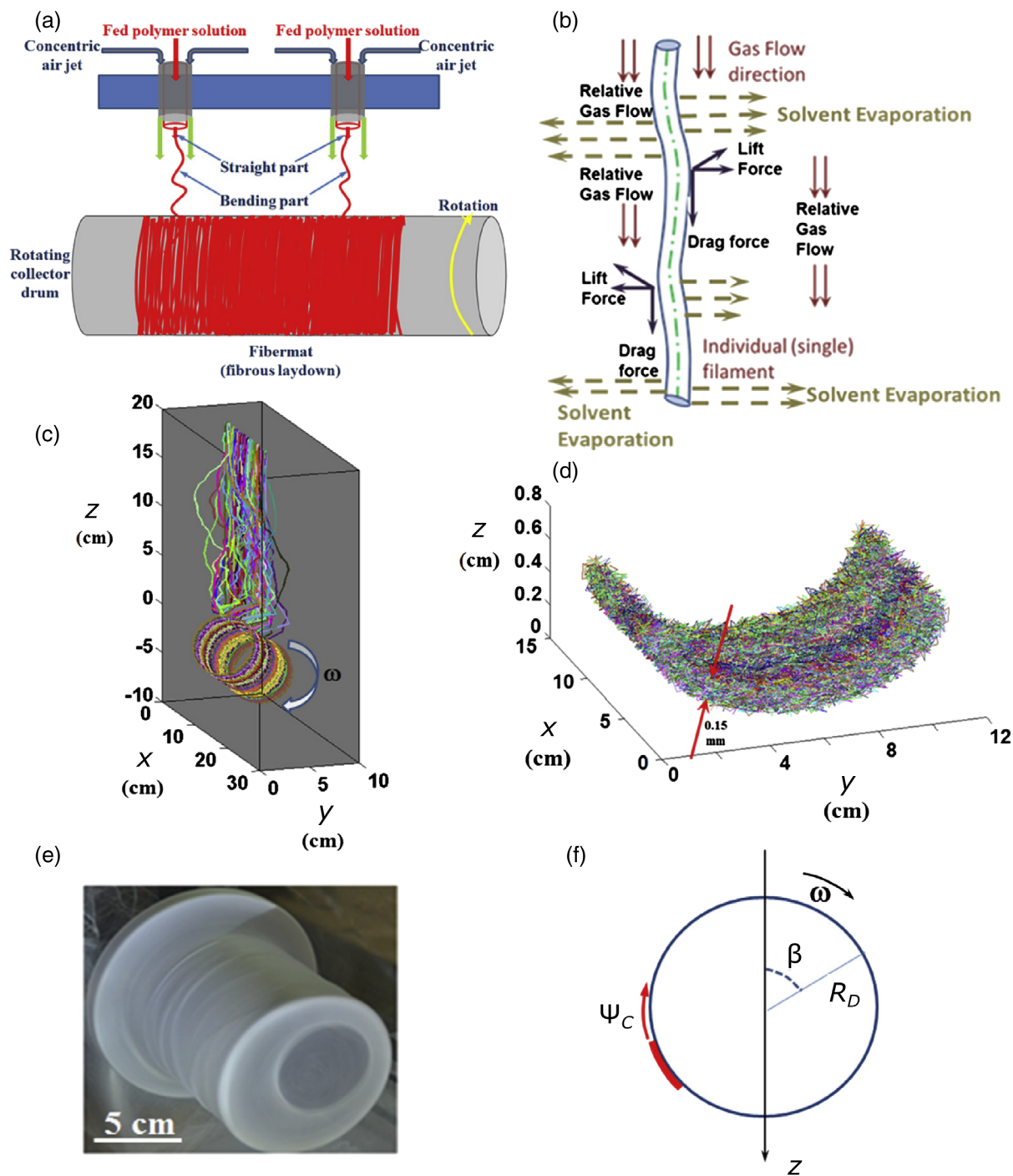
FIG. 38. (a) Scheme of polymer solution blowing, with multiple jets located along a nosepiece and a rotating collector. (b) Different forces acting on polymer solution jet. (c) Snapshot of 60 numerically simulated polymer solution jets. (d) Section of a deposited solution-blown laydown. (e) A drum used in the experiments. (f) Schematics of the drum cross section with the corresponding coordinate system. Adapted from Ghosal, Sinha-Ray, Sinha-Ray *et al.*, 2016.

material-dependent constants. This strongly nonlinear dependence of the zero-shear viscosity and of the relaxation time C_p practically arrests the deformation of the polymer solution at some moment, which corresponds to polymer precipitation at a high enough concentration where polymer-polymer self-interactions prevail. The longitudinal force P [Eq. (42b)] is a function of $\tau_{\tau\tau} - \tau_{nn}$, where $\tau_{\tau\tau}$ and τ_{nn} are the longitudinal and normal deviatoric stresses in the jet cross

section, respectively. Since $\tau_{\tau\tau} \gg \tau_{nn}$, P is practically a function of $\tau_{\tau\tau}$ only. The deviatoric stresses could be calculated using an appropriate rheological constitutive equation, for example, the UCM model (Yarin, 1993; Yarin, Pourdeyhimi, and Ramakrishna, 2014). Hence, the rheological behavior of polymer solutions can be described using phenomenological constitutive equations that do not directly utilize any physical information related to macromolecular

chains and their conformations. However, a link between UCM and micromechanical models of polymer solutions and jets was established (Yarin, 1993), showing that in strongly stretched polymer jets the higher values of the longitudinal deviatoric stress $\tau_{\tau\tau}$ correspond to the macromolecular chain stretching and orientation in the axial stretching direction. Jet stretching in flight has also been studied in detail in the framework of meltblowing (Yarin, Pourdeyhimi, and Ramakrishna, 2014).

In both experiments and numerical simulations of solution blowing (Ghosal, Sinha-Ray, Sinha-Ray *et al.*, 2016), solidified polymer jets (i.e., nanofibers) have been collected on a rotating drum [Figs. 38(a) and 38(c)–38(f)]. Here the direction of the blowing is defined as z. In particular, Fig. 38(c) shows this geometry along with a snapshot of 60 numerically simulated polymer solution jets in flight, which are wound on the collecting drum. Figure 38(d) shows a cut portion of the numerically simulated laydown on the drum. To model the process, the drum is assumed to rotate with the angular velocity $\omega = d\beta/dt$, where β is the angular coordinate around the drum axis, which is parallel to the nosepiece [Fig. 38(f)]. The drum has a cross-sectional radius R_D. The angular coordinate of a material element after its touchdown at the drum (or at the preceding fiber laydown on the drum) is found to be $\beta = \beta_{\text{touch}} + \omega(t - t_{\text{touch}})$, where the touchdown happens at the angle β_{touch} and at time $t_{\text{touch}} < t$. We emphasize that this expression allows the angle β to grow beyond $\beta_{\text{touch}} + 2\pi$, which means that the deposited fibers have made a full rotation with the drum and are being covered by a newly deposited fiber layer. The corresponding circumferential coordinate of a material element of a polymer filament on the drum is denoted as ψ_C and is found to be

$$\psi_C = \psi_{C,\text{touch}} + \omega(t - t_{\text{touch}})R_D, \qquad (45)$$

where $\psi_{C,\text{touch}} = \beta_{\text{touch}}R_D$. Therefore, the coordinate of a material element of a polymer filament on the drum along a direction normal to z and aligned parallel with the nosepiece [Fig. 38(a)] does not change after the touchdown. On the other hand, its z coordinate varies as [Fig. 38(f)] $z = z_{\text{touch}} + R_D \cos(\pi - \beta) = z_{\text{touch}} - R_D \cos\beta$, where z_{touch} corresponds to the touchdown position. This leads to

$$z = z_{\text{touch}} - R_D \cos[\beta_{\text{touch}} + \omega(t - t_{\text{touch}})]. \qquad (46)$$

The previously deposited and new layer of fibers (generated after a full rotation of the drum) could have the same value of the coordinate z as per Eq. (46), albeit they are distinguished by their coordinates ψ_C as per Eq. (45). In other words, ψ_C corresponds to a longitudinal coordinate along an unrolled laydown. These equations allow one to pose the boundary conditions at the end of a free polymer jet already deposited on the rotating cylindrical collector (the drum), similar to the boundary conditions used on planar collector screens (Sinha-Ray, Yarin, and Pourdeyhimi, 2010a, 2011, 2013; Yarin, Sinha-Ray, and Pourdeyhimi, 2010; Sinha-Ray *et al.*, 2015; Ghosal, Sinha-Ray, Sinha-Ray *et al.*, 2016; Ghosal, Sinha-Ray, Yarin, and Pourdeyhimi, 2016). These boundary conditions affect backwardly the oncoming part of the polymer jet
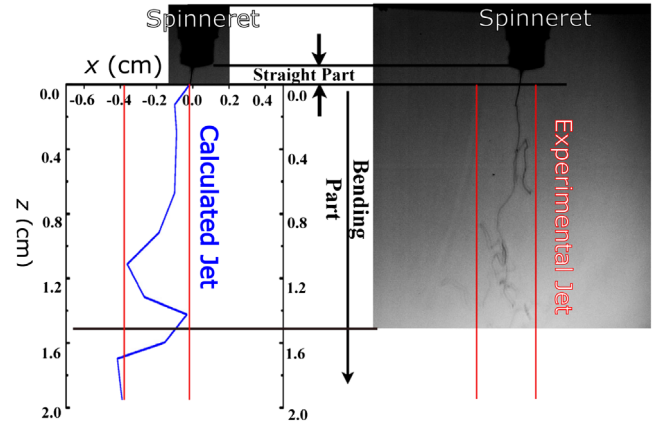

FIG. 39. Snapshot of jet configuration at the beginning of the bending part for blown polymer solutions. The bending jet domain that is found experimentally is highlighted by two vertical straight lines. The predicted snapshot of the jet axis at the beginning of the bending part wiggles between these lines, showing good agreement between model and experiment. The experimental data were acquired with a Phantom V210 fast camera. Adapted from Sinha-Ray *et al.*, 2015.

or filament through the corresponding viscoelastic force acting along the jet or filament, as predicted by the model (Ghosal, Sinha-Ray, Sinha-Ray *et al.*, 2016).

Results from simulations compare favorably with the experimental data. For instance, the predicted mean turbulent velocity field in the axisymmetric air jet surrounding polymer solution jets has been calculated (Sinha-Ray *et al.*, 2015). The simulated bending jet domain for a single solution-blown jet was found to occupy a cylinder of about 0.38 cm in diameter, whereas the experimentally observed jet was located inside a cylinder of 0.33 cm in diameter, as highlighted by the vertical lines in Fig. 39 (Sinha-Ray *et al.*, 2015). The predicted cross-sectional fiber diameter distribution is shown in Fig. 40.

Two additional properties of solution-blown nonwovens are the volumetric porosity and permeability. In modeling works, the volumetric porosity p_{vol} was defined following its basic definition, namely, based on the predicted volume V_E of the laydown envelope and the volume V_F of the polymer fibers encompassed by this envelope. Accordingly, $p_{\text{vol}} = (1 - V_F/V_E) \times 100\%$. Volumetric porosity values under different conditions were found by postprocessing the simulated nonwoven laydowns formed by 60 polymer solution jets for 1 min, and the calculated volumetric porosity was found to grow upon increasing the angular speed of the rotating drum collector (Ghosal, Sinha-Ray, Sinha-Ray *et al.*, 2016), which is reminiscent of the case of meltblowing onto a moving surface. A similar behavior was found for permeability (Ghosal, Sinha-Ray, Sinha-Ray *et al.*, 2016). Finally, the comparison of experimentally measured and numerically simulated laydown landscapes was also favorable, with similar morphological profiles and height variations (Fig. 41).

VII. PERSPECTIVE AND CONCLUSIONS

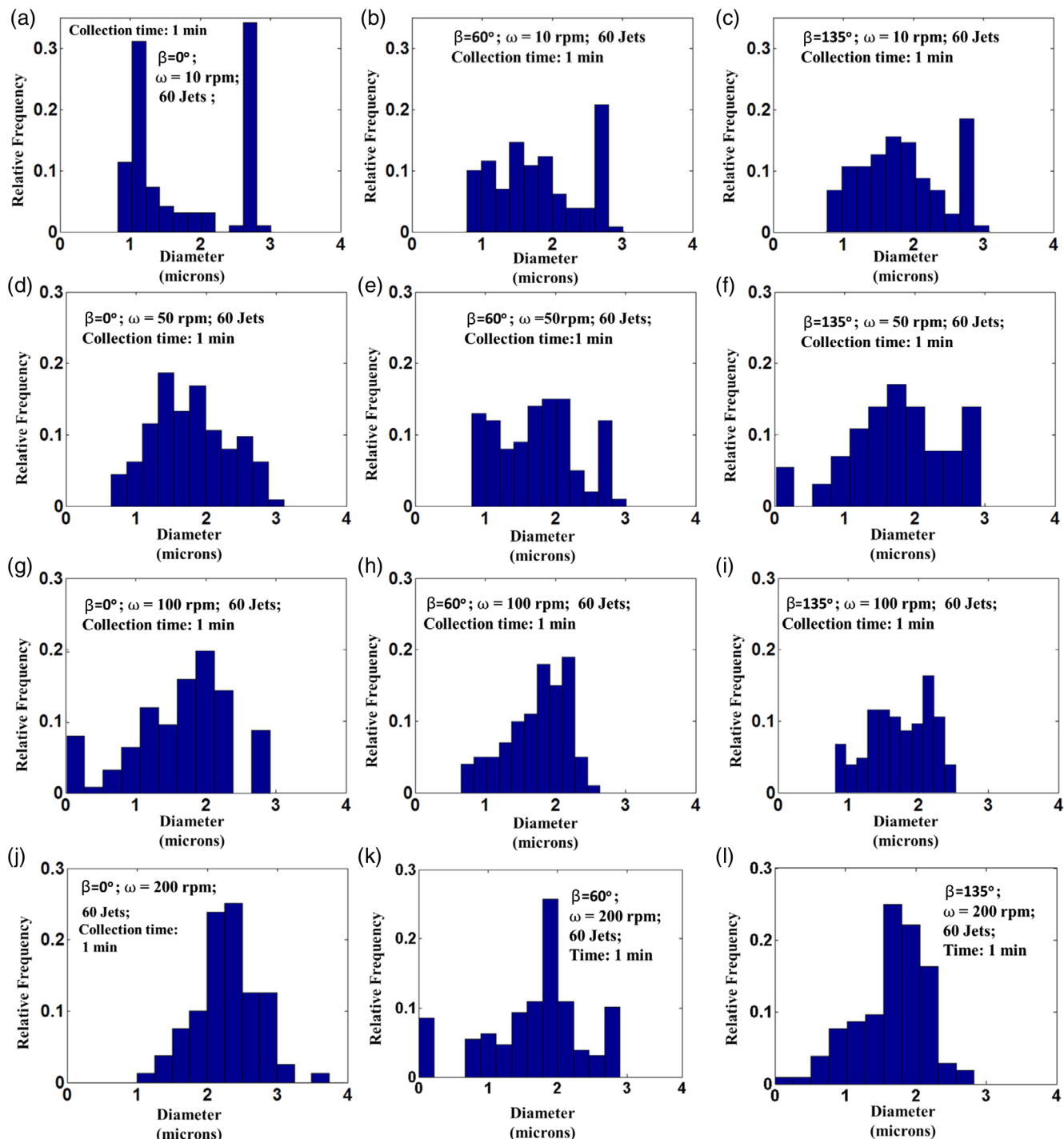Here we provide a summary of currently open challenges, as well as of possible future developments in the field of

FIG. 40. Predicted diameter distributions of solution-blown laydowns from 60 jets [parameters shown in Fig. 38(f)] for various angular velocities ω of the rotating drum. (a)–(c) Diameter distributions for $\beta = 0°$, 60°, and 135°, respectively, for $\omega = 10$ rpm. (d)–(f) Same angles, with $\omega = 50$ rpm. (g)–(i) Same angles, with $\omega = 100$ rpm. (j)–(l) Same angles, with $\omega = 200$ rpm. Adapted from Ghosal, Sinha-Ray, Sinha-Ray *et al.*, 2016.

modeling of electrified polymer jets and solution blowing, and of materials obtained by these processes.

From fluid dynamics to material properties.—Modeling of electrospinning and solution blowing is still to be generalized, for instance, to be able to predict the degree of crystallinity in the as-spun nanofibers. This would be a step toward the solution of a formidable problem, namely, the prediction of the ultimate mechanical properties of both individual

nanofibers and materials assembled with them. In fact, fiber-forming methods and laydown postprocessing encompass such processes as spunbonding and hydroentanglement, respectively. Modeling of these processes has already begun to develop along the same lines as those of electrospinning and solution blowing, i.e., based on the quasi-1D equation (11) (Li *et al.*, 2019a, 2019b). Only the first steps in this direction have been made, however, and significant efforts would be required
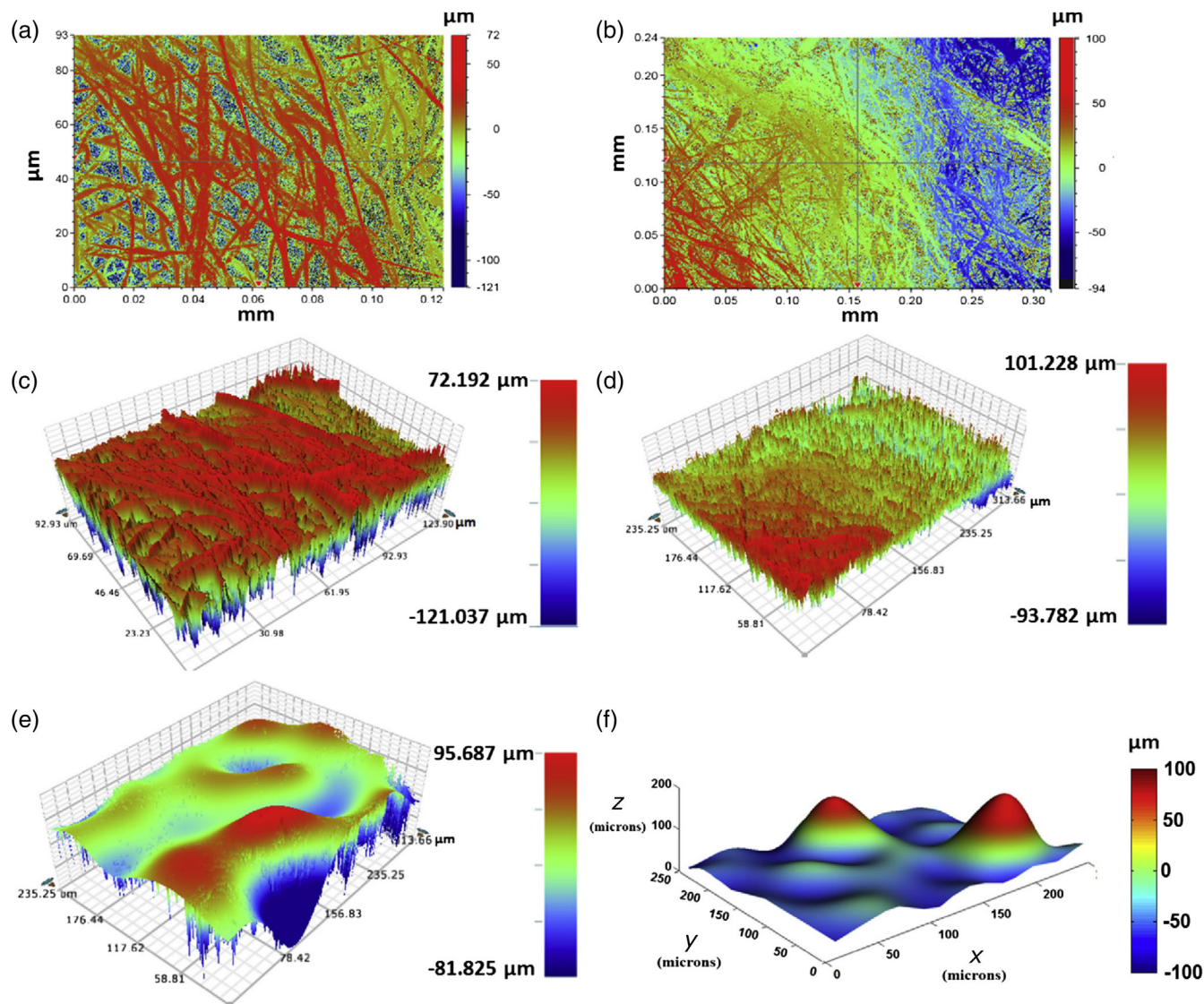
FIG. 41. Laydown produced by solution blowing of polymer nanofibers. (a)–(e) Height profiles of the laydown measured by optical profilometry at different sample points and (f) simulated average profile for a deposition region *x,y* of comparable size (of the order of 10^4 μm^2). Polymer solution concentration, 15 wt %; angular drum speed, 240 rpm. (f) *z*-numerical data are obtained starting from a large simulated laydown area (20×10 cm^2), which is then subdivided into several smaller areas of 250×250 μm^2, and the simulated mean elevation is averaged over those smaller areas. Adapted from Ghosal, Sinha-Ray, Sinha-Ray *et al.*, 2016.

in the future to predict the mechanical properties of the obtained materials. Electrospinning and solution blowing of core-shell nanofibers, such as those used in self-healing vascular, nanotextured composite materials (Yarin *et al.*, 2019), also pose multiple modeling questions. Novel electromechanical devices based on electrospun and solution-blown nanofibers (An, Kang, and Yarin, 2018; An, Sankaran, and Yarin, 2018; Kang *et al.*, 2019) involved multiple issues that require detailed modeling of material properties, and of how they descend from the jet properties and dynamics. That would enable development of software capable of controlling such nanotextured devices.

Other challenges are given by our capability to understand the internal structure of obtained nanofibers, which is also strictly related to the jet behavior. The variation of polymer concentration across the jet was found to go through high concentrations at the jet boundary due to evaporation as well as a concentration rise at the jet center (Greenfeld *et al.*, 2011, 2012). The last phenomenon is attributed to polymer stretching that causes lateral contraction of the polymer network toward the jet center, and it is in good agreement with theoretical models. Moreover, it was shown that evaporation is dominant when stretching is weaker (e.g., at lower electric field and/or higher flow rate), canceling the concentration peaks measured at the jet center. The balance between the effects of evaporation and stretching determines the polymer network nonequilibrium conformation during electrospinning, and it can help clarify the reasons for the diverse structures and properties found in solid nanofibers. In particular, the size-dependent mechanical, thermomechanical, and thermodynamic properties of as-spun nanofibers, such as the rise of the elastic modulus at small diameters and the shift of the glass

transition temperature, are attributed to the internal molecular and supramolecular structure of the polymer matrix in nanofibers. The current implementation of the method is, however, limited to the initial section of the jet. Further investigation could provide evidence for disentanglement of the polymer chains and reveal a nonuniform flow regime due to rapid evaporation, possibly with streamlines toward the jet boundary. Such studies may be important for several applications of electrospinning, such as drug delivery, nanocomposites, and aerogels based on short fibers.

Beyond Lagrangian models for a multiscale description.— The last advances in both mesoscopic and atomistic simulations led to a new multiscale paradigm. New high-tech experimental setups of electrospinning processes prompt a quantitative understanding of different complex phenomena that span a broad range of scales in both space and time. Several physical quantities may be described using different representations that are already at the same length scale. For instance, as pointed out in Sec. V.C.3, the simulation of electrospinning in the presence of a space-distributed electric field $\mathbf{E}(x, y, z)$ can be performed by coupling the Eulerian representation of the vector field to the Lagrangian jet beads. Moreover, the electrospinning process is a nonequilibrium transport problem, driven by strong force terms that span many length scales and timescales. A typical example is the repulsive Coulomb force. For each ith bead, the Coulomb term $\mathbf{f}_{c,i}$ is assessed as the summation of bead pairs (i, j) as the inverse of the distance $|\mathbf{R}_j - \mathbf{R}_i|$ [see the Coulomb term in Eq. (17)], distributed over several orders of magnitude in length ($|\mathbf{R}_j - \mathbf{R}_i|$ in the range 0.01–10 cm). With r_{pcut} denoting a primary cutoff for the Coulomb pair interactions, the Coulomb force can be split into two terms of different timescales: a contribution from all neighboring beads with $|\mathbf{R}_j - \mathbf{R}_i| \le r_{\mathrm{pcut}}$, which changes quickly in time, and a second, slower contribution due to the remaining far-field beads. Hence, it is possible to assess the force $\mathbf{f}_{c,i}$ using the so-called multistep method (Allen and Tildesley, 2017), where the contribution of the neighbor beads is computed at every time step (usually $\Delta t \sim 10^{-8}$ s), while that from the remaining beads is updated at a larger timescale (typically every $100\Delta t$).

On the other hand, other force terms cannot be easily described using a multiscale approach. For instance, the tensile stress force is related to the behavior of the polymeric matrix evolving toward nonequilibrium states when subject to the external, intense electric field. Hence, the mechanical response and fracture phenomena would require an atomistic description to be fully resolved (without using a rheological constitutive law). In the past decade, several works have investigated the mechanical response of stretched polymeric matrices at the atomistic level by Lagrangian methods (usually by molecular dynamics simulations), where particlelike points represent the atomic positions (Buell, Van Vliet, and Rutledge, 2009; Park and Joo, 2014; Miao *et al.*, 2015, 2017; Lolla *et al.*, 2016). However, the largest available system size in molecular dynamics simulations is about 10^{-6} cm, while the typical time step for the integration of the EOM is $\Delta t \sim 10^{-15}$ s. On the other hand, the typical length scales and timescales in the Lagrangian models (Sec. V.B) are about 10 cm and $\Delta t \sim 10^{-8}$ s, respectively. This range of several orders of

magnitude in both space and time is challenging to cover with a multiscale approach, which is, therefore, not a viable route in this context. Nonetheless, it is possible to exploit alternative strategies based on mesoscale physics to represent other phenomena that are not described in the Lagrangian models. As an example, in the bead models the fluid is assumed to be spinnable (ec. V.B.2), and the capillary breakup phenomena close to the nozzle are entirely missed in the description. Nonetheless, it is possible to bridge the gap using a mesoscale solver of the Navier-Stokes equation of the fluid close to the nozzle. Then, for instance, the information could be transferred to the Lagrangian bead representation within a multiscale scheme.

The mesoscale approaches are grounded in the intermediate level of the description of matter, namely, kinetic theory: the main versions are Boltzmann's kinetic theory and Langevin stochastic particle dynamics. A versatile simulation technique for solving Navier-Stokes equation is the lattice Boltzmann method (LBM), which exploits the Boltzmann kinetic theory (Benzi, Succi, and Vergassola, 1992; Krüger *et al.*, 2016; Succi, 2018). Here the fluid is represented as pseudoparticles propagating and colliding over a discrete lattice domain in space. Each pseudoparticle represents a statistical probability $f(x, y)$ of observing a fluid parcel in a lattice point moving over a discrete set of allowed directions so that the degrees of freedom of the system decrease enormously if compared to the corresponding atomistic representation. Although the LBM suffers the typical problems of grid-based methods (Secs. IV
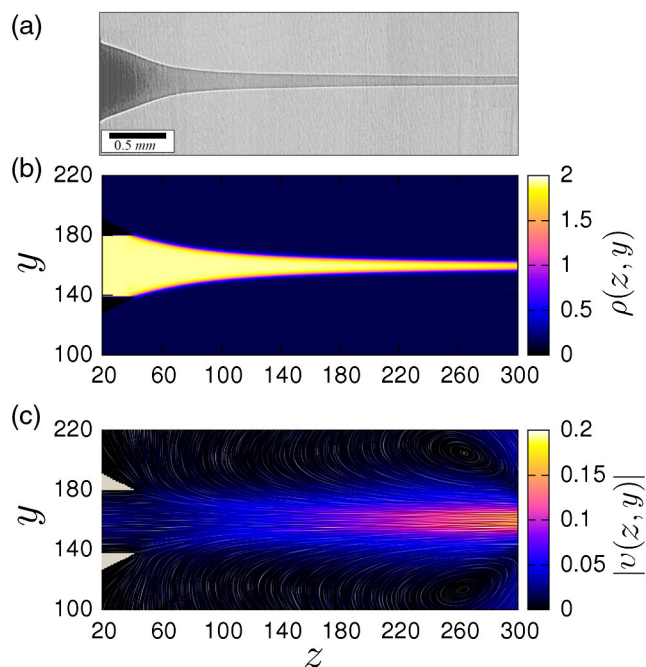

FIG. 42. (a) The quasistraight section of a jet in an electrospinning experiment with a solution of 5 wt % PEO in water. Adapted from Greenfeld *et al.*, 2011). (b) A snapshot of the fluid density $\rho(z, y)$ in the stationary regime after the jet has touched the right side of the simulation box. (c) The corresponding velocity field magnitude $|v(z, y)|$, and the line integral convolution representation (Forssell and Cohen, 1995) of the velocity field. From Lauricella *et al.*, 2018.

and V.B.1), it can be implemented with high computational efficiency, especially on parallel computers (Feichtinger *et al.*, 2015; Succi *et al.*, 2019). In the context of electrospinning modeling, the quasistraight jet path (Sec. V.B.2) can be effectively described by the LBM (Lauricella *et al.*, 2018). Figure 42 displays a comparison between hyperbolic profiles of a stretched jet observed in simulation and experiment. In particular, the profile in the simulation appears to be in qualitative agreement with the characteristic shape of the jet experimentally observed close to the injecting nozzle by the Rafailovich and Zussman groups (Greenfeld *et al.*, 2011) and is consistent with previous theoretical results on the jet conical shape (Feng, 2002, 2003). By its highly mesoscopic nature, the LBM is conceptually at a vantage point for multiscale or multilevel coupling, both upward, toward Lagrangian bead representations and downward, toward atomistic models. In perspective, a possible route is to devise new algorithms that allow for reproducing electrospinning setups of increasing complexity by coupling different descriptions from the bottom-up or, conversely, top-down overview.

LIST OF SYMBOLS AND ABBREVIATIONS

A	surface area	cm^2
Abs	linear attenuation coefficient	cm^{-1}
b	unit binormal vector of jet axis	1
Bo	Bond number	1
c	unit vector pointing to the jet curvature center	1
Ca	capillary number	1
C_s	solvent concentration	$mol\,cm^{-3}$
C_p	polymer concentration	$mol\,cm^{-3}$
D	diffusion coefficient	$cm^2\,s^{-1}$
De	Deborah number	1
e_0	electric charge per unit jet length (unperturbed)	$statC\,cm^{-1}$
E	electric field strength	$statV\,cm^{-1}$
e_L	electric charge per unit jet length	$statC\,cm^{-1}$
g	gravitational acceleration	cm/s^2
G	elastic modulus	$g\,cm^{-1}\,s^{-2}$
h	nozzle-collector distance	cm
I	current	$statC\,s^{-1}$
k	jet curvature	cm^{-1}
ℓ_{jet}	jet arc length	cm
m	mass	g
n	principal unit normal vector of jet axis	1
N_s	number of monomers	
p	pressure	$g\,cm^{-1}\,s^{-2}$
q	charge	$statC$
Q	flow rate	cm^3/s
r	cross-sectional radius	cm
r_0	cross-sectional radius (initial)	cm
r_T	droplet radius	cm

R	position vector	cm
t	time	s
T	temperature	K
Tr	radiation transmission	1
α	surface tension	g/s^2
ε	dielectric constant	1
$\dot{\varepsilon}$	strain rate	s^{-1}
Φ, φ, φ_0	electric potential	$statV$
ϕ	volume fraction	1
$\dot{\gamma}$	shear rate	s^{-1}
λ	stretching ratio	1
θ	relaxation time (viscoelastic)	s
θ_C	relaxation time (charge)	s
θ_H	relaxation time (hydrodynamic)	s
σ	stress	$g\,cm^{-1}\,s^{-2}$
σ_e	electrical conductivity	s^{-1}
σ_q	surface charge density	$statC\,cm^{-2}$
ρ	mass density	$g\,cm^{-3}$
ρ_q	volumetric charge density	$statC\,cm^{-3}$
μ	dynamic viscosity	$g\,cm^{-1}\,s^{-1}$
μ_e	elongational viscosity	$g\,cm^{-1}\,s^{-1}$
ν	kinematic viscosity	$cm^2\,s^{-1}$
τ	unit tangent vector of jet axis	1
υ	velocity	cm/s
W_G	Gibbs free energy	$g\,cm^2\,s^{-2}$
ω	angular velocity	rad/s
ξ	mesh size of polymer network	cm
Σ	mass attenuation coefficient	$cm^2\,g^{-1}$

REFERENCES

Alduchov, O. A., and R. E. Eskridge, 1996, J. Appl. Meteorol. **35**, 601.

Allen, M. P., and D. J. Tildesley, 2017, *Computer Simulation of Liquids* (Oxford University Press, Oxford).

An, S., D. J. Kang, and A. L. Yarin, 2018, Nanoscale **10**, 16591.

An, S., A. Sankaran, and A. L. Yarin, 2018, ACS Appl. Mater. Interfaces **10**, 37749.

Angammana, C. J., and S. H. Jayaram, 2011a, *Proceedings of the ESA Annual Meeting on Electrostatics*, Minneapolis (Electrostatic Society of America, Rochester, NY).

Angammana, C. J., and S. H. Jayaram, 2011b, IEEE Trans. Ind. Appl. **47**, 1028.

Angammana, C. J., and S. H. Jayaram, 2011c, IEEE Trans. Ind. Appl. **47**, 1109.

Anna, S. L., and G. H. McKinley, 2001, J. Rheol. **45**, 115.

Arinstein, A., R. Avrahami, and E. Zussman, 2009, J. Phys. D **42**, 015507.

Arinstein, A., M. Burman, O. Gendelman, and E. Zussman, 2007, Nat. Nanotechnol. **2**, 59.

Arinstein, A., Y. Liu, M. Rafailovich, and E. Zussman, 2011, Europhys. Lett. **93**, 46001.

Arinstein, A., and E. Zussman, 2011, J. Polym. Sci., Part B: Polym. Phys. **49**, 691.

Badieyan, S. S., and M. Janmaleki, 2015, J. Polym. Eng. **35**, 587.

Barenblatt, G. I., 1994, *Scaling Phenomena in Fluid Mechanics* (Cambridge University Press, Cambridge, England).

Barenblatt, G. I., 1996, *Scaling, Self-Similarity, and Intermediate Asymptotics: Dimensional Analysis and Intermediate Asymptotics* (Cambridge University Press, Cambridge, England).

Barrero, A., and I. G. Loscertales, 2007, Annu. Rev. Fluid Mech. **39**, 89.

Bassett, E. B., 1894, Am. J. Math. **16**, 93.

Batchelor, G. K., 2002, *An Introduction to Fluid Dynamics* (Cambridge University Press, Cambridge, England).

Battocchio, F., M. P. F. Sutcliffe, and F. Teschner, 2017, Proc. Inst. Mech. Eng., Part C **231**, 407.

Baumgarten, P. K., 1971, J. Colloid Interface Sci. **36**, 71.

Bazilevsky, A. V., A. L. Yarin, and C. M. Megaridis, 2008, Lab Chip **8**, 152.

Behrens, A. M., B. J. Casey, M. J. Sikorski, K. L. Wu, W. Tutak, A. D. Sandler, and P. Kofinas, 2014, ACS Macro Lett. **3**, 249.

Behrens, A. M., N. G. Lee, B. J. Casey, P. Srinivasan, M. J. Sikorski, J. L. Daristotle, A. D. Sandler, and P. Kofinas, 2015, Adv. Mater. **27**, 8056.

Bellan, L. M., and H. G. Craighead, 2006, J. Vac. Sci. Technol. B **24**, 3179.

Bellan, L. M., H. G. Craighead, and J. P. Hinestroza, 2007, J. Appl. Phys. **102**, 094308.

Belyaev, M. A., N. M. Zubarev, and O. V. Zubareva, 2019, Tech. Phys. Lett. **45**, 395.

Bennett, A., 2006, *Lagrangian Fluid Dynamics* (Cambridge University Press, Cambridge, England).

Benzi, R., R. Succi, and M. Vergassola, 1992, Phys. Rep. **222**, 145.

Bhattacharjee, P. K., T. M. Schneider, M. P. Brenner, G. H. McKinley, and G. C. Rutledge, 2010, J. Appl. Phys. **107**, 044306.

Bird, R. B., R. C. Armstrong, and O. Hassager, 1987, *Dynamics of Polymeric Liquids. Vol. 1: Fluid Mechanics* (John Wiley & Sons, New York).

Bognitzki, M., W. Czado, T. Frese, A. Schaper, M. Hellwig, M. Steinhart, A. Greiner, and J. H. Wendorff, 2001, Adv. Mater. 2001, **13**, 70.

Boltachev, G. Sh., N. M. Zubarev, and O. V. Zubareva, 2008, Phys. Rev. E **77**, 056607.

Buell, S., K. J. Van Vliet, and G. C. Rutledge, 2009, Macromolecules **42**, 4887.

Bühler, V., 2005, *Polyvinylpyrrolidone Excipients for Pharmaceuticals: Povidone, Crospovidone and Copovidone* (Springer Science+Business Media, New York).

Burman, M., A. Arinstein, and E. Zussman, 2008, Appl. Phys. Lett. **93**, 193118.

Burman, M., A. Arinstein, and E. Zussman, 2011, Europhys. Lett. **96**, 16006.

Camposeo, A., I. Greenfeld, F. Tantussi, M. Moffa, F. Fuso, M. Allegrini, E. Zussman, and Pisignano. D., 2014, Macromolecules **47**, 4704.

Camposeo, A., I. Greenfeld, F. Tantussi, S. Pagliara, M. Moffa, F. Fuso, M. Allegrini, E. Zussman, and D. Pisignano, 2013, Nano Lett. **13**, 5056.

Carroll, C. P., and Y. L. Joo, 2006, Phys. Fluids **18**, 053102.

Carroll, C. P., and Y. L. Joo, 2008, J. Non-Newtonian Fluid Mech. **153**, 130.

Carroll, C. P., and Y. L. Joo, 2009, Phys. Fluids **21**, 103101.

Carroll, C. P., and Y. L. Joo, 2011, J. Appl. Phys. **109**, 094315.

Casper, C. L., J. S. Stephens, N. G. Tassi, D. B. Chase, and J. F. Rabolt, 2004, Macromolecules **37**, 573.

Chang, C., K. Limkrailassiri, and L. Lin, 2008, Appl. Phys. Lett. **93**, 123111.

Chang, H., and A. S. Lodge, 1972, Rheol. Acta **11**, 127.

Chang, H. C., E. A. Demekhin, and E. Kalaidin, 1999, Phys. Fluids **11**, 1717.

Chen, H., N. Wang, J. Di, Y. Zhao, Y. Song, and L. Jiang, 2010, Langmuir **26**, 11291.

Cherney, L. T., 1999a, J. Fluid Mech. **378**, 167.

Cherney, L. T., 1999b, J. Aerosol Sci. **30**, 851.

Chiu-Webster, S., and J. R. Lister, 2006, J. Fluid Mech. **569**, 89.

Choi, S.-J., L. Persano, A. Camposeo, Jang J.-S., Koo W.-T., Kim S.-J., Cho H.-J., Kim I.-D., and D. Pisignano, 2017, Macromol. Mater. Eng. **302**, 1600569.

Collins, R. T., M. T. Harris, and O. A. Basaran, 2007, J. Fluid Mech. **588**, 75.

Collins, R. T., J. J. Jones, M. T. Harris, and O. A. Basaran, 2008, Nat. Phys. **4**, 149.

Collins, R. T., K. Sambath, M. T. Harris, and O. A. Basaran, 2013, Proc. Natl. Acad. Sci. U.S.A. **110**, 4905.

Coluzza, I., D. Pisignano, D. Gentili, G. Pontrelli, and S. Succi, 2014, Phys. Rev. Applied **2**, 054011.

Cooley, J. F., 1902, U.S. Patent No. 692,631.

Daristotle, J. L., A. M. Behrens, A. D. Sandler, and P. Kofinas, 2016, ACS Appl. Mater. Interfaces **8**, 34951.

Dayal, P., and T. Kyu, 2007, Phys. Fluids **19**, 107106.

Dayal, P., J. Liu, S. Kumar, and T. Kyu, 2007, Macromolecules **40**, 7689.

De Boor, C., 1978, *A Practical Guide to Splines* (Springer, New York).

de Gennes, P.-G., 1974, J. Chem. Phys. **60**, 5030.

de Gennes, P.-G., 1979, *Scaling Concepts in Polymer Physics* (Cornell University Press, Ithaca).

Deitzel, J. M., J. D. Kleinmeyer, D. Harris, and N. C. Beck Tan, 2001, Polymer **42**, 261.

Deitzel, J. M., J. D. Kleinmeyer, J. K. Hirvonen, and N. C. Beck Tan, 2001, Polymer **42**, 8163.

Deng, S., A. Arinstein, and E. Zussman, 2017, J. Polym. Sci., Part B: Polym. Phys. **55**, 506.

Divvela, M. J., and Y. L. Joo, 2017, J. Appl. Phys. **121**, 134306.

Doshi, J., and D. H. Reneker, 1995, J. Electrost. **35**, 151.

Dror, Y., W. Salalha, R. L. Khalfin, Y. Cohen, A. L. Yarin, and E. Zussman, 2003, Langmuir **19**, 7012.

Durrett, R., 2019, *Probability: Theory and Examples* (Cambridge University Press, Cambridge, England).

Dzenis, Y., 2004, Science **304**, 1917.

Eggers, J., 1997, Rev. Mod. Phys. **69**, 865.

Eggers, J., and T. F. Dupont, 1994, J. Fluid Mech. **262**, 205.

Eggers, J., and E. Villermaux, 2008, Rep. Prog. Phys. **71**, 036601.

Entov, V. M., and A. L. Yarin, 1984a, Fluid Dyn. **19**, 21.

Entov, V. M., and A. L. Yarin, 1984b, J. Fluid Mech. **140**, 91.

Fang, J., H. Niu, H. Wang, X. Wang, and T. Lin, 2013, Energy Environ. Sci. **6**, 2196.

Fasano, V., M. Moffa, A. Camposeo, L. Persano, and D. Pisignano, 2015, Macromolecules **48**, 7803.

Fedorova, N., and B. Pourdeyhimi, 2007, J. Appl. Polym. Sci. **104**, 3434.

Feichtinger, C., J. Habich, Köstler H., Rüde U., and T. Aoki, 2015, Parallel Comput. **46**, 1.

Feng, J. J., 2002, Phys. Fluids **14**, 3912.

Feng, J. J., 2003, J. Non-Newtonian Fluid Mech. **116**, 55.

Fernandez de la Mora, J., 1992, J. Fluid Mech. **243**, 561.

Fernandez de la Mora, J., 2007, Annu. Rev. Fluid Mech. **39**, 217.

Ferry, J. D., 1980, *Viscoelastic Properties of Polymers*, 3rd ed. (John Wiley & Sons, New York).

Feynman, R. P., R. B. Leighton, and M. Sands, 2006, *The Feynman Lectures on Physics*, Vol. 2 (Pearson, San Francisco).

Filatov, Y., A. Budyka, and V. Kirichenko, 2007, *Electrospinning of Micro- and Nanofibers: Fundamentals in Separation and Filtration Processes* (Begell House, New York).

Fong, H., and D. H. Reneker, 1999, J. Polym. Sci., Part B: Polym. Phys. **37**, 3488.

Formhals, A., 1934, U.S. Patent No. 1,975,504.

Formhals, A., 1939, U.S. Patent No. 2,160,962.

Formhals, A., 1940, U.S. Patent No. 2,187,306.

Formhals, A., 1943, U.S. Patent No. 2,323,025.

Formhals, A., 1944, U.S. Patent No. 2,349,950.

Forssell, L. K., and S. D. Cohen, 1995, IEEE Trans. Visual. Comput. Graph. **1**, 133.

Fridrikh, S. V., J. H. Yu, M. P. Brenner, and G. C. Rutledge, 2003, Phys. Rev. Lett. **90**, 144502.

Gañán-Calvo, A. M., 1997a, J. Fluid Mech. **335**, 165.

Gañán-Calvo, A. M., 1997b, Phys. Rev. Lett. **79**, 217.

Gañán-Calvo, A. M., 1999, J. Aerosol Sci. **30**, 863.

Gañán-Calvo, A. M., 2007, Phys. Rev. Lett. **98**, 134503.

Gañán-Calvo, A. M., J. C. Lasheras, Dávila J., and A. Barrero, 1994, J. Aerosol Sci. **25**, 1121.

Gañán-Calvo, A. M., López-Herrera J. M., M. A. Herrada, A. Ramos, and J. M. Montanero, 2018, J. Aerosol Sci. **125**, 32.

Gañán-Calvo, A. M., López-Herrera J. M., Rebollo-Muńoz N., and J. M. Montanero, 2016, Sci. Rep. **6**, 32357.

Gañán-Calvo, A. M., and J. M. Montanero, 2009, Phys. Rev. E **79**, 066305.

Gañán-Calvo, A. M., Gonzáles-Prieto R., Riesco-Chueca P., M. A. Herrada, and Flores-Mosquera M., 2007, Nat. Phys. **3**, 737.

Ghosal, A., S. Sinha-Ray, S. Sinha-Ray, A. L. Yarin, and B. Pourdeyhimi, 2016, Polymer **105**, 255.

Ghosal, A., S. Sinha-Ray, A. L. Yarin, and B. Pourdeyhimi, 2016, Polymer **85**, 19.

Gilbert, W., 1600, *De Magnete* (Peter Short, London) [English translation by P. F. Mottelay (Ferris Brothers, New York, 1893), p. 89].

Grasl, C., M. M. Arras, M. Stoiber, H. Bergmeister, and H. Schima, 2013, Appl. Phys. Lett. **102**, 053111.

Gray, M. C., 1953, Q. Appl. Math. **11**, 311.

Greenfeld, I., A. Arinstein, K. Fezzaa, M. H. Rafailovich, and E. Zussman, 2011, Phys. Rev. E **84**, 041806.

Greenfeld, I., K. Fezzaa, M. H. Rafailovich, and E. Zussman, 2012, Macromolecules **45**, 3616.

Greenfeld, I., and E. Zussman, 2013, J. Polym. Sci., Part B: Polym. Phys. **51**, 1377.

Greiner, A., and J. H. Wendorff, 2007, Angew. Chem., Int. Ed. **46**, 5670.

Greiner, A., J. H. Wendorff, A. L. Yarin, and E. Zussman, 2006, Appl. Microbiol. Biotechnol. **71**, 387.

Guarino, V., V. Iannotti, G. Ausanio, L. Ambrosio, and L. Lanotte, 2019, eXPRESS Polym. Lett. **13**, 419.

Guenthner, A. J., S. Khomobhongse, W. Liu, P. Dayal, D. H. Reneker, and T. Kyu, 2006, Macromol. Theory Simul. **15**, 87.

Gui-rong, L., 2003, *Smoothed Particle Hydrodynamics: A Meshfree Particle Method* (World Scientific, Singapore).

Hamed, A., N. Shehata, and M. Elosairy, 2018, Polymers **10**, 12.

Han, T., D. H. Reneker, and A. L. Yarin, 2007, Polymer **48**, 6064.

Han, T., A. L. Yarin, and D. H. Reneker, 2008, Polymer **49**, 1651.

Hayati, I., 1992, Colloids Surf. **65**, 77.

Herrada, M. A., López-Herrera J. M., Gañán-Calvo A. M., E. J. Vega, J. M. Montanero, and S. Popinet, 2012, Phys. Rev. E **86**, 026305.

Higuera, F. J., 2003, J. Fluid Mech. **484**, 303.

Higuera, F. J., 2006, J. Fluid Mech. **558**, 143.

Hohman, M. M., M. Shin, G. Rutledge, and M. P. Brenner, 2001a, Phys. Fluids **13**, 2201.

Hohman, M. M., M. Shin, G. Rutledge, and M. P. Brenner, 2001b, Phys. Fluids **13**, 2221.

Hsiao, H.-Y., Huang C.-M., Liu Y.-Y., Kuo Y.-C., and H. Chen, 2012, J. Appl. Polym. Sci. **124**, 4904.

Huang, C., S. Chen, C. Lai, D. H. Reneker, H. Qiu, Y. Ye, and H. Hou, 2006, Nanotechnology **17**, 1558.

Huang, W., L. Jiang, J. Luo, Z. Chen, L. Ren, and C. Li, 2016, Mater. Manuf. Processes **31**, 1603.

Huebner, A. L., 1969, J. Fluid Mech. **38**, 679.

Huebner, A. L., 1970, Science **168**, 118.

Jang, J.-S., S.-J. Kim, S.-J. Choi, N.-H. Kim, M. Hakim, A. Rothschild, and I.-D. Kim, 2015, Nanoscale **7**, 16417.

Jarusuwannapoom, T., W. Hongrojjanawiwat, S. Jitjaicham, L. Wannatong, M. Nithitanakul, C. Pattamaprom, P. Koombhongse, R. Rangkupan, and P. Supaphol, 2005, Eur. Polym. J. **41**, 409.

Jeans, J., 1958, *The Mathematical Theory of Electricity and Magnetism* (Cambridge University Press, Cambridge, England).

Ji, J., K. Ghosh, B. Li, J. C. Sokolov, R. A. F. Clark, and M. H. Rafailovich, 2006, Macromol. Biosci. **6**, 811.

Ji, Y., *et al.*, 2008, Europhys. Lett. **84**, 56002.

Jian, H. Y., S. V. Fridrikh, and G. C. Rutledge, 2006, Polymer **47**, 4789.

Kakade, M. V., S. Givens, K. Gardner, K. H. Lee, D. B. Chase, and J. F. Rabolt, 2007, J. Am. Chem. Soc. **129**, 2777.

Kalayci, V. E., P. K. Patra, Y. K. Kim, S. C. Ugbolue, and S. B. Warner, 2005, Polymer **46**, 7191.

Kalra, V., J. H. Lee, J. H. Park, M. Marquez, and Y. L. Joo, 2009, Small **5**, 2323.

Kalra, V., S. Mendez, J. H. Lee, H. Nguyen, M. Marquez, and Y. L. Joo, 2006, Adv. Mater. **18**, 3299.

Kang, D. J., S. An, A. L. Yarin, and S. Anand, 2019, Nanoscale **11**, 2065.

Kase, S., and T. Matsuo, 1965, J. Polym. Sci. A **3**, 2541.

Khakhar, D. V., and J. M. Ottino, 1987, Int. J. Multiphase Flow **13**, 71.

Khalid, B., X. Bai, H. Wei, Y. Huang, H. Wu, and Y. Cui, 2017, Nano Lett. **17**, 1140.

Khansari, S., S. Duzyer, S. Sinha-Ray, A. Hockenberger, A. L. Yarin, and B. Pourdeyhimi, 2013, Mol. Pharmaceutics **10**, 4509.

Kirichenko, V. M., I. V. Petrianov-Sokolov, N. N. Suprun, and A. A. Shutov, 1986, Sov. Phys. Dokl. **31**, 611.

Kloeden, P. E, and E. Platen, 2013, *Numerical Solution of Stochastic Differential Equations* (Springer Science+Business Media, New York).

Kolbasov, A., Sinha-Ray S., A. Joijode, M. A. Hassan, D. Brown, B. Maze, B. Pourdeyhimi, and A. L. Yarin, 2016, Ind. Eng. Chem. Res. **55**, 323.

Koombhongse, S., W. X. Liu, and D. H. Reneker, 2001, J. Polym. Sci., Part B: Polym. Phys. **39**, 2598.

Kowalewski, T. A., S. Barral, and T. Kowalczyk, 2009, in *Proceedings of the IUTAM Symposium on Modelling Nanomaterials and Nanosystems*, Aalborg, Denmark, edited by R. Pyrz and C. Rauhe (Springer, Dordrecht), pp. 279–292.

Kowalewski, T. A., S. Błoński, and S. Barral, 2005, Bull. Pol. Acad. Sci. Tech. Sci. **53**, 385.

Krüger, T., H. Kusumaatmaja, A. Kuzmin, O. Shardt, G. Silva, and E. M. Viggen, 2016, *The Lattice Boltzmann Method: Principles and Practice* (Springer, New York).

Kyselica, R., and E. T. Enikov, 2016, in *Proceedings of the International Mechanical Engineering Congress and Exposition*, p. V04AT05A025, https://doi.org/10.1115/IMECE2016-65405.

Kyselica, R., E. T. Enikov, and R. Anton, 2019, J. Electrost. **98**, 75.

Kyselica, R., E. T. Enikov, P. Polyvas, and R. Anton, 2018, J. Electrost. **94**, 21.

Lamb, H., 1959, *Hydrodynamics* (Cambridge University Press, Cambridge, England).

Landau, L. D., and E. M. Lifshitz, 1970, *Theory of Elasticity* (Pergamon Press, Oxford).

Landau, L. D., E. M. Lifshitz, and L. P. Pitaevskii, 1984, *Electrodynamics of Continuous Media* (Butterworth-Heinemann, Oxford).

Lauricella, M., F. Cipolletta, G. Pontrelli, D. Pisignano, and S. Succi, 2017, Phys. Fluids **29**, 082003.

Lauricella, M., S. Melchionna, A. Montessori, D. Pisignano, G. Pontrelli, and S. Succi, 2018, Phys. Rev. E **97**, 033308.

Lauricella, M., D. Pisignano, and S. Succi, 2016, J. Phys. Chem. A **120**, 4884.

Lauricella, M., D. Pisignano, and S. Succi, 2017, Europhys. Lett. **119**, 44001.

Lauricella, M., G. Pontrelli, C. Coluzza, D. Pisignano, and S. Succi, 2015a, Comput. Phys. Commun. **197**, 227.

Lauricella, M., G. Pontrelli, I. Coluzza, D. Pisignano, and S. Succi, 2015b, Mech. Res. Commun. **69**, 97.

Lauricella, M., G. Pontrelli, D. Pisignano, and S. Succi, 2015, Mol. Phys. **113**, 2435.

Lauricella, M., G. Pontrelli, D. Pisignano, and S. Succi, 2016, J. Comput. Sci. **17**, 325.

Lee, H. C., 1974, IBM J. Res. Dev. **18**, 364.

Lee, S. W., H. J. Lee, J. H. Choi, W. G. Koh, J. M. Myoung, J. H. Hur, J. J. Park, J. H. Cho, and U. Jeong, 2010, Nano Lett. **10**, 347.

Li, D., Y. Wang, and Y. Xia, 2003, Nano Lett. **3**, 1167.

Li, D., Y. Wang, and Y. Xia, 2004, Adv. Mater. **16**, 361.

Li, D., and Y. Xia, 2004a, Nano Lett. **4**, 933.

Li, D., and Y. Xia, 2004b, Adv. Mater. **16**, 1151.

Li, F., A. M. Gañán-Calvo, J. M. López-Herrera, X.-Y. Yin, and X.-Z. Yin, 2013, J. Non-Newtonian Fluid Mech. **196**, 58.

Li, G., C. Staszel, A. L. Yarin, and B. Pourdeyhimi, 2019a, Polymer **164**, 191.

Li, G., C. Staszel, A. L. Yarin, and B. Pourdeyhimi, 2019b, Polymer **164**, 205.

Li, H., T. C. Halsey, and A. Lobkovsky, 1994, Europhys. Lett. **27**, 575.

Li, W. W., Z. W. Luo, X. Wang, J. Y. Zheng, G. F. Zheng, and D. H. Yousefi, 2015, Key Eng. Mater. **645-646**, 281.

Liu, H., J. B. Edel, L. M. Bellan, and H. G. Craighead, 2006, Small **2**, 495.

Liu, L., and Y. Dzenis, 2008, Nanotechnology **19**, 355307.

Liu, M. B., and G. R. Liu, 2016, *Particle Methods for Multi-scale and Multi-physics* (World Scientific, Singapore).

Liu, S., and D. H. Reneker, 2019, Polymer **168**, 155.

Liu, Y., S. Chen, E. Zussman, C. S. Korach, W. Zhao, and M. Rafailovich, 2011, Macromolecules **44**, 4439.

Liu, Y., G. Zhang, X. Zhuang, S. Li, L. Shi, W. Kang, B. Cheng, and X. Xu, 2019, Polymers **11**, 364.

Loitsyanskii, L. G., 1996, *Mechanics of Liquids and Gases* (Pergamon Press, Oxford).

Lolla, D., J. Gorse, C. Kisielowski, J. Miao, P. L. Taylor, G. G. Chase, and D. H. Reneker, 2016, Nanoscale **8**, 120.

López-Herrera, J. M., and A. M. Gañán-Calvo, 1999, J. Fluid Mech. **501**, 303.

López-Herrera, J. M., A. M. Gañán-Calvo, and M. Perez-Saborid, 1999, J. Aerosol Sci. **30**, 895.

Loscertales, I. G., A. Barrero, I. Guerrero, R. Cortijo, M. Marquez, and A. M. Gañán-Calvo, 2002, Science **295**, 1695.

Loscertales, I. G., A. Barrero, M. Marquez, R. Spretz, R. Velarde-Ortiz, and G. Larsen, 2004, J. Am. Chem. Soc. **126**, 5376.

Lu, X., C. Wang, and Y. Wei, 2009, Small **5**, 2349.

Lukas, D., A. Sarkar, and P. Pokorny, 2008, J. Appl. Phys. **103**, 084309.

Luo, C. J., S. D. Stoyanov, E. Stride, E. Pelanb, and M. Edirisinghe, 2012, Chem. Soc. Rev. **41**, 4708.

Ma, M., V. Krikorian, J. H. Yu, E. L. Thomas, and G. C. Rutledge, 2006, Nano Lett. **6**, 2969.

Mackay, M. E., and D. V. Boger, 1987, J. Non-Newtonian Fluid Mech. **22**, 235.

Magarvey, R. H., and L. E. Outhouse, 1962, J. Fluid Mech. **13**, 151.

Magaz, A., A. D. Roberts, S. Faraji, T. R. L. Nascimento, E. S. Medeiros, W. Zhang, R. D. Greenhalgh, A. Mautner, X. Li, and J. D. Blaker, 2018, Biomacromolecules **19**, 4542.

Malkawi, G., A. L. Yarin, and F. Mashayek, 2010, J. Appl. Phys. **108**, 064910.

Matovich, M. A., and J. R. A. Pearson, 1969, Ind. Eng. Chem. Fundam. **8**, 512.

Maxwell, J. C., 1867, Phil. Trans. R. Soc. A **157**, 49.

Megelski, S., J. S. Stephens, D. B. Chase, and J. F. Rabolt, 2002, Macromolecules **35**, 8456.

Mei, L. Y., P. Song, and Y. Q. Liu, 2015, J. Appl. Polym. Sci. **132**, 41995.

Melcher, J. R., and G. I. Taylor, 1969, Annu. Rev. Fluid Mech. **1**, 111.

Melcher, J. R., and E. P. Warren, 1971, J. Fluid Mech. **47**, 127.

Meneveau, C., T. S. Lund, and W. H. Cabot, 1996, J. Fluid Mech. **319**, 353–385.

Miao, J., R. S. Bhatta, D. H. Reneker, M. Tsige, and P. L. Taylor, 2015, Polymer **56**, 482.

Miao, J., D. H. Reneker, M. Tsige, and P. L. Taylor, 2017, Polymer **125**, 190.

Michelson, D., 1990, *Electrostatic Atomization.* (Adam Higler, Bristol, England).

Middleman, S., 1995, *Modeling Axisymmetric Flows: Dynamics of Films, Jets, and Drops* (Academic Press, New York).

Montessori, A., M. Lauricella, E. Stolovicki, D. A. Weitz, and S. Succi, 2019, Phys. Fluids **31**, 021703.

Montinaro, M., V. Fasano, M. Moffa, A. Camposeo, L. Persano, M. Lauricella, S. Succi, and D. Pisignano, 2015, Soft Matter **11**, 3424.

Morozov, A., 2015, in *Complex Fluids in Biological Systems*, edited by S. E. Spagnolie(Springer, New York).

Morozov, V. N., and A. Y. Mikheev, 2012, J. Membr. Sci. **403-404**, 110.

Morton, W. J., 1902, U.S. Patent No. 705,691.

Neubert, S., D. Pliszka, A. Góra, A. Jaworek, E. Wintermantel, and S. Ramakrishna, 2012, J. Appl. Polym. Sci. **125**, 820.

Ng, S. L., R. P. Mun, D. V. Boger, and D. F. James, 1996, J. Non-Newtonian Fluid Mech. **65**, 291.

Notz, P. K., and O. A. Basaran, 1999, J. Colloid Interface Sci. **213**, 218.

Pagliara, S., M. S. Vitiello, A. Camposeo, A. Polini, R. Cingolani, G. Scamarcio, and D. Pisignano, 2011, J. Phys. Chem. C **115**, 20399.

Pai, C.-L., M. C. Boyce, and G. C. Rutledge, 2009, Macromolecules **42**, 2102.

Pai, C.-L., M. C. Boyce, and G. C. Rutledge, 2011, Polymer **52**, 2295.

Park, J. H., and Y. L. Joo, 2014, Soft Matter **10**, 3494.

Pillai, R., J. D. Berry, D. J. E. Harvie, and M. R. Davidson, 2016, Soft Matter **12**, 3310.

Pimbley, W. T., 1976, IBM J. Res. Dev. **20**, 148.

Pinchuk, L. C., V. A. Goldade, A. V. Makarevich, and N. V. Kestelman, 2002, *Meltblowing Equipment Technology and Polymer Fibrous Materials* (Springer, Berlin).

Pisignano, D., 2013, *Polymer Nanofibers* (Royal Society of Chemistry, Cambridge, England).

Polat, Y., E. S. Pampal, E. Stojanovska, R. Simsek, A. Hassanin, A. Kilic, A. Demir, and S. Yilmaz, 2016, J. Appl. Polym. Sci. **133**, 43025.

Pontrelli, G., D. Gentili, I. Coluzza, D. Pisignano, and S. Succi, 2014, Mech. Res. Commun. **61**, 41.

Press, W. H., S. A. Teukolsky, W. T. Vetterling, and B. P. Flannery, 1996, *FORTRAN Numerical Recipes*, Vol. 1 (Cambridge University Press, Cambridge, England).

Prilutski, G., R. K. Gupta, T. Sridhar, and M. E. Ryan, 1983, J. Non-Newtonian Fluid Mech. **12**, 233.

Rafiei, S., S. Maghsoodloo, B. Noroozi, V. Mottaghitalab, and A. K. Haghi, 2013, Cellul. Chem. Technol. **47**, 323.

Rahmani, S., M. Rafizadeh, and F. Afshar Taromi, 2014, J. Appl. Polym. Sci. **131**, 41179.

Ramakrishna, S., K. Fujihara, W. E. Teo, T. C. Lim, and Z. Ma, 2005, *An Introduction to Electrospinning and Nanofibers* (World Scientific, Singapore).

Ramos, A., and A. Castellanos, 1994a, Phys. Lett. A **184**, 268.

Ramos, A., and A. Castellanos, 1994b, J. Electrost. **33**, 61.

Lord Rayleigh, 1878, Proc. London Math. Soc. **s1-10**, 4.

Reid, R. C., J. M. Prausnitz, and B. E. Poling, 1987, *The Properties of Gases and Liquids* (McGraw-Hill, New York).

Rein, D. M., Shavit-Hadar L., Khalfin R.L, Y. Cohen, K. Shuster, and E. Zussman, 2007, J. Polym. Sci., Part B: Polym. Phys. **45**, 766.

Reneker, D. H., and I. Chun, 1996, Nanotechnology **7**, 216.

Reneker, D. H., and H. Fong, 2006, Eds., *Polymeric Nanofibers* (American Chemical Society, Washington, DC).

Reneker, D. H., and A. L. Yarin, 2008, Polymer **49**, 2387.

Reneker, D. H., A. L. Yarin, H. Fong, and S. Koombhongse, 2000, J. Appl. Phys. **87**, 4531.

Reneker, D. H., A. L. Yarin, E. Zussman, and H. Xu, 2007, Adv. Appl. Mech. **41**, 43.

Resta, V., A. Camposeo, M. Montinaro, M. Moffa, K. Kazlauskas, S. Jursenas, A. Tomkeviciene, J. V. Grazulevicius, and D. Pisignano, 2017, Opt. Express **25**, 24604.

Reznik, S. N., A. L. Yarin, A. Theron, and E. Zussman, 2004, J. Fluid Mech. **516**, 349.

Reznik, S. N., A. L. Yarin, E. Zussman, and L. Bercovici, 2006, Phys. Fluids **18**, 062101.

Reznik, S. N., and E. Zussman, 2010, Phys. Rev. E **81**, 026313.

Richard-Lacroix, M., and C. Pellerin, 2013, Macromolecules **46**, 9473.

Richard-Lacroix, M., and C. Pellerin, 2015, Macromolecules **48**, 4511.

Roe, R.J., 2000, *Methods of X-Ray and Neutron Scattering in Polymer Science* (Oxford University Press, New York).

Salalha, W., Y. Dror, R. L. Khalfin, Y. Cohen, A. L. Yarin, and E. Zussman, 2004, Langmuir **20**, 9852.

Saville, D. A., 1970, Phys. Fluids **13**, 2987.

Saville, D. A., 1971a, J. Fluid Mech. **48**, 815.

Saville, D. A., 1971b, Phys. Fluids **14**, 1095.

Saville, D. A., 1997, Annu. Rev. Fluid Mech. **29**, 27.

Schlecht, S., S. Tan, M. Yosef, R. Dersch, J. H. Wendorff, Z. Jia, and A. Schaper, 2005, Chem. Mater. **17**, 809.

Schlichting, H., 1979, *Boundary Layer Theory* (McGraw-Hill, New York).

Seaver, M., A. Galloway, and T. J. Manuccia, 1989, Rev. Sci. Instrum. **60**, 3452.

Shenoy, S. L., W. D. Bates, H. L. Frisch, and G. E. Wnek, 2005, Polymer **46**, 3372.

Shin, M., M. M. Hohman, M. P. Brenner, and G. C. Rutledge, 2001, Appl. Phys. Lett. **78**, 1149.

Sinha-Ray, S., M. W. Lee, S. Sinha-Ray, S. An, B. Pourdeyhimi, S. S. Yoon, and A. L. Yarin, 2013, J. Mater. Chem. C **1**, 3491.

Sinha-Ray, S., Sinha-Ray S., A. L. Yarin, and B. Pourdeyhimi, 2015, Polymer **56**, 452.

Sinha-Ray, S., A. L. Yarin, and B. Pourdeyhimi, 2010a, J. Appl. Phys. **108**, 034912.

Sinha-Ray, S., A. L. Yarin, and B. Pourdeyhimi, 2010b, Carbon **48**, 3575.

Sinha-Ray, S., A. L. Yarin, and B. Pourdeyhimi, 2011, Polymer **52**, 2929.

Sinha-Ray, S., A. L. Yarin, and B. Pourdeyhimi, 2013, Polymer **54**, 860.

Smith, W., and T. R. Forester, 1996, J. Mol. Graphics **14**, 136.

Smythe, W. R., 1989, *Static and Dynamic Electricity* (McGraw-Hill, New York).

Sommerfeld, A., 1952, *Electrodynamics: Lectures on Theoretical Physics*, Vol. 3 (Academic Press, New York).

Spivak, A. F., and Y. A. Dzenis, 1998, Appl. Phys. Lett. **73**, 3067.

Spivak, A. F., Y. A. Dzenis, and D. H. Reneker, 2000, Mech. Res. Commun. **27**, 37.

Srikar, R., A. L. Yarin, C. M. Megaridis, A. V. Bazilevsky, and E. Kelley, 2008, Langmuir **24**, 965.

Stelter, M., G. Brenn, A. L. Yarin, R. P. Singh, and F. Durst, 2000, J. Rheol. **44**, 595.

Sternberg, E., and W. T. Koiter, 1958, J. Appl. Mech. **25**, 575.

Stone, H. A., J. R. Lister, and M. P. Brenner, 1999, Proc. R. Soc. A **455**, 329.

Succi, S., 2018, *The Lattice Boltzmann Equation: For Complex States of Flowing Matter* (Oxford University Press, Oxford).

Succi, S., G. Amati, M. Bernaschi, G. Falcucci, M. Lauricella, and A. Montessori, 2019, Comput. Fluids **181**, 107.

Sui, X. M., C. L. Shao, and Y. C. Liu, 2005, Appl. Phys. Lett. **87**, 113115.

Sun, D., C. Chang, S. Li, and L. Lin, 2006, Nano Lett. **6**, 839.

Sun, Y., Y. Zeng, and X. Wang, 2011, Ind. Eng. Chem. Res. **50**, 1099.

Sun, Z., E. Zussman, A. L. Yarin, J. H. Wendorff, and A. Greiner, 2003, Adv. Mater. **15**, 1929.

Sundaray, B., V. Subramanian, T. S. Natarajan, Xiang R.-Z., Chang C.-C., and Fann W.-S., 2004, Appl. Phys. Lett. **84**, 1222.

Suvorov, V. G., and N. M. Zubarev, 2004, J. Phys. D **37**, 289.

Taylor, G. I., 1964, Proc. R. Soc. A **280**, 383.

Taylor, G. I., 1966, Proc. R. Soc. A **291**, 145.

Tchavdarov, B., A. L. Yarin, and S. Radev, 1993, J. Fluid Mech. **253**, 593.

Teo, W. E., and S. Ramakrishna, 2006, Nanotechnology **17**, R89.

Theron, S. A., A. L. Yarin, E. Zussman, and E. Kroll, 2005, Polymer **46**, 2889.

Theron, S. A., E. Zussman, and A. L. Yarin, 2001, Nanotechnology **12**, 384.

Theron, S. A., E. Zussman, and A. L. Yarin, 2004, Polymer **45**, 2017.

Thompson, C. J., G. G. Chase, A. L. Yarin, and D. H. Reneker, 2007, Polymer **48**, 6913.

Tomotika, S., 1935, Proc. R. Soc. A **150**, 322.

Tomotika, S., 1936, Proc. R. Soc. A **153**, 302.

Tuckerman, M., 2010, *Statistical Mechanics: Theory and Molecular Simulation* (Oxford University Press, Oxford).

Tutak, W., S. Sarkar, S. Lin-Gibson, T. M. Farooque, G. Jyotsnendu, D. Wang, J. Kohn, D. Bolikal, and C. G. Simon, 2013, Biomaterials **34**, 2389.

Um, I. C., D. Fang, B. S. Hsiao, A. Okamoto, and B. Chu, 2004, Biomacromolecules **5**, 1428.

van Dyke, M., 1964, *Perturbation Methods in Fluid Mechanics* (Academic Press, New York).

Vasilyev, G., M. Burman, A. Arinstein, and E. Zussman, 2017, Macromol. Mater. Eng. **302**, 1600554.

Wang, C., H.-S. Chien, C.-H. Hsu, Y.-C. Wang, C.-T. Wang, and H.-A. Lu, 2007, Macromolecules **40**, 7973.

Wang, X., I. C. Um, D. Fang, A. Okamoto, B. S. Hsiao, and B. Chu, 2005, Polymer **46**, 4853.

Weber, C., 1931, Z. Angew. Math. Mech. **11**, 136.

Wendorff, J. H., S. Agarwal, and A. Greiner, 2012 *Electrospinning* (Wiley-VCH, Weinheim).

Wu, X.-F., Y. Salkovskiy, and Y. A. Dzenis, 2011, Appl. Phys. Lett. **98**, 223108.

Xia, Y., P. Yang, Y. Sun, Y. Wu, B. Mayers, B. Gates, Y. Yin, F. Kim, and H. Yan, 2003, Adv. Mater. **15**, 353.

Xie, J., M. R. MacEwan, W. Z. Ray, W. Liu, D. Y. Siewe, and Y. Xia, 2010, ACS Nano **4**, 5027.

Xu, H., A. L. Yarin, and D. H. Reneker, 2003, Polym. Prepr. **44**, 51.

Xu, L., Y. Wu, and Y. Nawaz, 2011, Comput. Math. Appl. **61**, 2116.

Yan, F., B. Farouk, and F. Ko, 2003, Aerosol Sci. Technol. **34**, 99.

Yang, D., B. Lu, Y. Zhao, and X. Jiang, 2007, Adv. Mater. **19**, 3702.

Yang, G., J. Wang, Y. Wang, L. Li, X. Guo, and S. B. Zhou, 2015, ACS Nano **9**, 1161.

Yarin, A. L., 1993, *Free Liquid Jets and Films: Hydrodynamics and Rheology* (Longman, Harlow, England).

Yarin, A. L., 2007, in *Springer Handbook of Experimental Fluid Mechanics*, edited by C. Tropea, A. L. Yarin, and J. Foss (Springer, Berlin), pp. 57–82.

Yarin, A. L., 2011, Polym. Adv. Technol. **22**, 310.

Yarin, A. L., W. Kataphinan, and D. H. Reneker, 2005, J. Appl. Phys. **98**, 064501.

Yarin, A. L., S. Koombhongse, and D. H. Reneker, 2001a, J. Appl. Phys. **89**, 3018.

Yarin, A. L., S. Koombhongse, and D. H. Reneker, 2001b, J. Appl. Phys. **90**, 4836.

Yarin, A. L., M. W. Lee, S. An, and S. S. Yoon, 2019, *Self-Healing Nanotextured Vascular Engineering Materials* (Springer Nature, Cham, Switzerland).

Yarin, A. L., B. Pourdeyhimi, and S. Ramakrishna, 2014, *Fundamentals and Applications of Micro- and Nanofibers* (Cambridge University Press, Cambridge, England).

Yarin, A. L., I. V. Roisman, and C. Tropea, 2017, *Collision Phenomena in Liquids and Solids* (Cambridge University Press, Cambridge, England).

Yarin, A. L., S. Sinha-Ray, and B. Pourdeyhimi, 2010, J. Appl. Phys. **108**, 034913.

Yarin, A. L., S. Sinha-Ray, and B. Pourdeyhimi, 2011, Polymer **52**, 2929.

Yarin, A. L., and D. A. Weiss, 1995, J. Fluid Mech. **283**, 141.

Yarin, A. L., and E. Zussman, 2004, Polymer **45**, 2977.

Yarin, A. L., E. Zussman, J. H. Wendorff, and A. Greiner, 2007, J. Mater. Chem. **17**, 2585.

Yarin, L. P, 2012, *The Pi-Theorem: Applications to Fluid Mechanics and Heat and Mass Transfer* (Springer, Berlin).

Yousefi, S. H., D. G. Venkateshan, C. Tang, H. V. Tafreshi, and B. Pourdeyhimi, 2018, J. Appl. Phys. **124**, 235307.

Yu, J. H., S. V. Fridrikh, and G. C. Rutledge, 2004, Adv. Mater. **16**, 1562.

Yu, J. H., S. V. Fridrikh, and G. C. Rutledge, 2006, Polymer **47**, 4789.

Yuya, N., W. Kai, B. S. Kim, and I. S. Kim, 2010, J. Mater. Sci. Eng. Adv. Technol. **2**, 97.

Zel'dovich, Ya. B., 1937, Zh. Eksp. Teor. Fiz. **7**, 1463.

Zel'dovich, Ya. B., 1992, *Selected Works of Ya. B. Zel'dovich*, Vol 1, Chemical Physics and Hydrodynamics (Princeton University Press, Princeton).

Zeleny, J., 1914, Phys. Rev. **3**, 69.

Zeleny, J., 1917, Phys. Rev. **10**, 1.

Zhang, R., S. Knitter, S. F. Liew, F. G. Omenetto, B. M. Reinhard, H. Cao, and L. Dal Negro, 2016, Appl. Phys. Lett. **108**, 011103.

Zhang, X., and O. A. Basaran, 1996, J. Fluid Mech. **326**, 239.

Zhang, Y., Z.-M. Huang, X. Xu, C. T. Lim, and S. Ramakrishna, 2004, Chem. Mater. **16**, 3406.

Zhao, Y., X. Cao, and L. Jiang, 2007, J. Am. Chem. Soc. **129**, 764.

Zhuang, X., L. Shi, K. Jia, B. Cheng, and W. Kang, 2013, J. Membr. Sci. **429**, 66.

Ziabicki, A., 1961, Kolloid Z. **175**, 14.

Ziabicki, A., and H. Kawai, 1991, *High-Speed Fiber Spinning: Science and Engineering Aspects* (Krieger Publishing Company, Malabar, FL).

Zubarev, N. M., 2001, JETP Lett. **73**, 544.

Zubarev, N. M., 2002, Phys. Rev. E **65**, 055301.

Zubarev, N. M., 2006, Phys. Fluids **18**, 028103.

Zubarev, N. M., and O. V. Zubareva, 2004, Tech. Phys. Lett. **30**, 23.

Zubarev, N. M., and O. V. Zubareva, 2005, Phys. Rev. E **71**, 016307.

Zussman, E., and A. Arinstein, 2011, J. Polym. Sci., Part B: Polym. Phys. **49**, 691.

Zussman, E., A. Theron, and A. L. Yarin, 2003, Appl. Phys. Lett. **82**, 973.

Zussman, E., A. L. Yarin, A. V. Bazilevsky, R. Avrahami, and M. Feldman, 2006, Adv. Mater. **18**, 348.